2009

Smart Rotating Machines for Structural Health Monitoring

Dmitry Leonidovich Storozhev
Cleveland State University

SMART ROTATING MACHINES FOR STRUCTURAL HEALTH MONITORING

DMITRY LEONIDOVICH STOROZHEV

Bachelor of Science in Mechanical Engineering

Cleveland State University

May, 2008

Submitted in partial fulfillment of requirements for the degree

MASTER OF SCIENCE IN MECHANICAL ENGINEERING

at the

CLEVELAND STATE UNIVERSITY

December, 2009

This thesis has been approved

for the Department of MECHANICAL ENGINEERING

and the College of Graduate Studies by

_____

Dr. Jerzy T. Sawicki, Thesis Committee Chairperson
Department of Mechanical Engineering, CSU

_____

Dr. John L. Frater
Department of Mechanical Engineering, CSU

_____

Dr. Ana V. Stankovic
Department of Electrical and Computer Engineering, CSU

_____

Dr. John D. Lekki
NASA Glenn Research Center

ACKNOWLEDGEMENTS

I would first like to express my gratitude to my advisor, Dr. Jerzy T. Sawicki, for his incomparable guidance and support throughout my graduate career and the entire research. Without his mentorship this work would be difficult to accomplish. People like Dr. Jerzy T. Sawicki make difference in this world.

I would also like to thank the committee members, Dr. John L. Frater, Dr. Ana V. Stankovic and Dr. John D. Lekki, for their helpful observations, suggestions and time.

I would like to thank David W. Epperly, machinist of the Fenn College of Engineering, for his outstanding help with the crack detection test rig.

My expression of appreciation goes to NASA Glenn Research Center for funding this project. Without NASA's financial help this work would not be possible.

I would like to thank my lab mate Alex Pesch for his valuable suggestions and comments.

Finally, I would like to thank my wife Veronica along with my parents, Leonid and Olga, and my in-laws, Michael and Ludmila, for their love, patience and support throughout my educational pursuits.

SMART ROTATING MACHINES FOR STRUCTURAL HEALTH MONITORING

DMITRY LEONIDOVICH STOROZHEV

ABSTRACT

The objective of this thesis is to explore an innovative approach to the on-line health monitoring of rotating machinery in the presence of structural damage using active magnetic bearings (AMBs). First, the detailed model of the rotor with the breathing transverse crack is developed using finite element method. Next, the experimental data from the rotating magnetically levitated healthy and cracked shafts, under specially designed external excitation force, was collected, analyzed and compared with the computer simulation. The obtained results demonstrate that the presented on-line health monitoring technique is very effective for detection of the structural damage in rotating machinery, and it has a potential to be effectively applied in industry.

TABLE OF CONTENTS

LIST OF TABLES

LIST OF FIGURES

NOMENCLATURE

A	Area of a pole face, m^2
A_{AMB}	Amplitude of external AMB force, N
C	Damping matrix
c	Damping coefficient, N-s/m
e	Eccentricity, m
F_{AMB}	External AMB force, N
F_{st}	Static component of the external force due to weight of the rotor, N
F_{dy}	Dynamic component of the external force due to unbalance, N
F_1	Force generated by top electromagnet, N
F_2	Force generated by bottom electromagnet, N
F_d	Disturbance force acting on rotor, N
$f(\theta)$	Crack steering function
$G(s)$	Overall transfer function of controller
$G_N(s)$	Transfer function of notch filter in Laplace domain
$G_{LP}(s)$	Transfer function of low-pass filter in Laplace domain
$G_{PID}(s)$	Transfer function of PID controller in Laplace domain
g	Gravitational constant, m/s^2
I_c	Control current, A
I_o	Total bias current, A
I_0^r	Radial bias current, A
I_0^a	Axial bias current, A

I_c^r	Radial control current, A
I_c^a	Axial control current, A
I	Coil current, A
I_t	Transverse moment of inertia, kg-m^2
I_p	Polar moment of inertia, kg-m^2
K	Stiffness matrix
k	Stiffness coefficient, N/m
K_D	Derivative gain of PID controller, A-s/μm
K_I	Integral gain of PID controller, A/μm-s
k_i	Force-current factor, N/A
K_P	Proportional gain of PID controller, A/μm
K_T	Total gain of controller
$K(t)$	Stiffness matrix as a function of time in inertial coordinate frame
k_x	Stiffness in x-direction, N/m
k_{xf}	Force-displacement factor, N/μm
k_y	Stiffness in y-direction, N/m
K_0^{rot}	Stiffness matrix of the healthy rotor in rotating coordinate system
k_ζ	Stiffness in ζ-direction, N/m
k_η	Stiffness in η-direction, N/m
l_1	Distance between the rotor mass center and the center of actuation of drive end AMB, m
l_2	Distance between the rotor mass center and the center of actuation of non-drive end AMB, m

M	Mass matrix
m	Mass of the rotor, kg
N	Number of turn per coil
n	Any integer number
O_b	Bearing centerline
O_s	Shaft center
q	Position vector, m
r_{ca}	Radius of rotor at the center of AMB actuation
s	Air gap between stator and rotor, μm
s_0	Nominal air gap, μm
T	Transformation matrix from rotating to inertial coordinates
t	Time, s
V, W, Z	Coordinate frame of magnetic bearing system
x, y, z	Inertial coordinate system
α	Angular displacement of rotor around W-axis, degrees or rad
β	Angular displacement of rotor around V-axis, degrees or rad
Δk	Stiffness reduction coefficient, N/m
Δk_x	Stiffness reduction in x-direction due to crack, N/m
Δk_y	Stiffness reduction in y-direction due to crack, N/m
Δk_ζ	Stiffness reduction in ζ-direction due to crack, N/m
Δk_η	Stiffness reduction in η-direction due to crack, N/m
ΔV	Lateral displacement of rotor along V-axis, μm
ΔW	Lateral displacement of rotor along W-axis, μm

ΔZ	Lateral displacement of rotor along Z-axis, μm
ζ_{LP}	Damping ratio of low-pass filter
ζ_N	Damping ratio of notch filter
ζ, η, z	Rotating coordinate system
θ	Rotational angle of the rotor, degree or rad
λ	Angle between rotor response vector and crack centerline, rad
μ_0	Magnetic field constant, H/m
ϕ	Pole centerline angle, degrees
ψ	Cone angle of the rotor, degrees
Ω	Combinational frequency, rad/s or Hz
Ω_{AMB}	Frequency of external AMB force, rad/s or Hz
ω	Rotational speed of the rotor, rpm or Hz
ω_{cutoff}	Cutoff frequency of low-pass filter, Hz
ω_i	i^{th} natural frequency of the system, rad/s or Hz
ω_{notch}	Notch frequency of notch filter, Hz
ω_{n1}	Natural frequency corresponding to first rigid mode, rad/s or Hz
ω_{n2}	Natural frequency corresponding to second rigid mode, rad/s or Hz
ω_{n3}	Natural frequency corresponding first bending mode, rad/s or Hz

CHAPTER I

INTRODUCTION

1.1 Background and Motivation

Rotating machinery is a very common and widely used in the modern industrial world. For example, steam turbines, compressors, pumps and jet engines are the most known and commonly used rotating machines. A breakdown of the rotating machine may result in economic losses and even worse, in the death of a human being. That is why damage diagnostics of the rotating machinery during the operation is a very important and one of the most difficult engineering tasks on which the durability and safety of machine operation depend.

There are a variety of malfunctions that can cause machine failure; one of them is a crack. A crack is unpredictable and the most dangerous fault because it is can lead to abrupt catastrophic consequences. In theory, presence of a crack in the rotating machine will change the dynamic characteristics of the machine due to asymmetric stiffness

caused by a crack, but in reality it is very hard to see the difference between dynamic characteristics of healthy and cracked rotors while they are in operation. The defect can be identified only when the crack grows to a very large and unsafe size. There is a significant quantity of researches and publications all over the world devoted to the early shaft crack identification problem; however, there are still not enough reliable techniques.

1.2 Literature Review

Detection and monitoring of fatigue cracks in the rotating machinery has been an interesting area of scientific study in the past 35 years. Particularly, the dynamic characteristics of cracked shafts and their monitoring have received the most attention in this area of research. There have been numerous papers written related to cracked shafts.

In order to conduct a study on the behavior of the rotor with a crack, a model of a cracked rotor has to be first derived. Gasch [Gasch, 1976] investigated the behavior of a simple rotor with a cross-sectional crack. He modeled a rotor with a breathing crack using the simplest "Hinge Model". In this model the crack opens and closes abruptly as the rotor spins; therefore, stiffness of the shaft remains at a maximum value (closed crack) for the first half a rotor's revolution and after that abruptly changes to a minimum value (opened crack) and remains for the second half a rotor's revolution. Numerical simulations showed subharmonic resonances at 1/3X and 2/3X, which were interpreted as characteristics of the cracked shaft.

Mayes and Davies [Mayes, 1976, Mayes, 1980] presented the vibration behavior of a rotating shaft containing a transverse crack. They used a cosine function to describe an opening and closing or "breathing" behavior of a cracked shaft. Moreover, they

demonstrated that when the angle between the crack and the unbalance lies within the range of -45º to 135º, the crack possesses major effects. When the unbalance is outside of this range, rotor demonstrates an uncracked behavior.

Jun et al. [Jun, 1992] derived the direct and cross-coupled stiffnesses of a rotor with a breathing crack using principles of fracture mechanics. It was concluded that the second horizontal harmonic components measured near the 2X resonant speed are the best characteristics of the cracked rotor.

Papadopoulus and Dimarogonas [Papadopoulos, 1987] demonstrated the coupling of bending and longitudinal vibrations of a rotating shaft due to a transverse crack. Also, they showed that an instability region exists for shafts with different moments of inertia experiencing natural vibrations.

Sawicki et al. [Sawicki, 2003] presented the cracked rotating shaft passing through the resonance with the constant acceleration and the constant driving torque. In order to determine the breathing of the crack, they used the angle between the vibration vector and the crack that allowed them to ignore the weight dominance assumption. They observed the presence of 1/3X and 1/2X subharmonic resonance peaks and amplification of 1X resonance peak when the crack exists in the shaft. Furthermore, they showed that the stalling effect is very sensitive to the crack; rotor can stall even with a small increase of a crack depth.

Lee and Chung [Lee, 2000] offered a nondestructive method for detecting a crack in a shaft using eigenfrequency test data. Sinou [Sinou, 2008] proposed the use of 2X and 3X super-harmonic frequency components for identifying the breathing transverse crack in a rotor. Xiang et al. [Xiang, 2008] developed a method of detection of a crack in a shaft

based on the combination of wavelet-based elements and generic algorithm. Excellent literature reviews on a dynamic behavior of cracked rotors and damage detection in shafts are done by Wauer [Wauer, 1990], Gasch [Gasch, 1993] and Dimarogonas [Dimarogonas, 1996]. All of these works, which address detection of transverse crack in rotors, do not involve external excitation technique i.e. applying an additional force on the spinning rotor not found during normal operation.

Of the works that explore active diagnostics of cracks in rotating shafts, active magnetic bearings (AMBs) are commonly used as force actuators because of their non-contact nature of rotor support and inherent position sensors.

Aenis et al. [Aenis, 2002] introduced the model-based fault identification techniques using AMBs. They investigated different techniques of force measurement and possible accuracy of a radial AMB such as a reluctance network method, the *i-s*-method, and flux based method using Hall sensors. It was found that the Hall sensor method is the most accurate.

Zhu et al. [Zhu, 2002] theoretically analyzed the dynamic characteristics of the cracked rotor using AMB. They showed that the dynamic characteristics of the rotor system containing a transverse crack with AMBs are more complicated than the system with no AMBs. Also, it was concluded that the 2X and 3X super-harmonic components in the subcritical speed region can help to identify a crack in the rotor system with AMBs.

Nordmann and Aenis [Nordmann, 2004] used a built-in software for fault identification together with AMBs to measure force and frequency response of the centrifugal pump and to diagnose faults.

Mani et al. [Mani, 2005, Mani, 2006] and Quinn et al. [Quinn, 2005] analytically and experimentally demonstrated a technique of health monitoring of rotor systems with the breathing crack using AMB as a force actuator. In their work, the rotor was supported on conventional ball bearings with AMB situated near the midspan of the rotor. AMB was used to inject a special sinusoidal excitation force. They used a multiple scale analysis in order to identify combinational resonances which occur due to crack. Also, it was shown that the cracked rotor under an excitation force at the combinational frequency experiences an increase in the response amplitude at the fundamental frequency as the depth of the crack increases.

Sawicki et al. [Sawicki, 2008] presented modeling, simulations, and experimental results obtained using the cracked rotor supported on ball bearings under external excitation force which was generated with additional AMB positioned near the midspan of the spinning rotor. It was shown that when a cracked rotor undergoes a specially designed harmonic excitation force, the combinational frequencies are induced, which can be used as indicator of presence of the crack.

There are many techniques for on-line detection of faults in rotating machinery. Most techniques use measured vibration signals and analyze orbits or Fourier spectra for a unique fault signature. However, recently there is a trend toward smart rotating machinery, where the machine can have a self-diagnostic features and full active control. Figure 1.1 shows the principle block diagram of the smart machine. The diagram was developed by R. Nordmann [Nordmann, 2001].

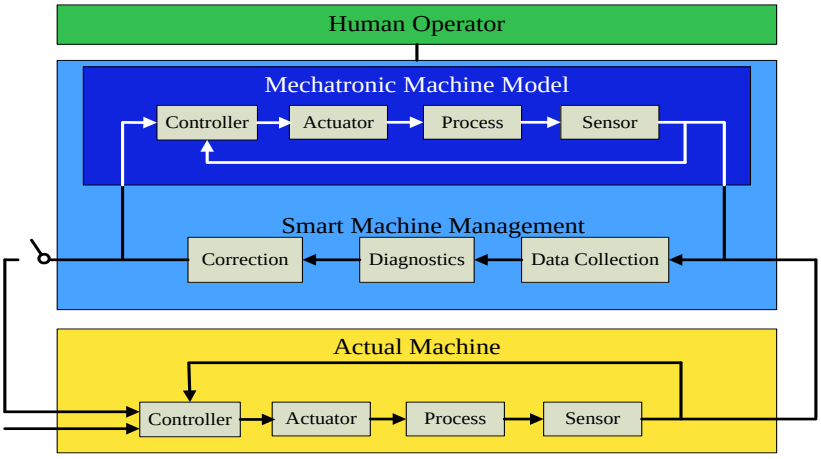

Figure 1.1 Principal block diagram of a smart machine

The block diagram shows that the smart machine consists of three parts. The first part consists of the actual machine during the work process, the controller, the actuator and sensors. The second part of the block diagram is a computer based mechatronic model of the actual machine which runs simultaneously with the actual machine. The third part is the management of the smart machine, which makes the machine "smart". It gathers the information from the actual machine and from the model and identifies the present condition of the machine. Moreover, as a result of a closed-loop control, the machine can have self-diagnostic features, i.e. create specially designed experimental signals to check the parameters of the system. Based on the obtained results, prediction, detection and correction of faults can be possible [Schweitzer, 2005]. Excellent review on smart machines and their applications and capabilities was done by Maslen [Maslen, 2008].

The approach presented in this thesis uses specially designed excitation force applied at one of the rotor supporting active magnetic bearings in order to detect a crack. In contrast with other published works done by Quinn et al. [Quinn, 2005], Mani et al. [Mani, 2006], Sawicki et al. [Sawicki, 2008], and Wroblewski [Wroblewski, 2008] the

undertaken approach does not require additional force actuator to generate the force excitation. This technology enables rotating machinery to become smart or have self-diagnosing features.

1.3 Objective and Scope of Thesis

The main objective of the present thesis is to validate a new approach for on-line detection of the transverse crack in AMB-supported shafts during operation. In addition to pure levitation, the rotor supporting bearing also serves as a force actuator that transforms current signals additionally injected inside the control loop into the superimposed specially selected forces which perturb suspended spinning rotor. These additional excitations induce combinational frequencies in the spectrum of the rotor response, providing a unique signature of the presence of a crack. This would be the step toward smart rotating machinery where no additional hardware is required for diagnostic purposes. The existing bearing and its sensors can be utilized for on-line structural damage detection. The inherent ability for sensing, information processing and actuation give the magnetic bearing the potential to become a key element in smart machines.

Chapter II describes the basics of a theoretical modeling of the Jeffcott rotor with a breathing transverse surface crack. The breathing behavior of a transverse crack is modeled based on a weight dominance assumption. Also, this Chapter presents the required conditions for combinational resonances that occur due to the presence of a crack.

Chapter III presents the modeling of the experimental rotor-bearing system and its rotordynamic analysis. The results of the computer simulation are provided for the system with the healthy, 25% cracked and 40% cracked rotors.

Chapter IV presents a complete description of the experimental crack detection test rig as well as a configuration of the external signal injection and data acquisition systems. Experimental data is plotted for the healthy, 25% cracked and 40% cracked shafts with various AMB force injections. In addition, there is a section on a detailed modeling and control of a system with conical AMBs.

Chapter V presents the conclusions of the present research work.

CHAPTER II

MODELING OF A CRACKED ROTOR

2.1 Introduction

Fracture mechanics defines a crack as an infinitesimal defect which exists on the surface or within the material. A crack is unpredictable and the most dangerous fault in rotating machinery for the reason that it is can lead to abrupt catastrophic consequences. Damage of the machine can be prevented by identifying a crack on early stages of its propagation. There are three modes of crack deformation:

1) Opening mode – crack deforms due to distribution of tensile stresses;
2) Sliding mode – crack deforms due to distribution of shear stresses;
3) Tearing mode – crack deforms due to distribution of out-of-plane shear stresses.

Figure 2.1 shows these three modes of crack deformation.

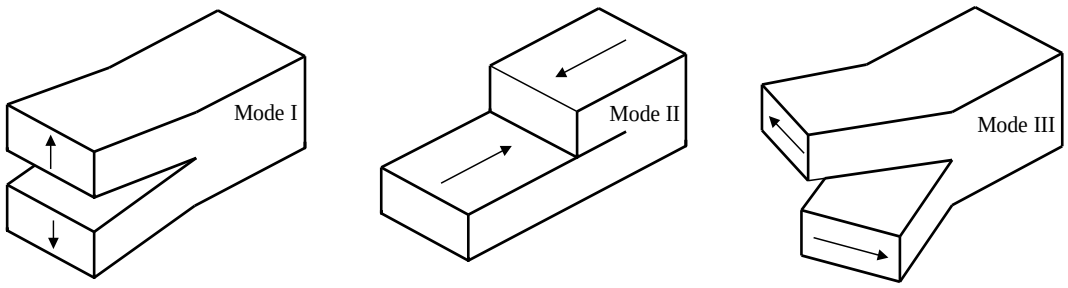

Figure 2.1 Modes of crack deformation

The location of the crack, being lateral on the shaft, and loading conditions during rotation, tension/compression, make deformation mode I the most dominant for cracked shafts in rotating machinery and this work will concentrate on this situation.

2.2 Weight Dominance

The presence of the crack in the rotating shaft changes the dynamic characteristics of the rotor as a result of the asymmetric cross-section at the crack location. Based on vibration amplitudes, crack may 1) always remain either opened or closed, or 2) open and close (i.e. breathe) once per shaft revolution. Breathing behavior of the cracked shaft is linked to a weight dominance condition. Figure 2.2(a) shows the model of the spinning cracked rotor with weight dominance. With weight dominance, static deflection of the rotating cracked shaft due to the gravity load is greater than the vibration amplitude of the cracked shaft due to unbalance force; therefore, the crack will open and close once per shaft revolution. On the other hand, when the vibration amplitude of the cracked rotor is greater than the static deflection of the rotor, then the crack will be always either opened or closed depending on a location and size of the unbalance. Figure 2.2(b) shows the

mechanism of the transverse crack opening and closing as a function of a shaft rotation due to weight dominance.

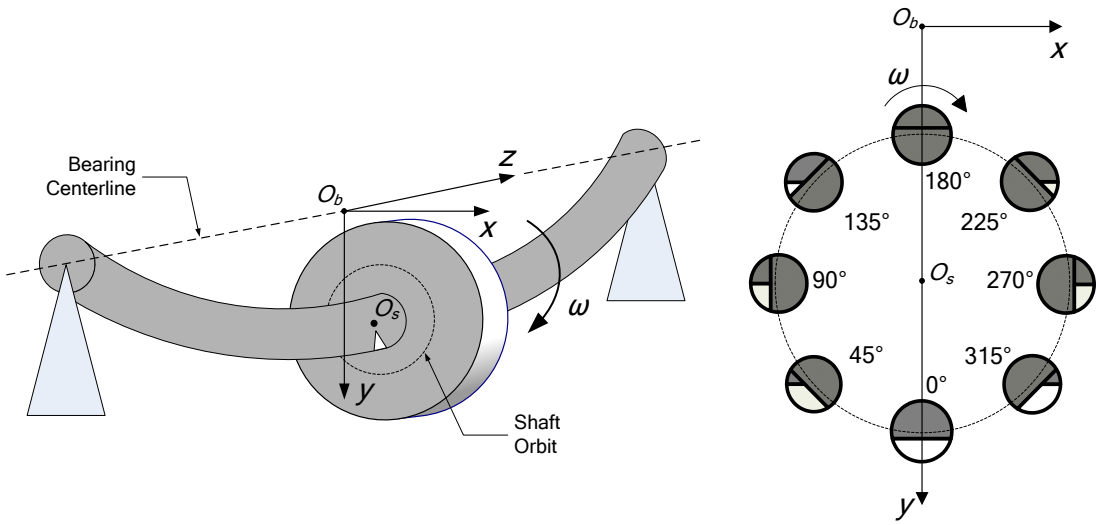

(a) **(b)**

Figure 2.2 Model of the spinning cracked rotor with weight dominance (a), opening and closing of the crack with weight dominance (b)

The downward direction along the vertical axis serves as a reference position and corresponds to 0º. The crack is open for a location below the centerline of the shaft as it is under tension force; therefore, there is maximum reduction in stiffness of a shaft. As a shaft rotates, the crack starts to close until it reaches its maximum state at 180º, which corresponds to a fully closed state of the crack; therefore, there is no reduction of stiffness and shaft behaves as uncracked. When a shaft further rotates, a crack starts to open until it reaches a fully open state at 360º and that completes the cycle. The crack detection technique presented in this work is based on the weight dominance assumption which will be validated in section 4.1.1.

2.3 Models of the Breathing Crack

The problem of the breathing crack was initially investigated by Gasch [Gasch, 1976]. He modeled the breathing crack using the simplest "hinge" model. In this model crack changes its state form closed to open and vice-versa abruptly as a shaft rotates. Namely, the crack is open for a first half of a shaft's revolution and closed for the other half. This behavior of a breathing crack Gasch described using a steering function, which is defined as follows:

$$f(\theta) = \begin{cases} 1 & \textit{for open crack} \\ 0 & \textit{for closed crack} \end{cases} \tag{2.1}$$

or, this function can be represented using Fourier cosine series expansion as:

$$f(\theta) = \frac{1}{2} + \frac{2}{\pi}\cos\theta - \frac{2}{3\pi}\cos 3\theta + \frac{2}{5\pi}\cos 5\theta - \ldots \tag{2.2}$$

The hinge model is a very good depiction for small (shallow) cracks; however, it is not appropriate representation for deep cracks. Mayes and Davies [Mayes, 1976, Mayes, 1980] used a cosine function to represent the model of the shaft with the deep breathing crack. The cosine function was used in order to account for the smooth transition between fully open and fully closed states of the deep crack. The crack steering function for this model $f(\theta)$, called the Mayes' modified function, takes the following form:

$$f(\theta) = \frac{1+\cos\theta}{2} \tag{2.3}$$

The opening and closing behavior of a crack using the hinge model for small crack and Mayes' modified function for deep crack is shown in Figure 2.3 below.

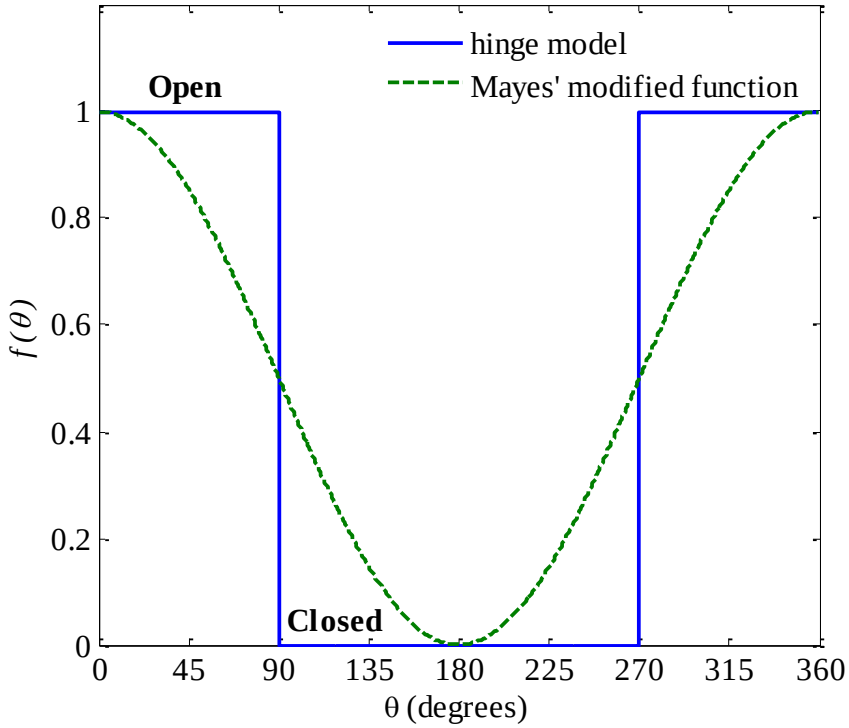

Figure 2.3 Opening and closing behavior of a crack using the hinge model and Mayes' modified function

2.4 Equations of Motion of a Cracked Rotor

In order to conduct a rotordynamic analysis of a rotor-bearing system, it is necessary to choose a coordinate system that will be used to derive the equations of motion. The analysis may be performed either in inertial or rotating coordinate frames. Since the rotor spins, it is advantageous to perform study on stiffness change due to opening and closing of the crack in the rotating frame, which is fixed to a rotor and rotates with it, and then transform obtained results to the inertial frame. Figure 2.4 shows a section of a rotor with a crack in inertial and rotating coordinate systems.

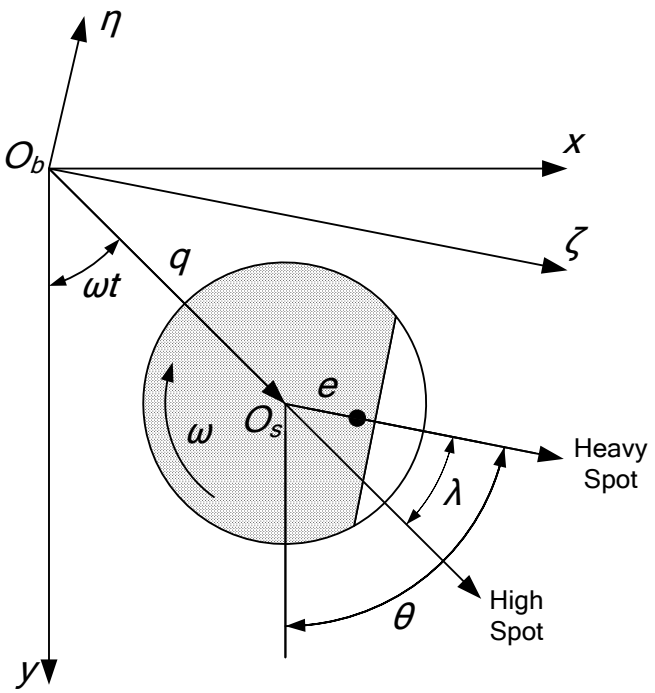

Figure 2.4 Section of a rotor with a transverse crack in inertial and rotating coordinate frames

The origins of the inertial (x, y) and rotating (ζ, η) coordinate systems are attached to a bearing centerline at a point O_b. The ζ-axis of the rotational frame always remains parallel to a crack centerline and the η-axis remains perpendicular to crack edge; therefore, rotor and coordinate system (ζ, η) constantly spin at the same velocity. The crack position with respect to a response vector (high spot) is determined by the angle λ, which depends on a speed of the rotor.

The equation of motion of the spinning undamaged Jeffcott rotor in the inertial coordinate frame is:

$$M\ddot{q} + C\dot{q} + Kq = F_{st} + F_{dy} \tag{2.4}$$

where M is a mass matrix, C is a damping matrix, K is a stiffness matrix, q is a position vector, F_{st} is a static component of the external force due to weight of the rotor, and F_{dy} is

a dynamic component of the external force due to unbalance. Equation (2.4) can be rewritten as:

$$\begin{bmatrix} m & 0 \\ 0 & m \end{bmatrix}\begin{bmatrix} \ddot{y} \\ \ddot{x} \end{bmatrix}+\begin{bmatrix} c & 0 \\ 0 & c \end{bmatrix}\begin{bmatrix} \dot{y} \\ \dot{x} \end{bmatrix}+\begin{bmatrix} k & 0 \\ 0 & k \end{bmatrix}\begin{bmatrix} y \\ x \end{bmatrix}=mg\begin{bmatrix} 1 \\ 0 \end{bmatrix}+me\omega^2\begin{bmatrix} \cos\omega t \\ \sin\omega t \end{bmatrix} \tag{2.5}$$

with

$$q=\begin{bmatrix} y \\ x \end{bmatrix} \tag{2.6}$$

Let the stiffness of the healthy rotor in rotating coordinate system be K_0^{rot} that can be expressed in a matrix form as follows:

$$K_0^{rot}=\begin{bmatrix} k_\zeta & 0 \\ 0 & k_\eta \end{bmatrix} \tag{2.7}$$

where k_ζ is a stiffness in ζ-direction and k_η is a stiffness in η-direction. Rotation of the cracked rotor with weight dominance results in a periodic change in the stiffness of the rotor; therefore, the stiffness of the cracked rotor can be written as:

$$K^{rot}=\begin{bmatrix} k_\zeta & 0 \\ 0 & k_\eta \end{bmatrix}-f(\theta)\begin{bmatrix} \Delta k_\zeta & 0 \\ 0 & \Delta k_\eta \end{bmatrix} \tag{2.8}$$

where Δk_ζ and Δk_η are changes in stiffness due to presence of the crack in weaker and stronger axes respectively, and $f(\theta)$ is a steering function that describes the opening and closing behavior of the crack. In the present work the Mayes' modified function for deep cracks from eq. (2.3) utilized as a steering function. From figure 2.4, the angle θ can be described as:

$$\theta=\omega t+\lambda \tag{2.9}$$

Assume the rotor spins at the constant speed ω; therefore, the angle θ becomes a function of time and the stiffness of the cracked rotor can be expressed as a function of time as follows:

$$K^{rot}(t)=\begin{bmatrix} k_\zeta & 0 \\ 0 & k_\eta \end{bmatrix}-f(t)\begin{bmatrix} \Delta k_\zeta & 0 \\ 0 & \Delta k_\eta \end{bmatrix} \tag{2.10}$$

The transformation matrix is used in order to convert the stiffness matrix of the cracked rotor from rotational to inertial coordinate system:

$$\begin{bmatrix} \zeta \\ \eta \end{bmatrix}=\begin{bmatrix} \cos\omega t & \sin\omega t \\ -\sin\omega t & \cos\omega t \end{bmatrix}\begin{bmatrix} y \\ x \end{bmatrix} \tag{2.11}$$

or

$$\begin{bmatrix} \zeta \\ \eta \end{bmatrix}=T\begin{bmatrix} y \\ x \end{bmatrix} \tag{2.12}$$

Thus the stiffness matrix of the cracked rotor can be written in stationary coordinate system as:

$$K(t)=T^T\begin{bmatrix} k_\zeta & 0 \\ 0 & k_\eta \end{bmatrix}T-T^T\left(f(t)\begin{bmatrix} \Delta k_\zeta & 0 \\ 0 & \Delta k_\eta \end{bmatrix}\right)T \tag{2.13}$$

or

$$K(t)=\begin{bmatrix} k_y & 0 \\ 0 & k_x \end{bmatrix}-f(t)\begin{bmatrix} \Delta k_y & 0 \\ 0 & \Delta k_x \end{bmatrix} \tag{2.14}$$

Substituting the stiffness matrix of the cracked rotor eq. (2.14) into the equation of motion of the healthy rotor eq. (2.5), the equation of motion of the cracked rotor in the inertial coordinate system becomes:

$$\begin{bmatrix} m & 0 \\ 0 & m \end{bmatrix}\begin{bmatrix} \ddot{y} \\ \ddot{x} \end{bmatrix}+\begin{bmatrix} c & 0 \\ 0 & c \end{bmatrix}\begin{bmatrix} \dot{y} \\ \dot{x} \end{bmatrix}+\left(\begin{bmatrix} k & 0 \\ 0 & k \end{bmatrix}-f(t)\begin{bmatrix} \Delta k & 0 \\ 0 & \Delta k \end{bmatrix}\right)\begin{bmatrix} y \\ x \end{bmatrix}=mg\begin{bmatrix} 1 \\ 0 \end{bmatrix}+me\omega^2\begin{bmatrix} \cos\omega t \\ \sin\omega t \end{bmatrix} \tag{2.15}$$

or simply

$$M\ddot{q} + C\dot{q} + K(t)q = F_{st} + F_{dy} \tag{2.16}$$

The crack detection technique used in the present work is based on the injection of the external excitation force applied on the rotor by AMB; therefore, the external force applied on the cracked rotor has to be included in the equations of motion. Thus the equation of motion of the cracked rotor can be expressed as follows:

$$M\ddot{q} + C\dot{q} + K(t)q = F_{st} + F_{dy} + F_{AMB} \tag{2.17}$$

where F_{AMB} is an external AMB force applied on the cracked rotor. In this thesis, an external excitation force will be chosen to be a sinusoidal force which is described as:

$$F_{AMB} = A_{AMB} \sin(\Omega_{AMB} t) \tag{2.18}$$

where A_{AMB} is the amplitude and Ω_{AMB} is the frequency of the external excitation force which will be discussed next.

2.5 Combinational Frequency Technique for Crack Detection

There are many techniques for detection of faults in rotating machinery. However, recently there is a trend toward utilization of AMBs as force actuators for crack detection in rotating shafts. The idea of the combinational frequency technique is when the external excitation force applied on the rotor, the presence of the breathing crack generates combinational frequencies corresponding to the injected AMB force frequency, natural frequencies of the system and the rotor spin speed. Mani et al. [Mani, 2005, Mani, 2006] and Quinn et al. [Quinn, 2005] determined necessary conditions for combinational frequencies using multiple scale analysis. Combinational frequencies occur with:

$$\Omega = |n\omega - \omega_i| \text{ for } n = \pm 1,\ \pm 2,\ \pm 3, \ldots \tag{2.19}$$

where Ω is the excitation frequency, ω_i is the i^{th} natural frequency of the system, and ω is the rotational speed of the rotor. The external AMB force with any calculated frequency when applied on the rotor induces combinational frequencies corresponding to the injected AMB frequency, the rotor spin speed and natural frequencies of the system.

CHAPTER III

MODELING AND SIMULATION OF THE EXPERIMENTAL CRACKED ROTOR

3.1 Introduction

In the present thesis the finite element method was used to develop the detailed model of the actual experimental rotor-bearing system with the breathing transverse crack. The finite element model consists of 48 Timoshenko beam finite elements with 8 degrees-of-freedom each and takes into account rotational inertia and shear deformation effects. Also, the model accounts for gyroscopic effects. The rotor consists of the solid circular shaft, a disk and two conical magnetic rotors of AMBs. The shaft is 15.9 mm in diameter and its length is 660.4 mm. The disk has a diameter of 127 mm and a thickness of 30.5 mm. Two identical conical rotors of AMBs have 13˚ cone angle and the 42.9 mm diameter at the center of actuation. The table with complete geometry of the finite element model is shown in Appendix A. Figure 3.1 shows the actual experimental rotor and the finite element model of the rotor.

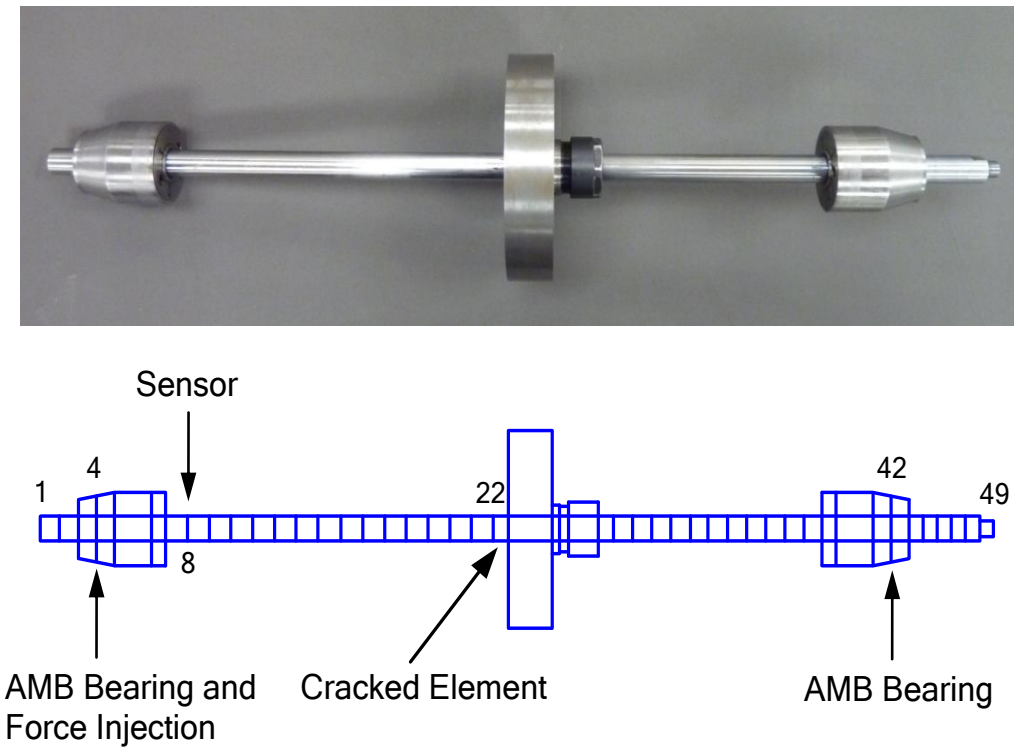

Figure 3.1 The experimental rotor and the finite element model of the experimental rotor

The disk is modeled at the 23rd element, and the crack is located next to the disk at the 22nd element. AMB supports are modeled at nodes 4 and 42 and the AMB force excitation is modeled at the node 4. Also, the unbalance of 0.003 kg-m is modeled at the node 23 and a damper of value 10 N-s/m is added at the location of the disk at node 24. Node 8 is selected to be a position of sensing for signal processing. The rotor is composed of the 400 series hardened stainless steel with corresponding physical properties shown in Table I below.

Table I Physical properties of the experimental rotor

Physical Property	Value
Density	7800 kg/m^3
Modulus of Elasticity	200 GPa
Shear Modulus	83 GPa
Poisson Ratio	0.3
Mass of the Disk	3.18 kg

For the operating conditions corresponding to the tested case, the equivalent stiffness and damping of magnetic bearings were found to be about 2×10^5 N/m and 500 N-s/m respectively. The method for determination of the effective stiffness and damping of active magnetic bearings comprehensively described in Appendix D.

3.2 Rotordynamic Analysis of the Modeled System

The main aspect of the rotordynamic analysis is to determine critical speeds of the rotor-bearing system that help to identify the operational speed region of the system and possible mode shapes. The rotordynamic analysis of the modeled rotor-bearing system was performed using XLRotor software version 3.75 developed by Rotating Machinery Analysis, Inc. XLRotor software is based on the finite element method. The analysis consists of the Campbell diagram, undamped critical speed map and mode shapes of the rotor. The Campbell diagram presents the number of critical speeds and change of frequency modes due to induced gyroscopic effects with respect to the rotational speed of the rotor. The resonance speeds for backward and forward whirls can be identified at

points of intersection of the dashed line with lines corresponding to each frequency mode. The Campbell diagram for the modeled rotor-bearing system is shown in Figure 3.2 below.

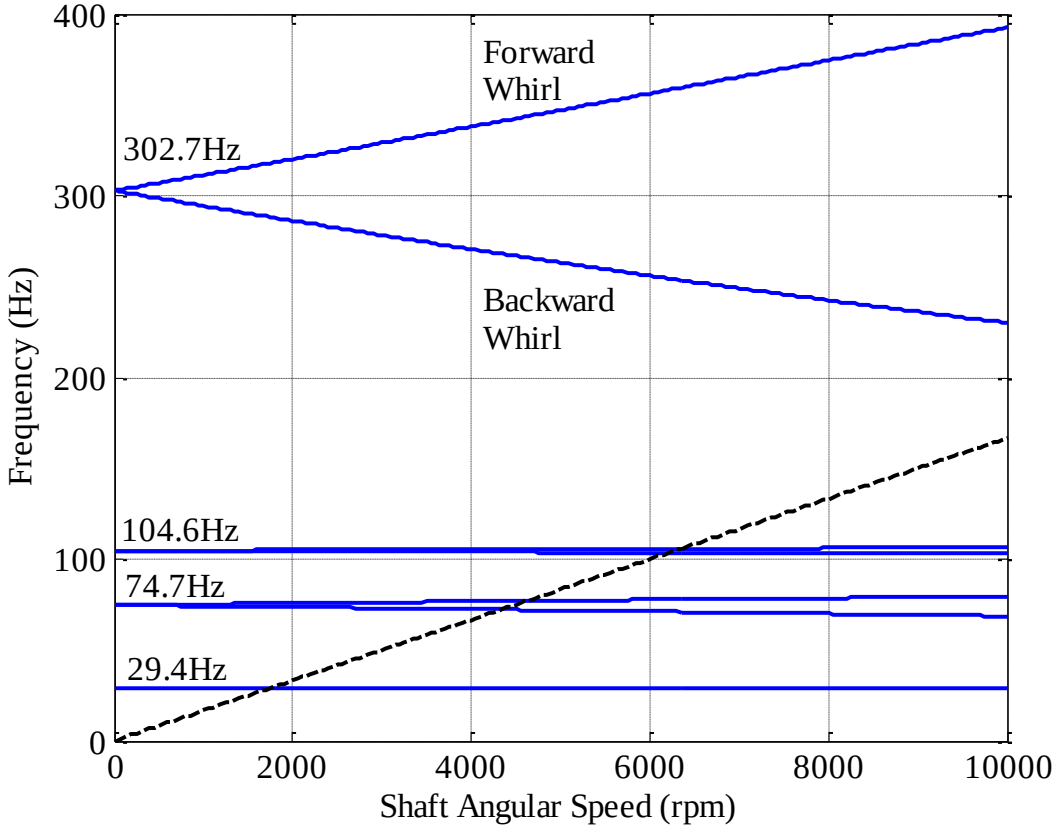

Figure 3.2 Campbell diagram for the modeled rotor

The natural frequencies of the modeled rotor-bearing system were found to be 29.4 Hz, 74.7 Hz, 104.6 Hz, and 302.7 Hz. These values agreed well with experimental results obtained using actual rotor-bearing system and which are shown in the following Chapter IV.

The undamped critical speed map is another tool which helps to identify critical speeds of the system. The undamped critical speed map shows the behavior of the critical

speeds as a function of the actual support stiffness. The critical speeds can be obtained by superimposing actual bearing stiffness over frequency mode curves. Figure 3.3 shows the undamped critical speed map of the modeled rotor-bearing system.

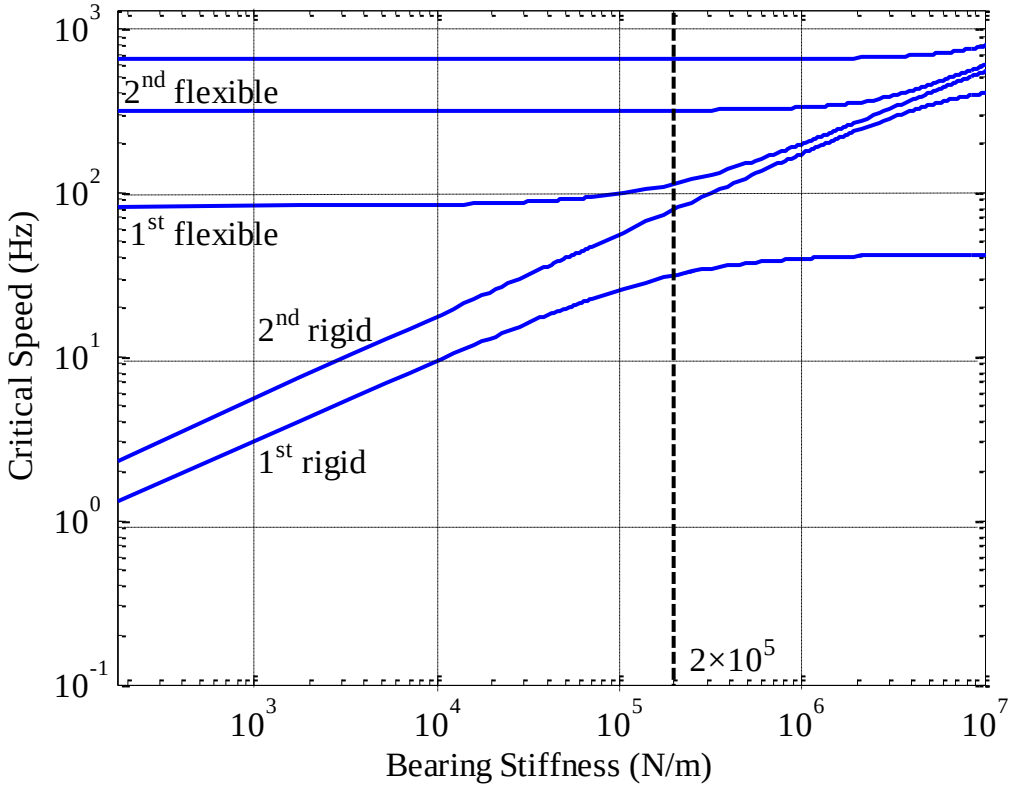

Figure 3.3 Undamped critical speed map

From the undamped critical speed map, in order for critical speeds values to be equal to ones found in Campbell diagram, the bearing stiffness has to be about 2×10^5 N/m. This value of the stiffness is in well agreement with the bearing stiffness value found using method described in Appendix D. This confirms the method of determination of stiffness coefficients of the AMB.

The mode shape is a pattern that describes the deflection shape of the system due to vibration. Figure 3.4 shows the visualization of the first four mode shapes of the modeled rotor calculated at a rotational speed of 1560 rpm.

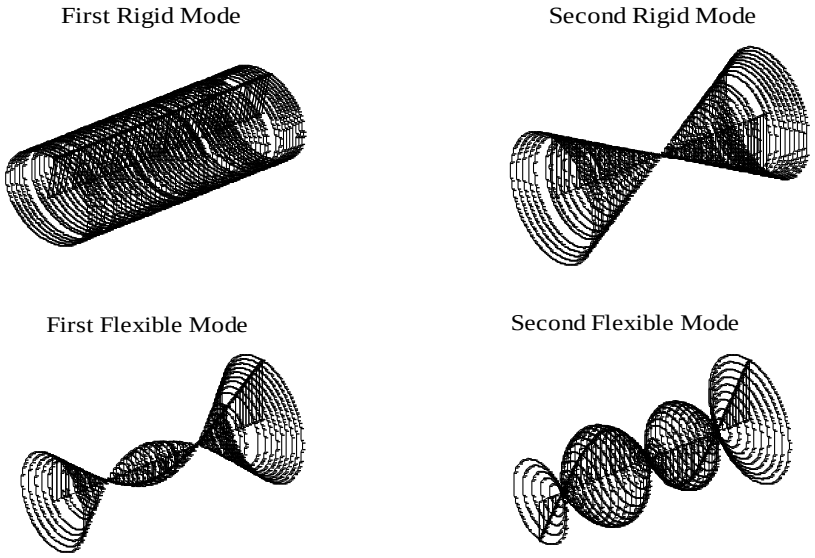

Figure 3.4 Mode shapes of the rotor

Due to low stiffness, active magnetic bearings are not rigid supports but have some flexibility; therefore, the first two modes are rigid-body modes and next two are flexible modes.

3.3 Computer Simulations of the Modeled System

The crack modeling procedure presented in section 2.4 was applied to the finite element model in order to simulate a behavior of the breathing crack. The reduction of stiffness due to fully-open 25% diameter crack was modeled by reducing the cracked element stiffness by 25% in the direction perpendicular to the crack edge and 12.5% in the direction parallel to the crack edge. The reduction of stiffness due to fully-open 40%

diameter crack was modeled by reducing the cracked element stiffness by 40% and 20% in the directions perpendicular and parallel to the crack edge respectively. MATLAB software was used to perform simulations. In order to be able to compare the simulated and experimental results, computer simulations were conducted for the operating conditions and parameters corresponding to the experimental case. The spin speed of the rotor for all simulation trials was 1560 rpm (26 Hz). Combinational frequencies for first three critical speeds were calculated using equation (2.19) and provided in Table II below. Note that combinational frequencies listed in this table were calculated using experimentally extracted natural frequencies which are discussed in Chapter IV.

Table II Calculated combinational frequencies

n value	**Running Speed (Hz)**	**Combinational Frequency (Hz)**		
		First Rigid ω_{n1} = 29.7 Hz	Second Rigid ω_{n2} = 70.6 Hz	First Flexible ω_{n3} = 102.1 Hz
-4	26	133.7	174.6	206.1
-3	26	107.7	148.6	180.1
-2	26	81.7	122.6	154.1
-1	26	55.7	96.6	128.1
0	26	29.7	70.6	102.1
1	26	3.7	44.6	76.1
2	26	22.3	18.6	50.1
3	26	48.3	7.4	24.1
4	26	74.3	33.4	1.9
5	26	100.3	59.4	27.9
6	26	126.3	85.4	53.9
7	26	152.3	111.4	79.9
8	26	178.3	137.4	105.9

Frequencies of 18.6 Hz, 22.3 Hz, and 50.1 Hz, corresponding to $n = 2$, were used as excitation frequencies for the first, second and third injection trials respectively. The amplitude of the externally injected sinusoidal AMB force was chosen to be 5 N which corresponds to the amplitude of the external excitation force used in the experimental trials.

Since the vibration signals of the complex structures often contain more than one frequency component, it is convenient to analyze these signals in the frequency domain. In order to analyze the vibration signal in the frequency domain, the Fast Fourier Transform (FFT) spectrum analysis was used. Figures 3.5, 3.6 and 3.7 show simulated frequency responses of the healthy, 25% cracked and 40% cracked rotors respectively.

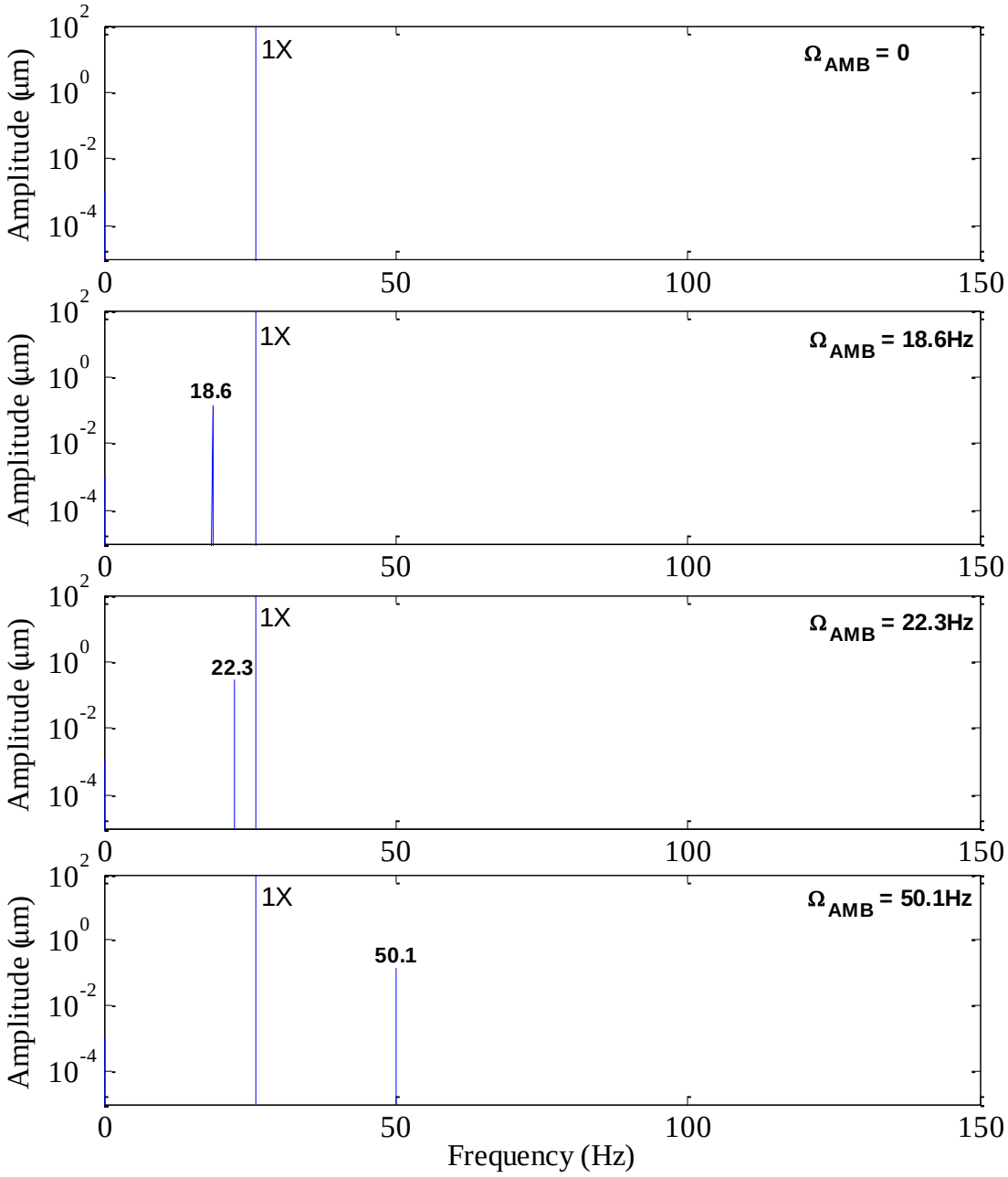

Figure 3.5 Simulated frequency responses of the healthy rotor at spin speed ω = 26 Hz without and with excitation force of 5 N with various frequencies

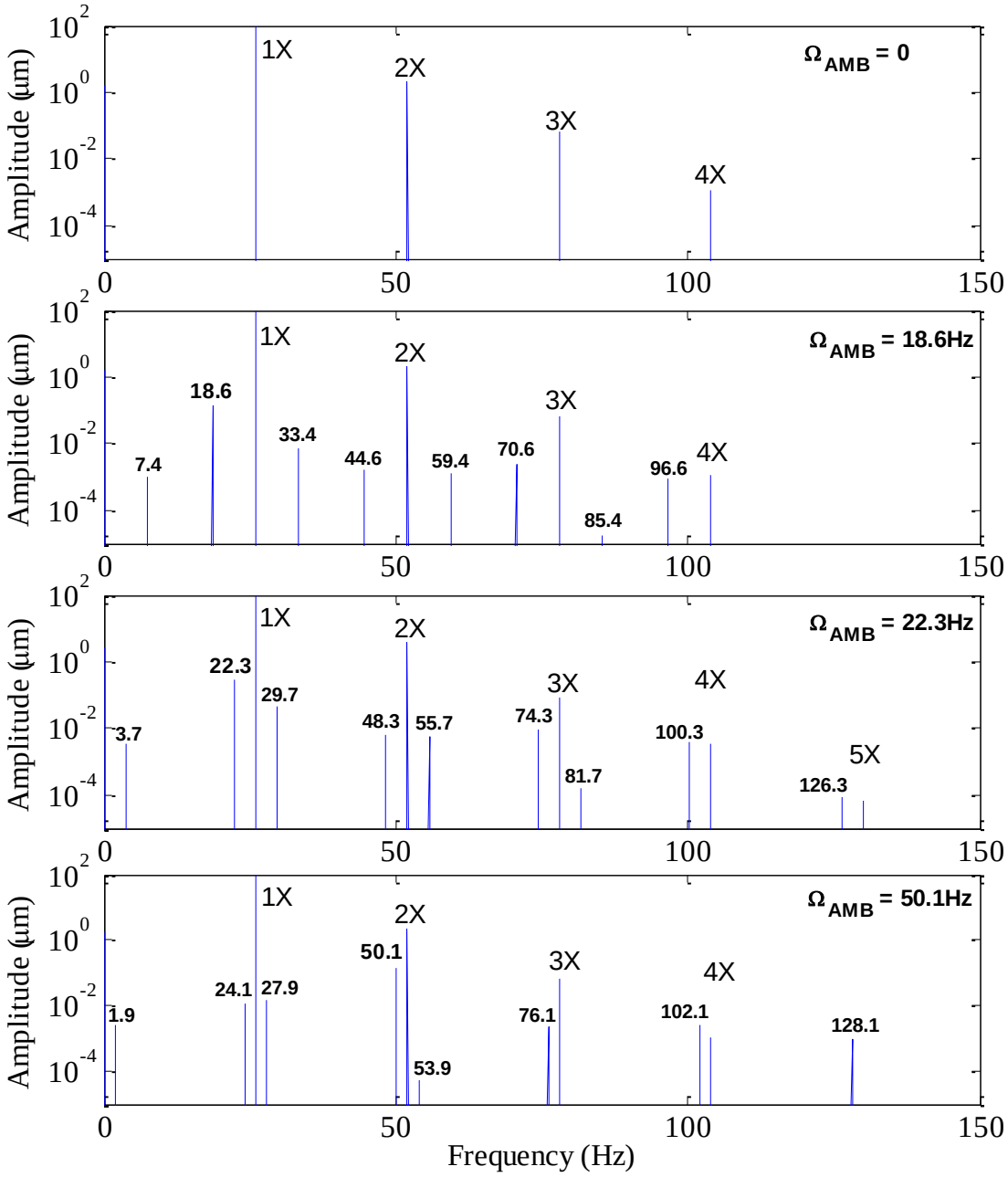

Figure 3.6 Simulated frequency responses of the 25% cracked rotor at spin speed ω = 26 Hz without and with excitation force of 5 N with various frequencies

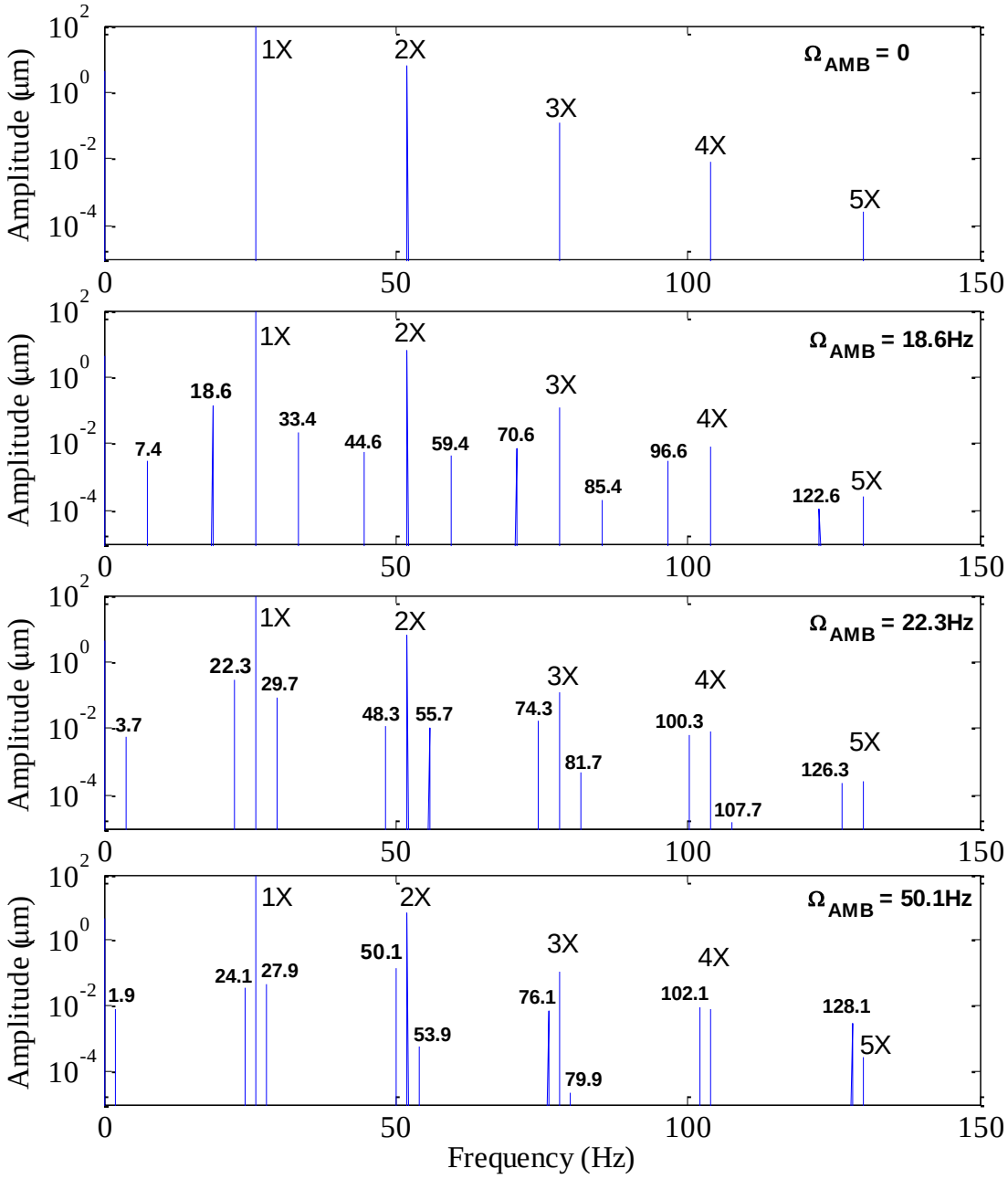

Figure 3.7 Simulated frequency responses of the 40% cracked rotor at spin speed ω = 26 Hz without and with excitation force of 5 N with various frequencies

In Figure 3.5 for the case with no external excitation force ($\Omega_{AMB} = 0$), the only response is at the rotor running speed of 26 Hz or 1X. In this case, the healthy rotor is excited only by a rotating unbalance force at frequency of 26 Hz; therefore, there is only one peek at 26 Hz. The other three plots in this figure represent the cases with different frequency injections. Now, each plot shows the frequency response of the uncracked rotor, which contains the corresponding injection frequency as well as the rotor spin frequency.

In Figure 3.6 for the case without an external excitation force, the frequency response of the 25% cracked rotor consists of the rotor spin frequency and its harmonics (2X, 3X, 4X, 5X) due to the presence of the crack. The other three plots in this figure correspond to the cases with 18.6 Hz, 22.3 Hz and 50.1 Hz frequency injections. These three plots present the frequency responses with each containing a number of unique combinational frequencies, in addition to the corresponding injection frequency, rotor spin frequency and multiples of the spin frequency. These combinational resonances provide unique signatures of a crack.

Figure 3.7 shows the frequency responses of the 40% cracked rotor. The frequency responses of the 40% cracked rotor are similar to the corresponding frequency responses of the 25% cracked rotor with a small difference in response amplitudes. Response amplitudes of the 40% cracked rotor are higher than the corresponding amplitudes of the 25% cracked rotor, which was expected due to the higher asymmetric stiffness in 40% cracked rotor when compared with the 25% cracked rotor.

CHAPTER IV

EXPERIMENTAL SETUP, PROCEDURE AND RESULTS

4.1 Experimental Crack Detection Test Rig

The experimental crack detection rotor test stand employed in this study was manufactured by SKF Magnetic Bearings a Unit of SKF Canada Limited. The experimental crack detection rotor test rig is shown in Figure 4.1 below.

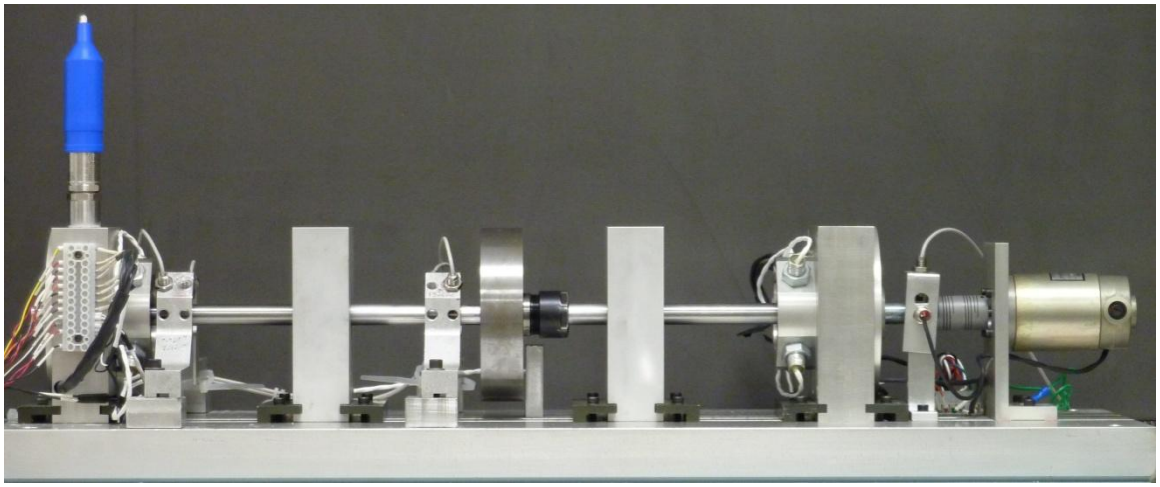

Figure 4.1 Experimental crack detection test rig

The rig consists of an aluminum base plate, 48 VDC brush type motor, a shaft, a disk, two identical conical AMBs equipped with two conical hydraulic rotors. The shaft connected to the motor using a lightweight, flexible coupling which allows axial and radial displacements of the shaft. Figure 4.2 shows the general assembly of the experimental crack detection rotor test rig with some dimensions. Note that dimensions are given in millimeters (mm).

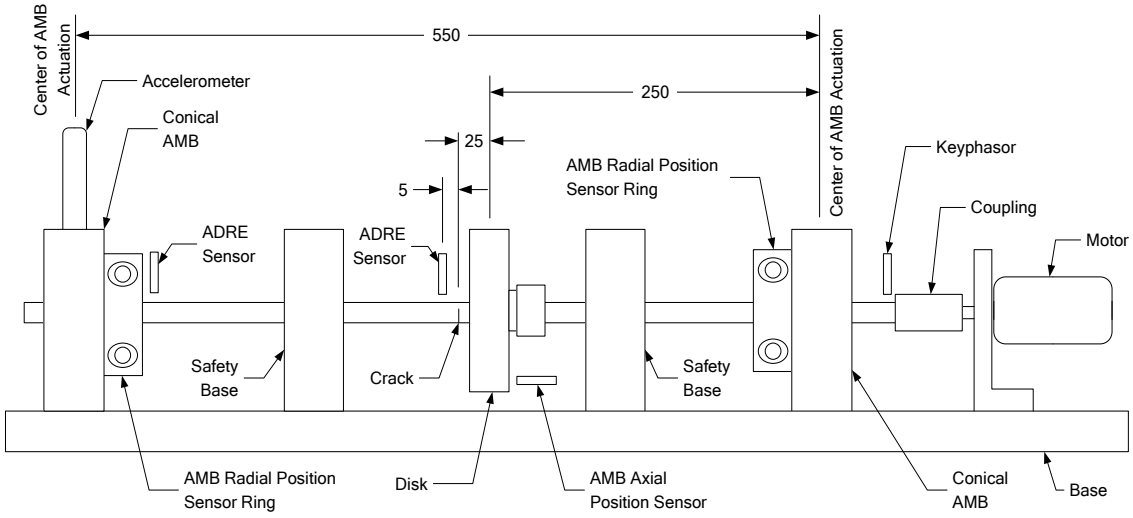

Figure 4.2 General assembly of the crack detection test rig

4.1.1 Rotor

The experimental rotor consists of the shaft, two conical magnetic rotors and a disk. The solid circular shaft is 15.9 mm in diameter and 660.4 mm in length. The shaft is composed of the 416 hardened stainless steel. The disk has a diameter of 127 mm and a thickness of 30.5 mm. The mass of the disk is 3.18 kg. Two identical conical rotors of AMBs composed of Arnon 5 and have 13˚ cone angle and 42.9 mm diameter at the center

of AMB actuation. Note that the present study on breathing crack is based on the weight dominance assumption. In order to show that the current configuration of the crack detection test rig falls under the weight dominance condition, the commercial computer-aided design software SolidWorks was utilized. Figure 4.3 shows the visualization of the static deflection of the rotor supported on active magnetic bearings.

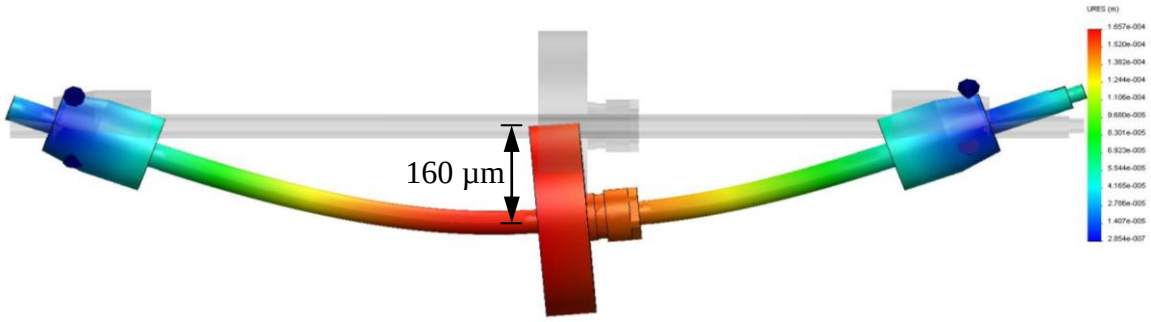

Figure 4.3 Static deflection of the rotor due to gravity

The peak amplitude of the static deflection of the rotor at the crack location is found to be roughly 160 µm. The peak amplitude of the experimentally obtained orbit of 40% cracked shaft was found to be approximately 70 µm; therefore, the current configuration of the crack detection test rig corresponds to the weight dominance condition.

In the present experimental work, in order to imitate a behavior of a real lateral crack, two shafts, one with a narrow lateral notch having the depth equal to a 25% of the shaft diameter and one with a narrow lateral notch having the depth equal to a 40% of the shaft diameter, were tested. Both notches of approximately 115 µm in width were made in the shafts at the bearing midspan using an electrical discharge machine (EDM). In theory, an actual crack would have a width of zero; therefore, a stainless steel shim was inserted into the 25% and 40% EDM cuts in order to mimic the opening and closing behavior of the

real crack as close as possible. Magnified images of the EDM cut with no shim and with the inserted shim are shown in Figures 4.4(a) and 4.4(b) respectively.

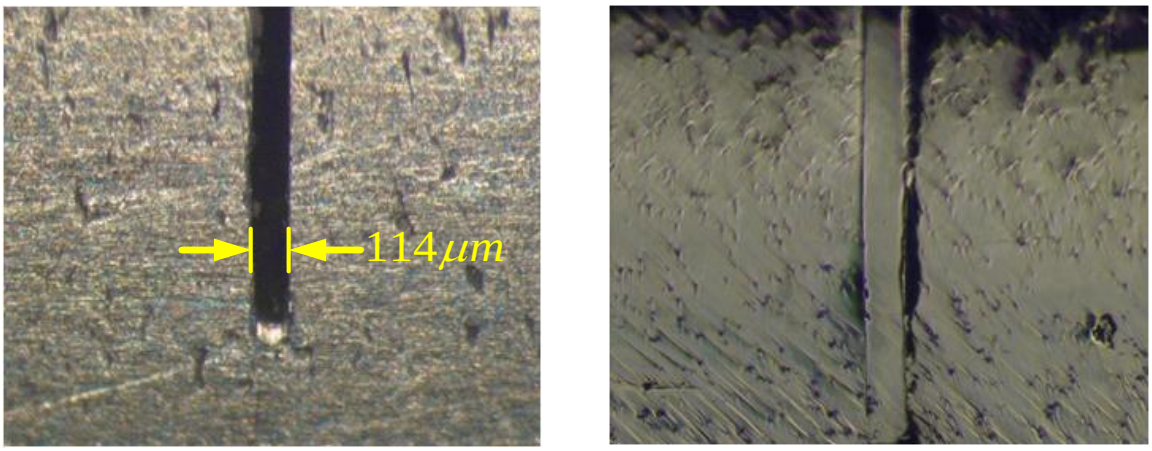

(a) **(b)**

Figure 4.4 Magnified view of the shaft with the EDM cut: (a) with no shim and (b) with a shim

4.1.2 Conical AMBs

Conical AMBs serve as rotor supporting bearings as well as actuators for injection of the specially designed excitation force. The main advantage of conical AMBs over radial AMBs is that conical bearings can provide radial and axial forces simultaneously; therefore, there is no need for an extra AMB for axial support of the rotor. Each conical bearing consists of a cone-shaped stator based on an 8-pole radial design, a cone-shaped rotor with 13˚ cone angle, and a sensor ring equipped with four variable reluctance type position sensors. In addition, each AMB has a backup touchdown ball bearing which is used when the AMBs are inactive or during an upset condition. Both stator and rotor consist of a stack of laminated layers which are used to reduce eddy current losses and to

improve the response of the bearing. Figures 4.5 and 4.6 show a cone-shaped rotor and a conical AMB housing respectively.

Figure 4.5 Cone-shaped AMB rotor

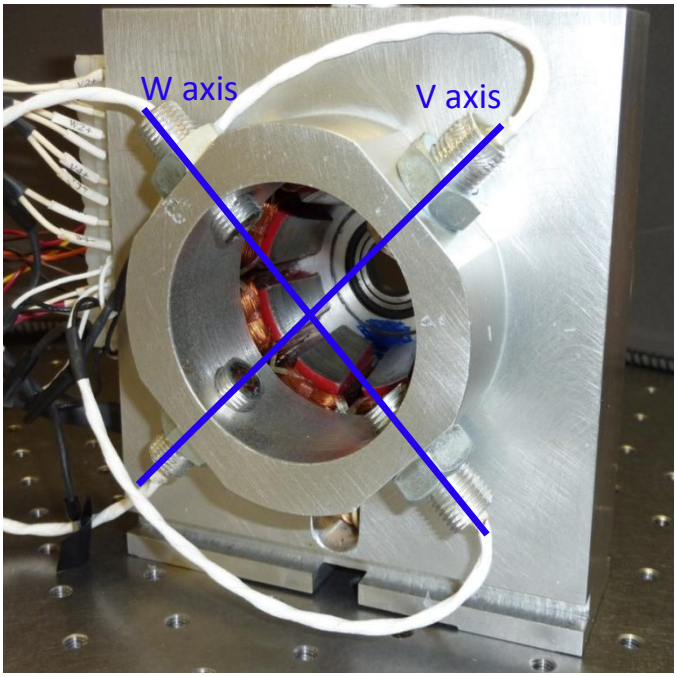

Figure 4.6 Conical AMB housing

Electromagnetic forces are applied to the rotor along two perpendicular axes V and W, which are aligned 45° from the vertical. The line of action of these forces is inclined at 13° from the plane perpendicular to the bearings centerline due to a cone angle of the

magnetic bearing rotor. Figure 4.7 illustrates the convention used for axes orientation in a 5-axis magnetic bearing system.

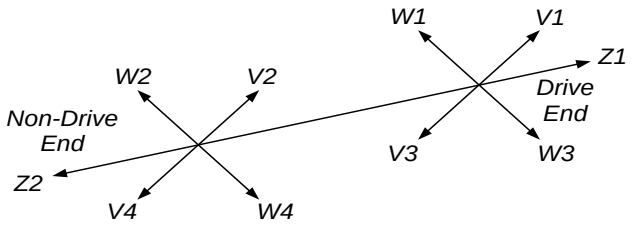

Figure 4.7 Axes orientation in a 5-axis magnetic bearing system

The static load capacity of AMBs is 266 N and a dynamic load capacity is 48 N at 1000 Hz. The nominal air gap of the magnetic bearings is 381 µm and the gap between the auxiliary bearings and the landing sleeves on the shaft is 190 µm.

4.1.2.1 Modeling and Control of the System with Conical AMBs

Consider a symmetrical rigid rotor supported simultaneously laterally and axially using two conical AMBs, as shown in Figure 4.8.

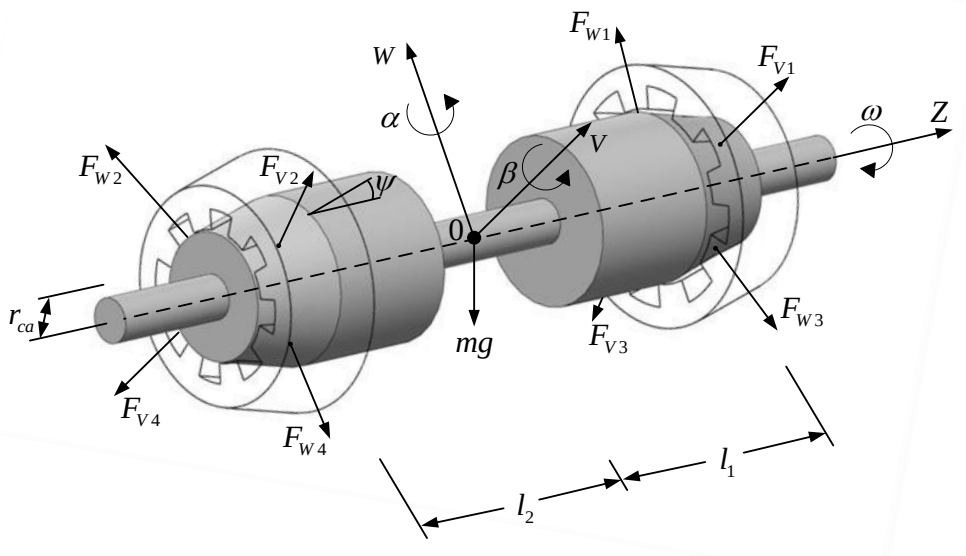

Figure 4.8 Configuration of a rotor suspended on conical AMBs

From the Newton's second law, the equations of translatory motion of the rotor can be derived in the following form:

$$\begin{aligned} m\ddot{W} &= \left(F_{W1} - F_{W3} + F_{W2} - F_{W4}\right)\cos\psi - \frac{\sqrt{2}}{2}mg \\ m\ddot{V} &= \left(F_{V1} - F_{V3} + F_{V2} - F_{V4}\right)\cos\psi - \frac{\sqrt{2}}{2}mg \\ m\ddot{Z} &= \left(F_{V1} + F_{W1} + F_{V3} + F_{W3}\right)\sin\psi - \left(F_{V2} + F_{W2} + F_{V4} + F_{W4}\right)\sin\psi \end{aligned} \tag{4.1}$$

while the equations of rotary motion of the rotor can be obtained from Euler's equations as:

$$\begin{aligned} I_t\ddot{\alpha} + I_p\omega\dot{\beta} &= F_{V1}\left(l_1\cos\psi - r_{ca}\sin\psi\right) + F_{V2}\left(r_{ca}\sin\psi - l_2\cos\psi\right) \\ &\quad + F_{V4}\left(l_2\cos\psi - r_{ca}\sin\psi\right) + F_{V3}\left(r_{ca}\sin\psi - l_1\cos\psi\right) \\ I_t\ddot{\beta} - I_p\omega\dot{\alpha} &= F_{W1}\left(l_1\cos\psi - r_{ca}\sin\psi\right) + F_{W3}\left(r_{ca}\sin\psi - l_1\cos\psi\right) \\ &\quad + F_{W4}\left(l_2\cos\psi - r_{ca}\sin\psi\right) + F_{W2}\left(r_{ca}\sin\psi - l_2\cos\psi\right) \end{aligned} \tag{4.2}$$

where: m - mass of the rotor, F_{Vj} and F_{Wj} - electromagnetic forces acting on a rotor in j-direction (j = 1, 2, 3, 4), ψ - cone angle of the rotor, l_1 and l_2 - distances between the rotor mass center and the center of actuation of first and second AMBs respectively, g - gravitational constant, ω - rotational speed of the rotor, r_{ca} - radius of the rotor at the center of AMB actuation, I_t and I_p - transverse and polar moments of inertia respectively.

Based on the electromagnetic theory, the force produced by a single electromagnet of a radial bearing with four pole pairs can be expressed as [Schweitzer, 1993]:

$$F_{AMB} = \frac{1}{4}\mu_0 N^2 A\left(\frac{I}{s}\right)^2\cos\phi \tag{4.3}$$

where: μ_0 - magnetic field constant, N - number of turn per coil, A - the area of a pole face, $\phi = 22.5^\circ$ - pole centerline angle, I - coil current, and s - air gap between the stator and the rotor.

Equation (4.3) demonstrates that the electromagnetic force is a function of the coil current and the air gap; therefore, in order to derive magnetic forces generated by conical AMB, the changes in coil currents and air gaps have to be determined.

Consider the exaggerated motion of the rotor, as shown in Figure 4.9. Assume that the rotor's displacements from the equilibrium position are very small such that $\sin\alpha \approx \alpha$ and $\sin\beta \approx \beta$.

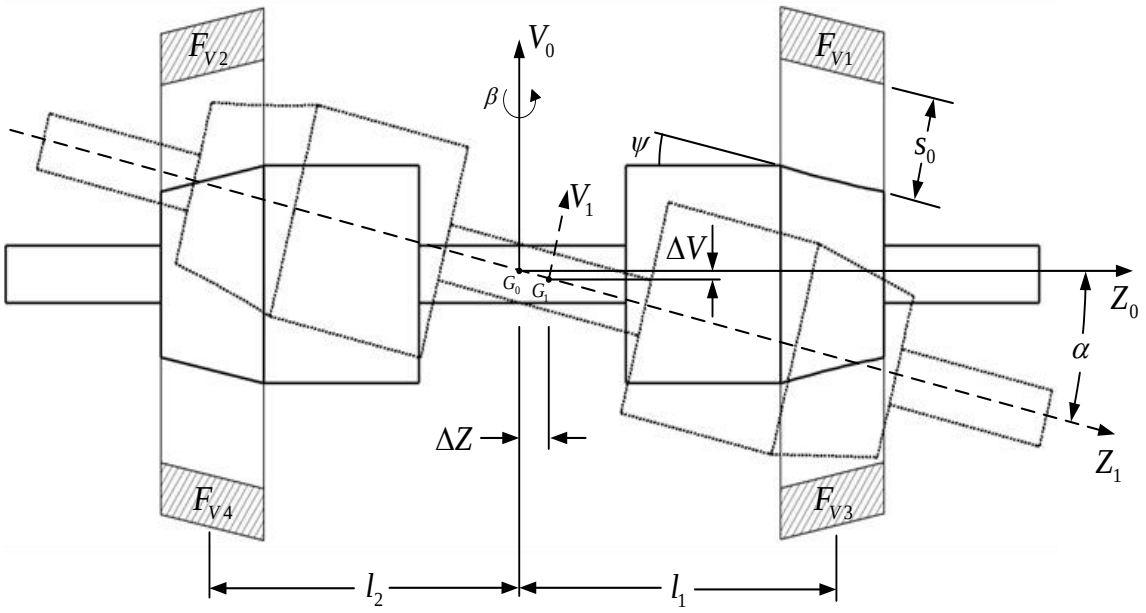

Figure 4.9 One-plane motion of the rotor suspended on two conical AMBs

Based on Figure 4.9, the air clearances between the rotor and the stator of the system with conical AMBs can be described as follows:

$$
\begin{aligned}
s_{V1} &= s_0 + \Delta V \cos\psi + l_1 \alpha \cos\psi - \Delta Z \sin\psi \\
s_{V2} &= s_0 + \Delta V \cos\psi - l_2 \alpha \cos\psi + \Delta Z \sin\psi \\
s_{V3} &= s_0 - \Delta V \cos\psi - l_1 \alpha \cos\psi - \Delta Z \sin\psi \\
s_{V4} &= s_0 - \Delta V \cos\psi + l_2 \alpha \cos\psi + \Delta Z \sin\psi \\
s_{W1} &= s_0 + \Delta W \cos\psi - l_1 \beta \cos\psi - \Delta Z \sin\psi \\
s_{W2} &= s_0 + \Delta W \cos\psi + l_2 \beta \cos\psi + \Delta Z \sin\psi \\
s_{W3} &= s_0 - \Delta W \cos\psi + l_1 \beta \cos\psi - \Delta Z \sin\psi \\
s_{W4} &= s_0 - \Delta W \cos\psi - l_2 \beta \cos\psi + \Delta Z \sin\psi
\end{aligned}
\tag{4.4}
$$

where: s_0 - nominal air gap, ΔV, ΔW, and ΔZ - lateral displacements of the rotor along *V*, *W*, and *Z*-axes respectively, and α and β - angular displacements of the rotor around *W* and *V*-axes respectively.

In order for AMBs to create a stable levitation of the rotor, the closed-loop control algorithm is implemented; therefore, any change of a rotor position results in change of coil currents. The levitation of the rotor using AMBs is most commonly performed with class A operation mode, i.e. a bias current with a constant value is applied to all coils and control current is added to a bias current in one coil and subtracted in the opposite coil. Since the configuration of electromagnets is identical for both levitation planes and the levitation planes mutually perpendicular, the same control principle applies to each plane. The schematic diagram of a one-plane control of the rotor suspended on two conical AMBs with class A operation mode is shown in Figure 4.10 below.

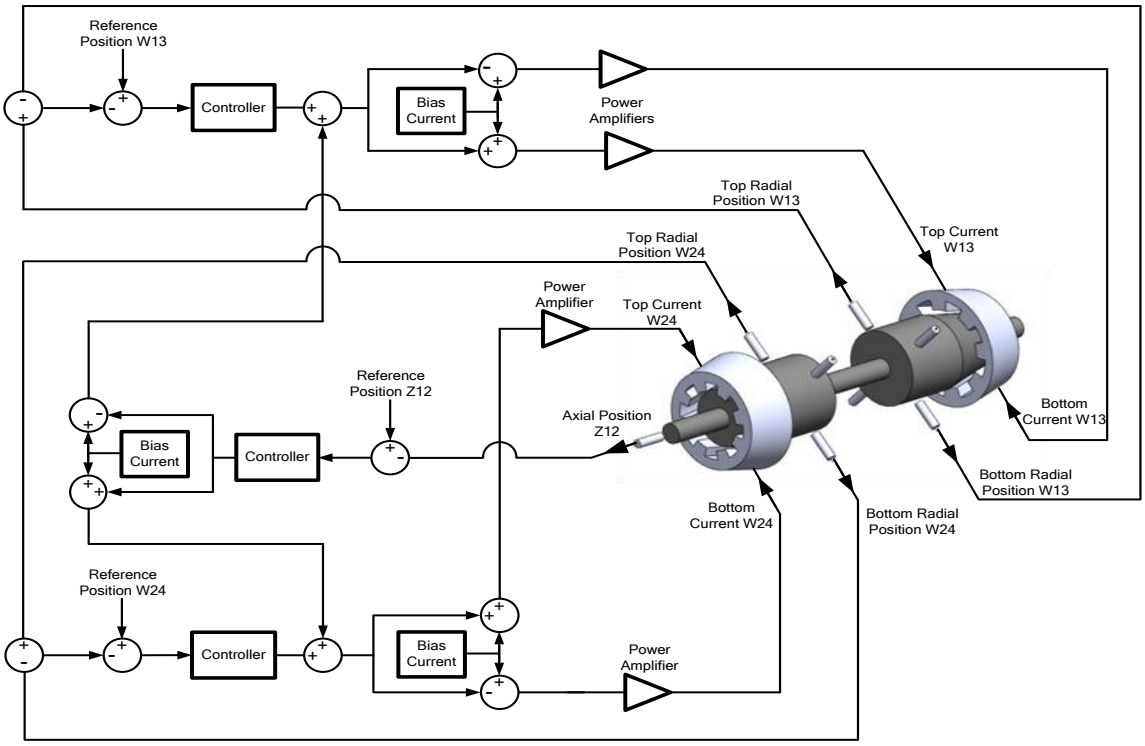

Figure 4.10 Schematic diagram of a one-plane control of the rotor suspended on conical AMBs

The shaft is affected by the forces generated by each magnetic pole of conical AMBs. Using conical AMBs, the magnetic force is divided into radial and axial force components that depend on a cone angle of the rotor; therefore, the radial position of the rotor is controlled by a radial component of the magnetic force and the axial position is controlled by an axial component of the magnetic force. As shown in Figure 4.10, each axis of levitation has its own controller. Based on position data received from the corresponding sensors, each controller calculates the amount of control current that needs to be added to or subtracted from the bias current in each coil. The total bias current, i.e. the sum of the radial and axial bias currents, is applied to all coils in both conical AMBs. At the same time, the axial control current is added to a total bias current in all coils of

one conical AMB and subtracted from a total bias current in all coils of another conical AMB such that the axial displacement of the rotor is controlled, whereas the radial control current is added in one coil and subtracted in the opposite coil of both AMBs such that the radial displacement of the rotor is controlled. In such manner, the rotor system with five degrees-of-freedom supported on two conical AMBs is fully controlled using only four magnetic coil pairs. As a result, coil currents can be expressed in the following way:

$$\begin{aligned}
I_{V1} &= I_0 - I_{c,V1}^r + I_{c,V1}^a \\
I_{V2} &= I_0 - I_{c,V2}^r - I_{c,V2}^a \\
I_{V3} &= I_0 + I_{c,V3}^r + I_{c,V3}^a \\
I_{V4} &= I_0 + I_{c,V4}^r - I_{c,V4}^a \\
I_{W1} &= I_0 - I_{c,W1}^r + I_{c,W1}^a \\
I_{W2} &= I_0 - I_{c,W2}^r - I_{c,W2}^a \\
I_{W3} &= I_0 + I_{c,W3}^r + I_{c,W3}^a \\
I_{W4} &= I_0 + I_{c,W4}^r - I_{c,W4}^a
\end{aligned} \tag{4.5}$$

with

$$I_0 = I_0^r + I_0^a \tag{4.6}$$

where: I_0^r and I_0^a - radial and axial bias currents, and I_c^r and I_c^a - radial and axial control currents respectively.

Substituting each corresponding term of equations (4.4) and (4.5) into equation (4.3), the forces produced by a system of two conical AMBs with four pole pairs each, as shown in Figure 4.8, can be written as:

$$
\begin{aligned}
F_{V1} &= \frac{1}{4}\mu_o N^2 A\left(\frac{I_0 - I^r_{c,V1} + I^a_{c,V1}}{s_0 + \Delta V\cos\psi + l_1\alpha\cos\psi - \Delta Z\sin\psi}\right)^2\cos 22.5^\circ \\
F_{V2} &= \frac{1}{4}\mu_o N^2 A\left(\frac{I_0 - I^r_{c,V2} - I^a_{c,V2}}{s_0 + \Delta V\cos\psi - l_2\alpha\cos\psi + \Delta Z\sin\psi}\right)^2\cos 22.5^\circ \\
F_{V3} &= \frac{1}{4}\mu_o N^2 A\left(\frac{I_0 + I^r_{c,V3} + I^a_{c,V3}}{s_0 - \Delta V\cos\psi - l_1\alpha\cos\psi - \Delta Z\sin\psi}\right)^2\cos 22.5^\circ \\
F_{V4} &= \frac{1}{4}\mu_o N^2 A\left(\frac{I_0 + I^r_{c,V4} - I^a_{c,V4}}{s_0 - \Delta V\cos\psi + l_2\alpha\cos\psi + \Delta Z\sin\psi}\right)^2\cos 22.5^\circ \\
F_{W1} &= \frac{1}{4}\mu_o N^2 A\left(\frac{I_0 - I^r_{c,W1} + I^a_{c,W1}}{s_0 + \Delta W\cos\psi - l_1\beta\cos\psi - \Delta Z\sin\psi}\right)^2\cos 22.5^\circ \\
F_{W2} &= \frac{1}{4}\mu_o N^2 A\left(\frac{I_0 - I^r_{c,W2} - I^a_{c,W2}}{s_0 + \Delta W\cos\psi + l_2\beta\cos\psi + \Delta Z\sin\psi}\right)^2\cos 22.5^\circ \\
F_{W3} &= \frac{1}{4}\mu_o N^2 A\left(\frac{I_0 + I^r_{c,W3} + I^a_{c,W3}}{s_0 - \Delta W\cos\psi + l_1\beta\cos\psi - \Delta Z\sin\psi}\right)^2\cos 22.5^\circ \\
F_{W4} &= \frac{1}{4}\mu_o N^2 A\left(\frac{I_0 + I^r_{c,W4} - I^a_{c,W4}}{s_0 - \Delta W\cos\psi - l_2\beta\cos\psi + \Delta Z\sin\psi}\right)^2\cos 22.5^\circ
\end{aligned}
\tag{4.7}
$$

The system of equations (4.7) was implemented in MATLAB/Simulink software in order to simulate the behavior of the experimental rotor magnetically supported using two conical AMBs and confirm the stability of the experimental system. The simulink model of the rotor suspended on conical AMBs is shown in Figure 4.11 below.

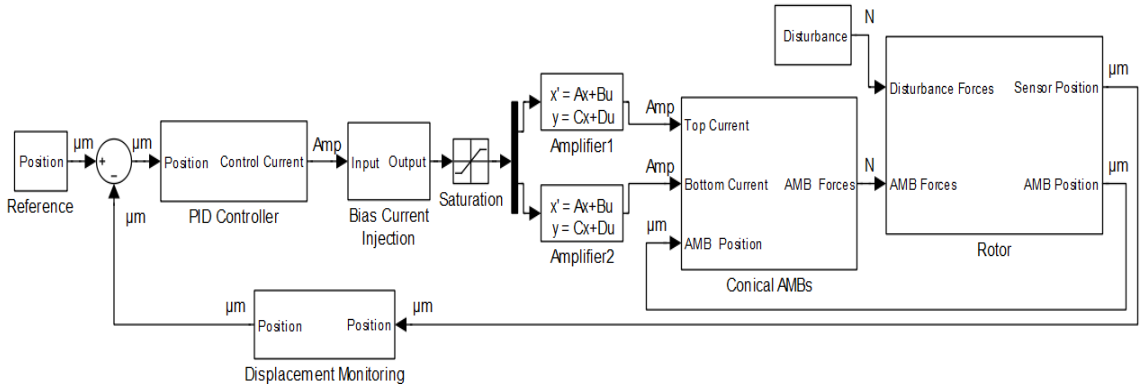

Figure 4.11 Simulink model of the rotor supported on conical AMBs

Figures 4.12 and 4.13 show simulink models of the conical AMBs and the bias current injection respectively. Theses figures correspond to blocks “Conical AMBs” and “Bias Current Injection” in Figure 4.10.

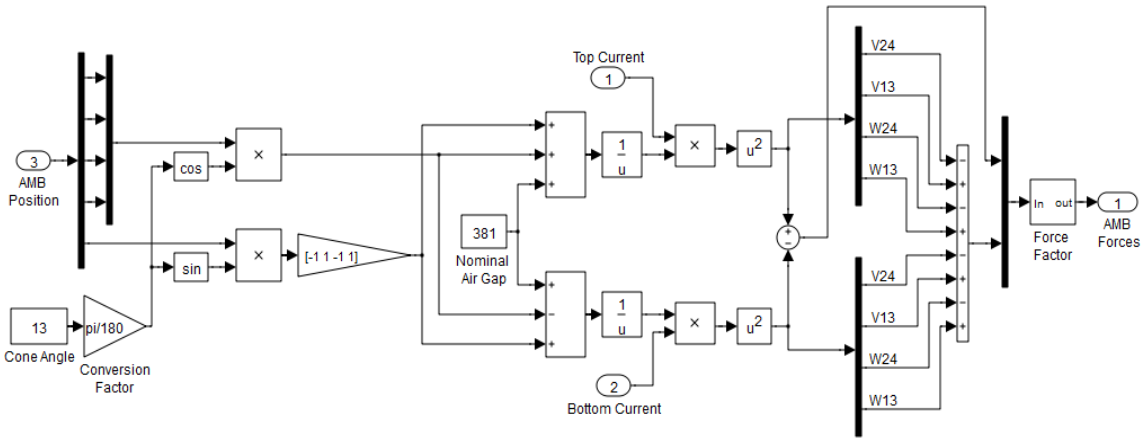

Figure 4.12 Simulink model of the conical AMBs

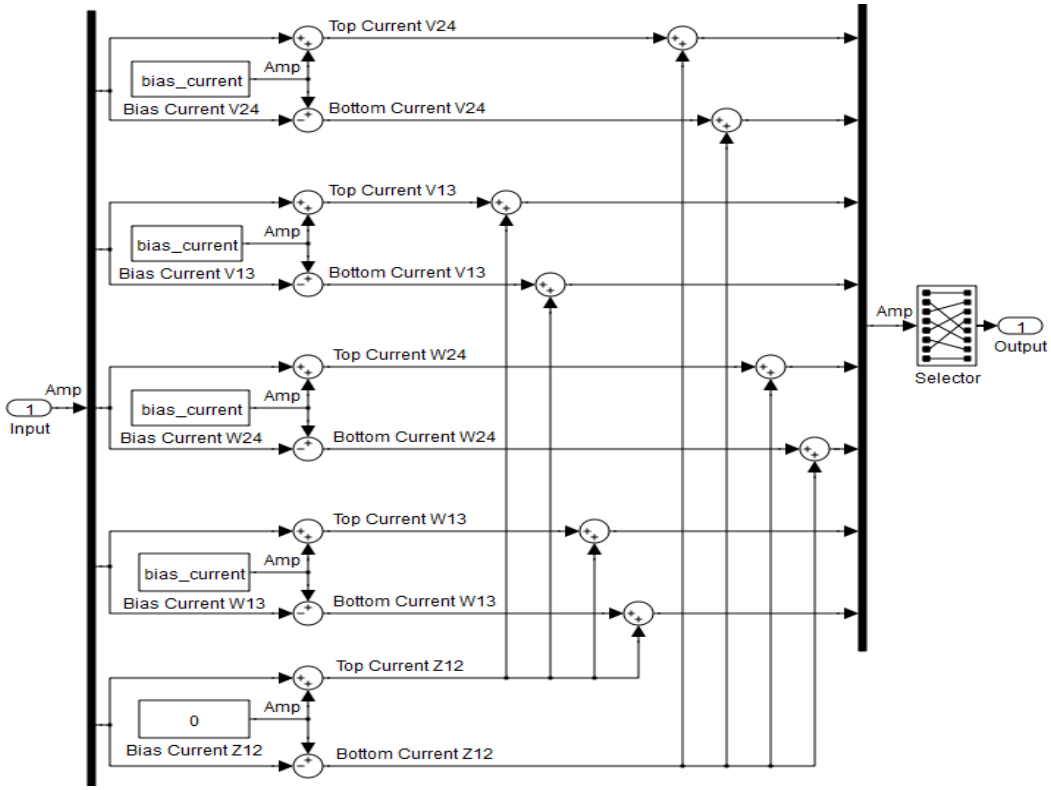

Figure 4.13 Simulink model of the bias current injection

4.1.2.2 PID Control of the Rotor System with AMBs

The simulated and experimental rotor-bearing system has five degrees-of-freedom, i.e. axis of levitation, each with its own controller. The controller transfer function $G(s)$ consists of the classical PID controller, low-pass filter and two notch filters. The transfer function of the PID controller in the Laplace domain can be expressed as:

$$G_{PID}(s) = K_P + \frac{K_I}{s} + K_D s \tag{4.8}$$

where K_P is a proportional gain, K_I is an integral gain, and K_D is a derivative gain of the PID controller. These three parameters were tuned in order to achieve a stable levitation performance of the experimental rotor.

A low-pass filter is a filtering device that passes signals with low-frequency components and attenuates signals with frequency components above selected cutoff frequency. The transfer function of a low-pass filter in the Laplace domain is given by:

$$G_{LP}(s) = \frac{\omega_{cutoff}^2}{s^2 + 2\zeta_{LP}\omega_{cutoff}s + \omega_{cutoff}^2} \tag{4.9}$$

where ω_{cutoff} is a cutoff frequency and ζ_{LP} is a damping ratio of a low-pass filter.

A notch filter is a device that passes all frequencies unchanged except the ones in a narrow frequency band that affect the stability of the system. A notch filter attenuates signals with unwanted frequencies to a very low level. The transfer function of the notch filter in the Laplace domain can be written as follows:

$$G_N(s) = \frac{s^2 + \omega_{notch}^2}{s^2 + 2\zeta_N\omega_{notch}s + \omega_{notch}^2} \tag{4.10}$$

where ω_{notch} is a notch frequency and ζ_N is a damping ratio of the notch filter.

The overall transfer function of the controller, which consists of all the above components connected in series, can be expressed as

$$G(s) = G_{PID}(s)G_{LP}(s)G_N(s)K_T \tag{4.11}$$

where K_T is a total gain of the controller that works as a scaling factor of the entire control loop. Table III lists controller parameters that were used in the simulation and experiment.

Table III Controller parameters

Controller Parameter	Value				
	V13 axis	W13 axis	V24 axis	W24 axis	Z12 axis
Bias Current (A)	1.2	1.2	1.2	1.2	0
Proportional Gain (A/μm)	70	70	70	70	100
Integral Gain (A/μm-s)	100	100	100	100	100
Derivative Gain (A-s/μm)	0.12	0.12	0.12	0.12	0.2
Total Gain	0.00006	0.00006	0.00006	0.00006	0.00002
LP Cutoff Frequency (Hz)	1200	1200	1200	1200	1200
LP Damping Ratio	0.707	0.707	0.707	0.707	0.707
Notch 1 Frequency (Hz)	300	300	300	300	0
Notch 1 Damping Ratio	0.4	0.4	0.4	0.4	0
Notch 2 Frequency (Hz)	500	500	500	500	0
Notch 2 Damping Ratio	0.4	0.4	0.4	0.4	0

Figure 4.14 shows the bode plot of the developed controller that was used for levitation of the simulated and experimental rotors.

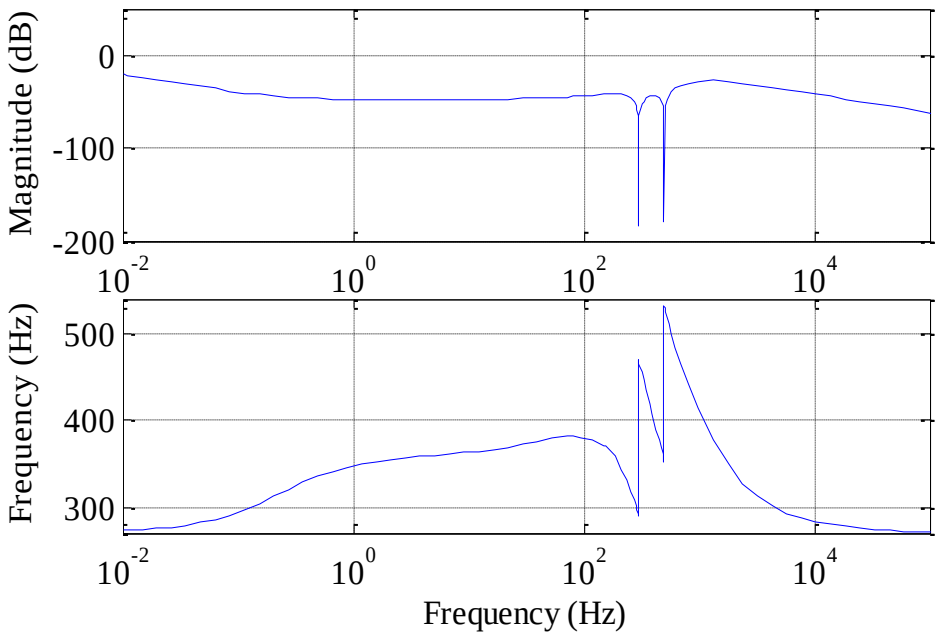

Figure 4.14 Bode plot of the developed controller

In order to verify the stability and robustness of the simulated rotor magnetically suspended on conical AMBs, a force input in a form of an impulse was applied to a non-rotating rotor at the V-axis of the non-drive end bearing at t = 1 second and the response was measured at the same location. The simulated impulse response of the magnetically levitated non-rotating rotor is shown in Figure 4.15. Also, an impulse was applied to a simulated rotor spinning at speed 1560 rpm and the impulse response of the rotor is shown in Figure 4.16.

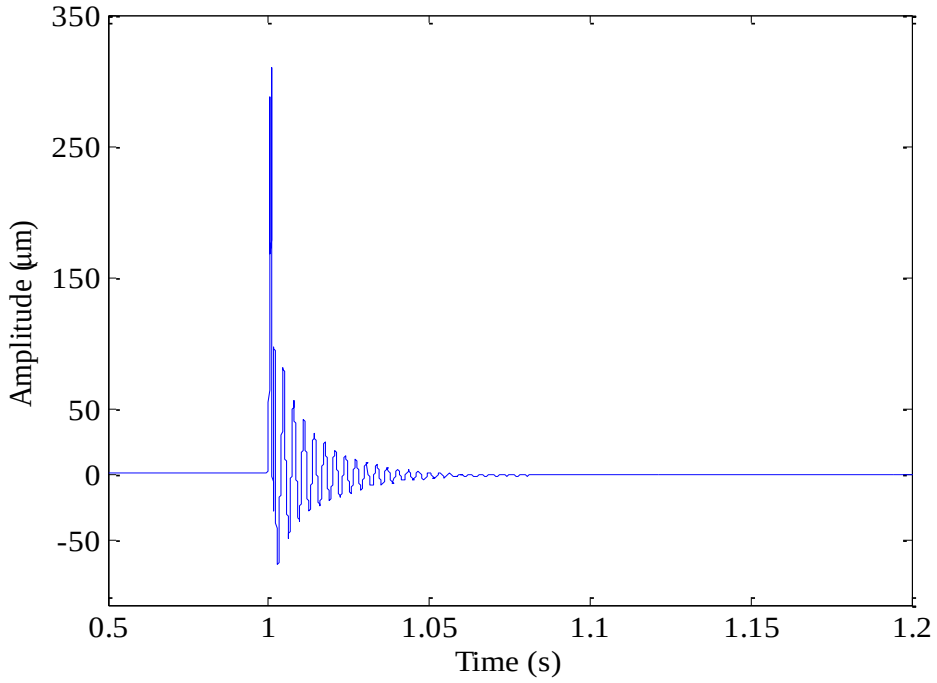

Figure 4.15 Impulse response of the simulated non-rotating rotor suspended on conical AMBs with impulse applied at the V-axis of the non-drive end bearing at t = 1 second

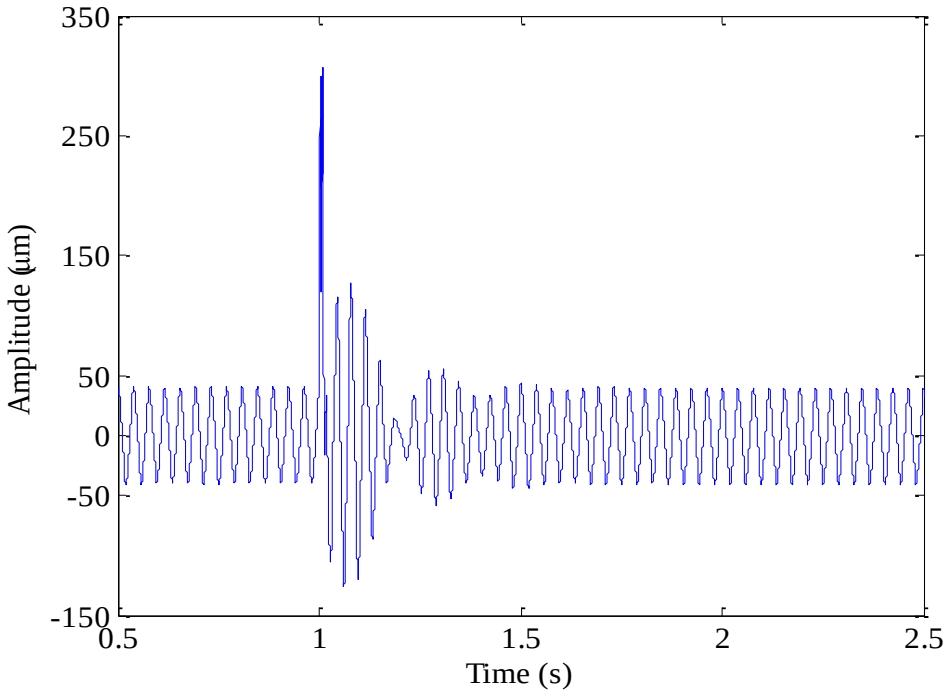

Figure 4.16 Impulse response of the simulated rotor suspended on conical AMBs at rotor spin ω = 1560 rpm with impulse applied at the V-axis of the non-drive end bearing at t = 1 second

Figure 4.17 shows simulated and measured time responses of the levitated rotor running at the speed 1560 rpm without and with an external harmonic force of 5 N applied at 18.6 Hz at the V-axis of the non-drive end bearing. For all cases, responses were measured with a position sensor located next to the non-drive end AMB and oriented along V-axis. For illustration purposes a time response only for one injection frequency is presented. The responses are very similar although the vibration amplitudes in the simulated case are slightly higher. This also applies for cases with 22.3 Hz and 50.1 Hz frequencies of injection.

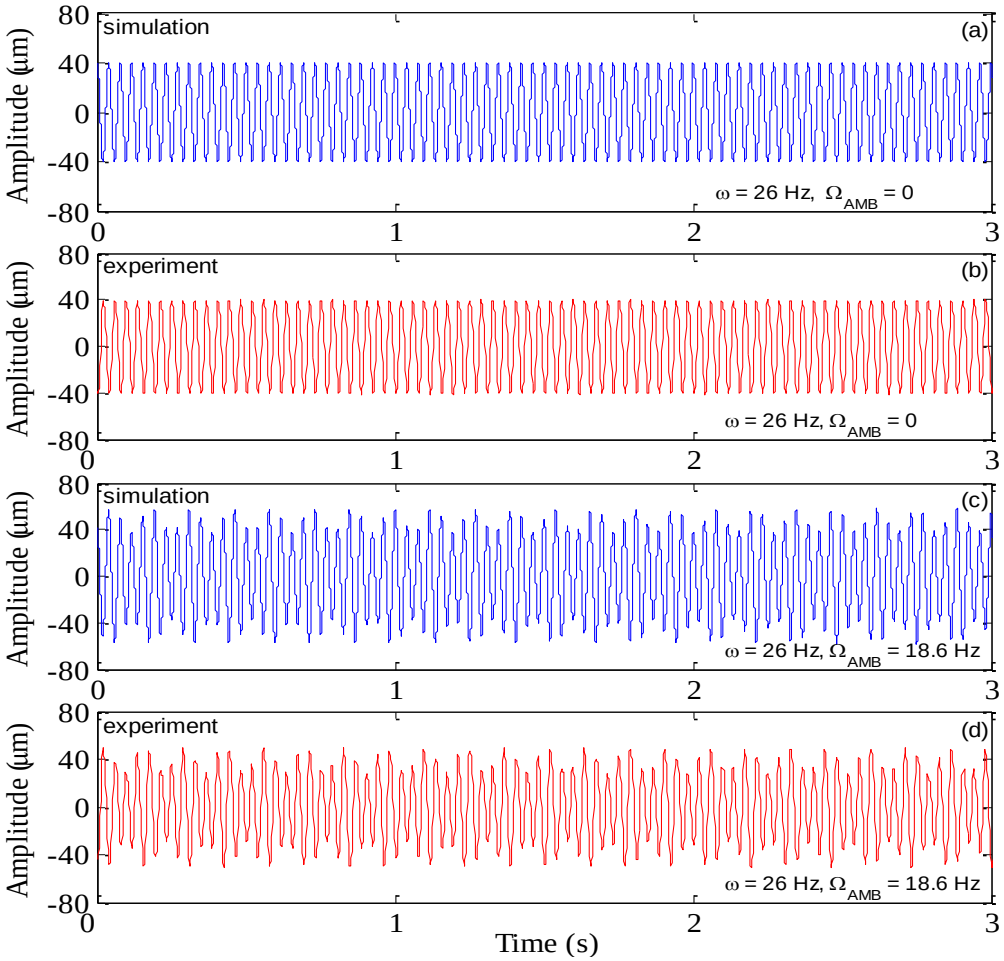

Figure 4.17 Simulated and experimental time responses of the rotor suspended on conical AMBs at spin ω = 1560 rpm: (a, b) without an additional harmonic force and (c, d) with an additional harmonic force of 5 N at 18.6 Hz applied at the V-axis of the non-drive end bearing

Figures 4.18 and 4.19 show simulated and measured orbits of the levitated rotor running at the speed 1560 rpm without and with external harmonic force respectively. The orbits were measured with a pair of sensors located next to the non-drive end AMB. The orbits are similar although the amplitudes in the W-axis in the simulated case are slightly higher than corresponding amplitudes in the experimental case.

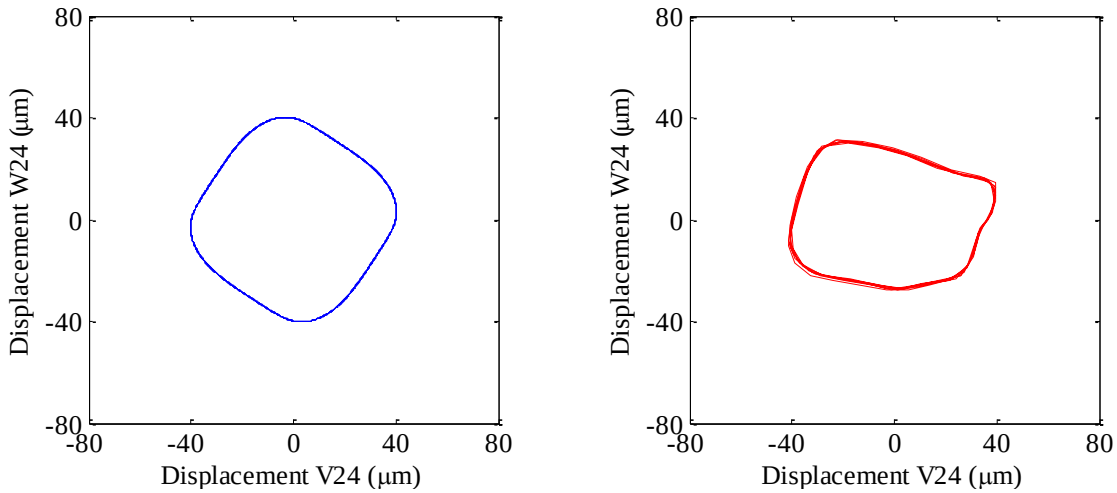

Figure 4.18 Orbits of (a) simulated and (b) experimental rotors suspended on conical AMBs at spin ω = 1560 rpm without an additional harmonic force

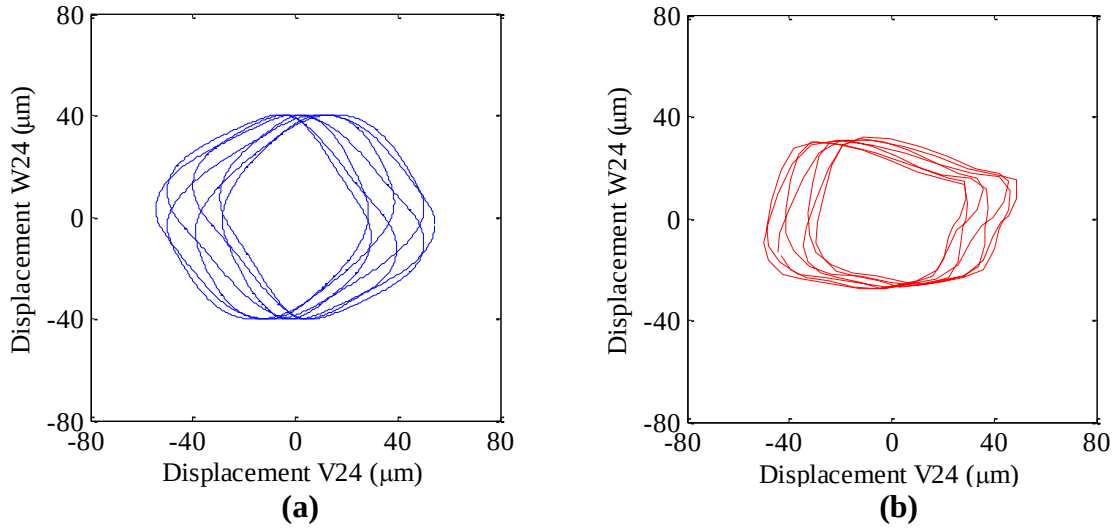

Figure 4.19 Orbits of (a) simulated and (b) experimental rotors suspended on conical AMBs at spin ω = 1560 rpm with an additional harmonic force of 5 N at 18.6 Hz applied at the V-axis of the non-drive end bearing

Figure 4.17, 4.18 and 4.19 demonstrate a good agreement of the model with the experimentally extracted data indicating that the method of modeling a system with conical AMBs described earlier is accurate to reproduce the experimental behavior of the shaft magnetically levitated using conical AMBs.

4.2 Experimental System Setup

The experimental system used in the present work consists of different components. The layout of the system is shown in Figure 4.20 below.

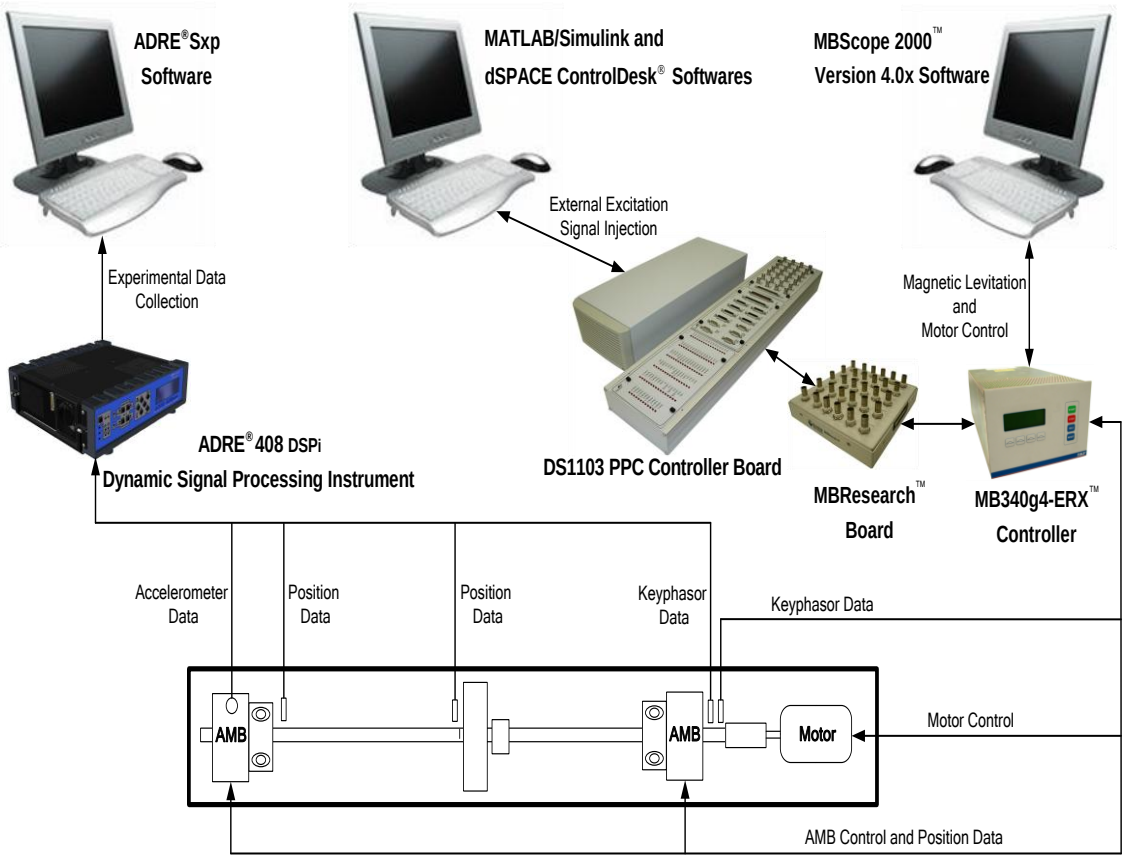

Figure 4.20 Experimental System Layout

The experiment was performed on the crack detection test rig. The magnetic levitation of the experimental rotor and its rotational speed are controlled using the MB340g4-ERX™ fully-digital, magnetic bearing controller. The controller is programmed with a PC which is equipped with the MBScope 2000™ version 4.0x software. The software consists of different graphical Tools, which are used to monitor and control system performance parameters such as position, current, and rotational speed. In addition to the levitation and rotation hardware, two independent systems are used. The first system is the ADRE data acquisition system which consists of the ADRE® 408 DSPi (Dynamic Signal Processing Instrument) and a PC equipped with the ADRE®Sxp software. This data acquisition system collects 6 channels of experimental data; five from Bently-Nevada® 3300 eddy current probes (four position data and one keyphasor data) and one from the Bently-Nevada® 330400 accelerometer. One pair of position probes is located next to the non-drive end AMB and another pair is located at the bearing midspan. Both pairs of position probes are oriented along two perpendicular axes V and W, which are aligned 45° from the vertical. The accelerometer is positioned on top of the non-drive end AMB housing. The second system is the dSPACE control prototyping system, which is used for external signal injection and connected to the MB340g4-ERX™ controller via a BNC connector module called MBResearch™. The dSPACE DS1103 PPC controller board is programmed by a PC via ControlDesk® software which allows MATLAB/Simulink external excitation force model to be implemented in real time. In order to create the external excitation force, a sinusoidal current of particular amplitude and frequency is superimposed on the total current of the levitated rotor via the V-axis of the non-drive

end bearing using dSPACE. With the complete experimental system setup, the test matrix is developed and it is shown in Appendix B.

4.3 System Identification of the Rotor

The system identification of the healthy experimental rotor was performed for two cases: 1) free-free rotor and 2) magnetically levitated rotor. The transfer function of the free-free rotor was measured using the impact hammer modal testing. A photo of an impact hammer test is shown in Appendix E. Particularly, the experimental rotor was suspended in the air using thin nylon wire and struck with the force-instrumented hammer. The resultant motion of the rotor was measured with an accelerometer fixed on the rotor and analyzed using the HP 35670A Dynamic Signal Analyzer. Figure 4.21 shows the transfer function of the experimental rotor obtained using an impact hammer test and transfer function of the FE model of the rotor.

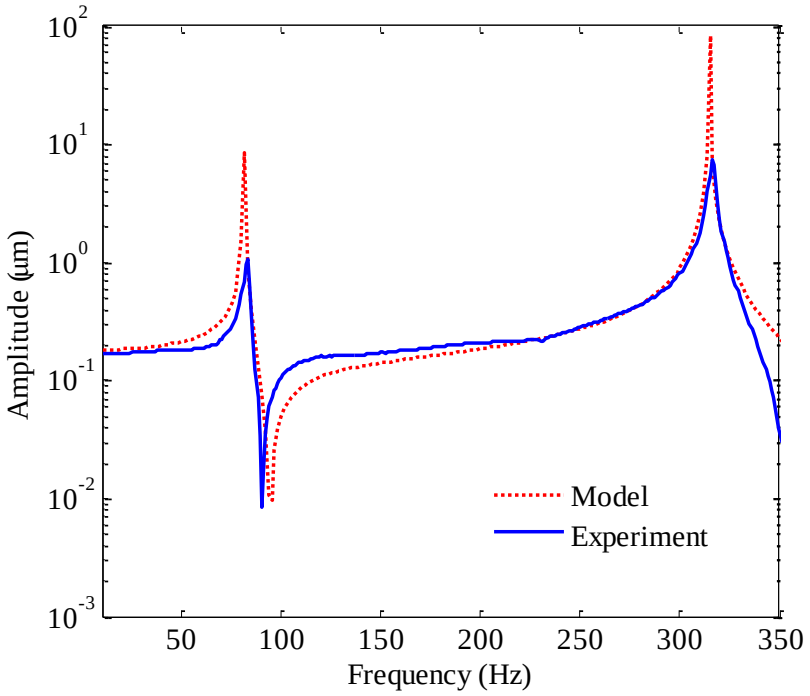

Figure 4.21 Transfer functions of the modeled and experimental free-free rotors

Figure 4.21 demonstrates a good agreement of a FE model with experimentally extracted data.

The transfer function of the levitated non-rotating rotor was measured using the Analyzer Tool of the MBScope software package. A sinusoidal current of 0.05 A amplitude was injected to a levitated rotor via V-axis of the non-drive end bearing over a 0 to 600 Hz frequency range and the amplitude of the rotor response was measured at each frequency. The transfer function between current disturbance and response of the rotor both measured at the same axis is shown in Figure 4.22 below.

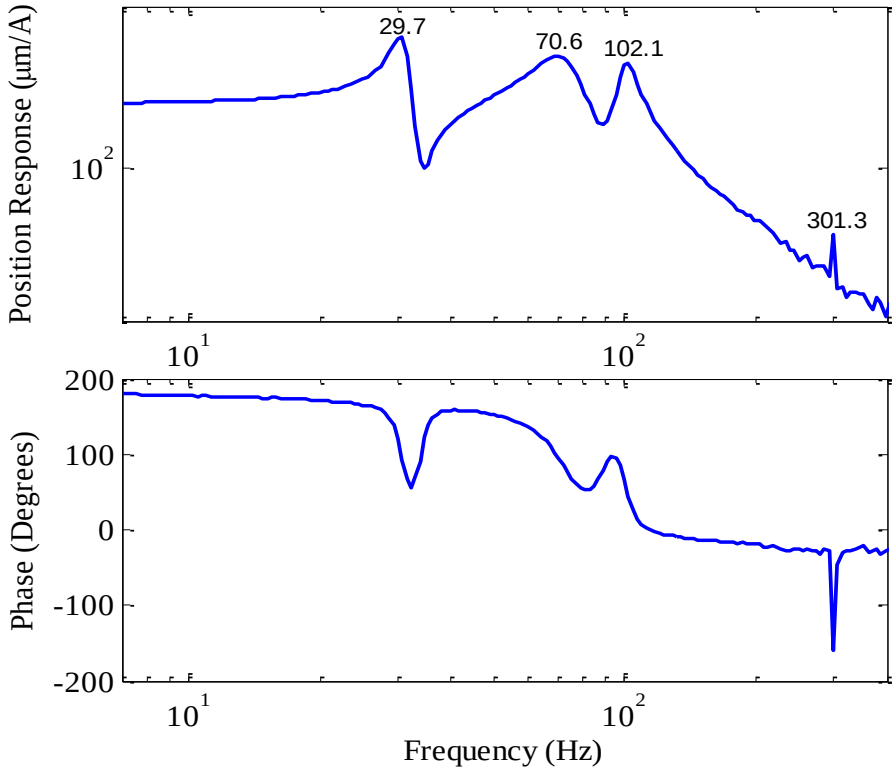

Figure 4.22 Bode plot of the experimental rotor suspended on conical AMBs

In Figure 4.22, the first two are the frequencies of rigid body modes and the third one is associated with the first bending mode. The experimentally obtained natural frequencies

of 29.7 Hz, 70.6 Hz, and 102.1 Hz are each utilized in the equation (2.19) to calculate the combinational frequencies used in the present crack detection work. The calculated combinational frequencies were previously shown in Table II located in Chapter III. Overall there are many frequencies that can be used as excitation frequencies; therefore, frequencies of 18.6 Hz, 22.3 Hz, and 50.1 Hz, corresponding to $n = 2$, were selected as excitation frequencies for the first, second and third injection trials respectively.

4.4 Experimental Results

For all presented experimental results the rotor is levitated on two AMBs and rotating at constant speed of 1560 rpm, which is equivalent to 26 Hz. The PID controller with notch and low-pass filters is implemented to provide stable and quiet levitation of the rotor over the range of speeds. The controller parameters were previously shown in Table III. The experimental data is obtained with two pairs of eddy-current position sensors. One pair of position sensors is located at the bearing midspan next to a crack location and another pair is positioned next to the non-drive end AMB, see Figures 4.1 and 4.2. Both pairs of position sensors are oriented along two perpendicular axes V and W, which are aligned 45° from the vertical.

For all experimental trials, the combinational frequency peaks were found to be more apparent in the data collected from the sensors aligned in plane with the axis used for excitation force injection; therefore, only data obtained from the sensors oriented in the V-axis is presented in this work.

In order to create an external excitation force, the external sinusoidal current of 0.12 A amplitude with particular frequency is added to the levitation current (bias plus control)

in the V-axis of the non-drive end bearing; therefore, the external excitation force is generated along the V-axis of the non-drive end AMB. The line of action of this force is inclined at 13° from the plane perpendicular to the bearings centerline due to the cone-shape of the magnetic bearing rotor. As it was mentioned earlier, frequencies of 18.6 Hz, 22.3 Hz, and 50.1 Hz, corresponding to n = 2, were selected as excitation frequencies for the first, second and third injection trials respectively. Based on the relationship between current and force, the amplitude of the external excitation force is estimated to be 5 N. For more details on the relationship between current and force see Appendix C.

Figure 4.23 shows four cases of the total magnetic force acting on the spinning rotor which is calculated in a similar manner as equation (4.7) using the total current and position data collected experimentally with the multimeter and local AMB proximity probes.

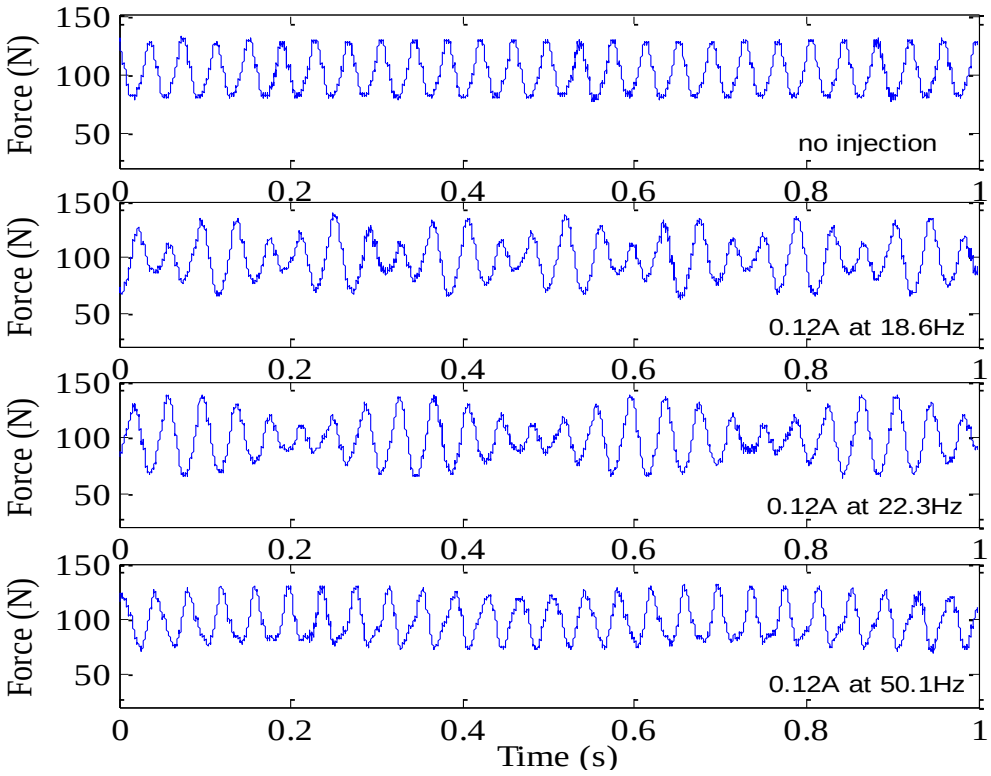

Figure 4.23 Total magnetic force

4.4.1 Healthy Shaft

The first set of experimental trials is presented for the system operating with the healthy shaft. It should be noted that the frequency responses for all experimental trials are plotted on a logarithmic scale in order to better visualize the presence and the amplitudes of the frequency peaks which may not be observable on a linear scale.

Figure 4.24 represents the case of the healthy rotor without and with an external excitation force injection with the response measured at the bearing midspan. The first plot in Figure 4.24 shows the frequency response of the rotating rotor without an external excitation force. The frequency response consists of the rotor spin frequency of 26 Hz, also known as the 1X component, and its harmonics (2X, 3X, 4X, 5X). The 1X component is present in the response of the system due to unbalance existing in the system. The 2X, 3X, 4X, and 5X frequency components are present in the rotor response due to non-linearities caused by imperfections of the experimental system. Such imperfections may include a bow of the shaft, misalignments in the coupling, and some looseness between components of the experimental system. The other three plots in this figure represent the cases with 18.6 Hz, 22.3 Hz and 50.1 Hz frequency injections. Now, each plot shows the frequency response which contains the corresponding injection frequency as well as the rotor spin frequency and its multiples.

Figure 4.25 shows the frequency responses of the healthy rotor without and with an external excitation force injection with responses measured using the sensor positioned next to the non-drive end AMB. The frequency responses for this case are similar to the corresponding frequency responses measured at the bearing midspan with the slight difference in amplitudes of 2X and 4X vibration peaks.

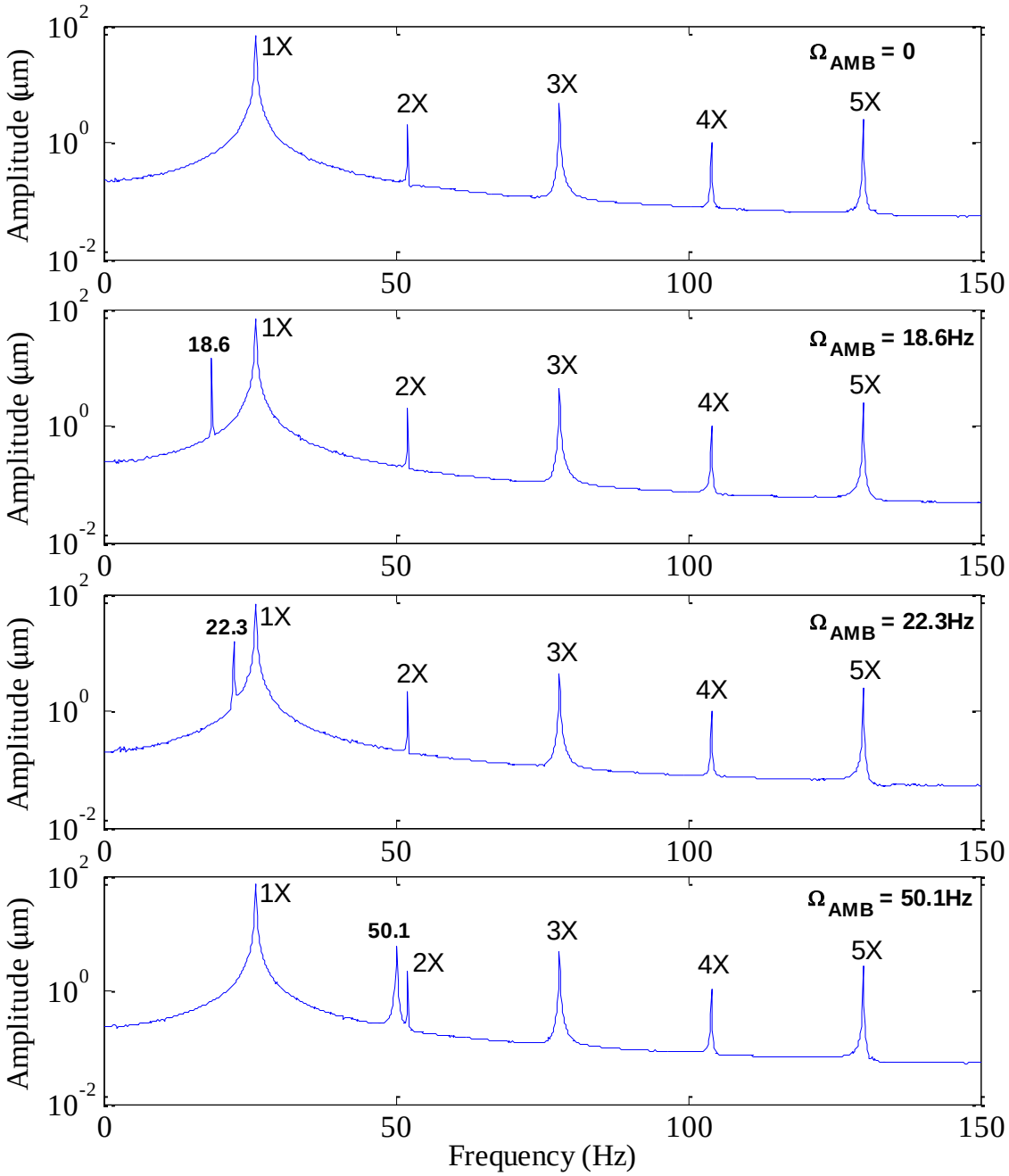

Figure 4.24 Experimental frequency responses of the healthy rotor (rotor spin speed ω = 26 Hz and excitation force of 5 N with various frequencies, response measured at the bearing midspan)

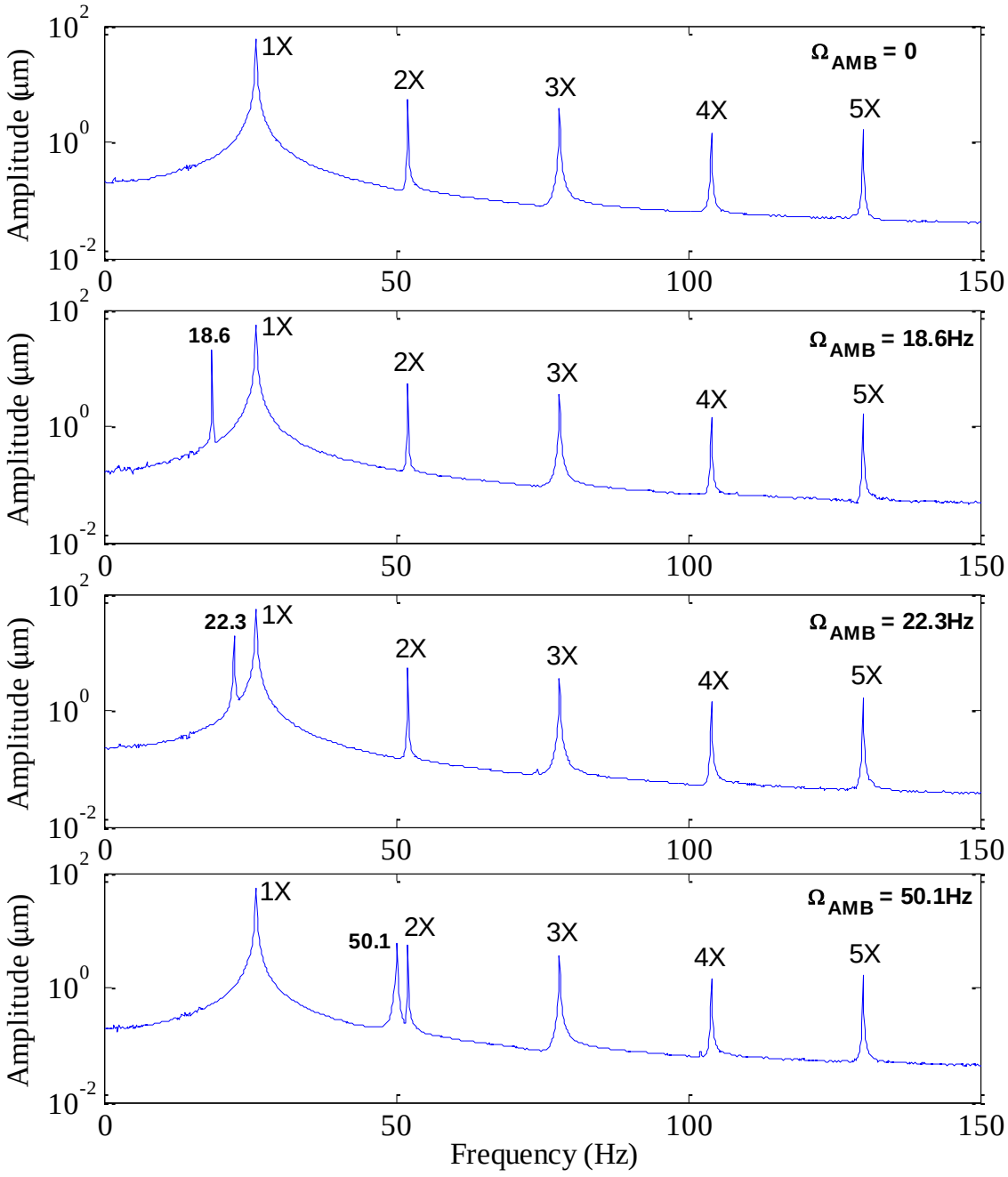

Figure 4.25 Experimental frequency responses of the healthy rotor (rotor spin speed ω = 26 Hz and excitation force of 5 N with various frequencies, response measured next to the non-drive end bearing)

4.4.2 25% Cracked Shaft

The second set of experimental trials is presented for the system operating with the 25% cracked shaft. Figure 4.26 represents the case of the 25% cracked rotor without and with an external excitation force injection with the response measured at the bearing midspan. The first plot in Figure 4.26 shows the frequency response of the rotating rotor without an external excitation force. As in the case with the healthy rotor without an external excitation force, the frequency response of the 25% cracked rotor also consists only of the rotor spin frequency of 26 Hz and its multiples of 2X, 3X, 4X, 5X. The only difference between frequency responses of the healthy and 25% cracked rotors for the case without external AMB excitation is a small increase in the amplitudes of the response peaks. The increase in the response amplitudes of the 25% cracked rotor is insignificant and not applicable for crack detection. The other three plots in this figure correspond to the cases with 18.6 Hz, 22.3 Hz and 50.1 Hz frequency injections. Now, in addition to the injection frequency, rotor spin frequency and multiples of the spin frequency, each plot shows a number of unique combinational frequency peaks due to the presence of the crack, although their amplitudes are insignificant.

Figure 4.26 shows the frequency responses of the 25% cracked rotor without and with an external excitation force injection with responses measured using the sensor positioned next to the non-drive end AMB. The frequency responses for this case are similar to the corresponding frequency responses of the 25% cracked rotor measured at the bearing midspan with the slight difference in quantity of combinational frequency peaks and their amplitudes.

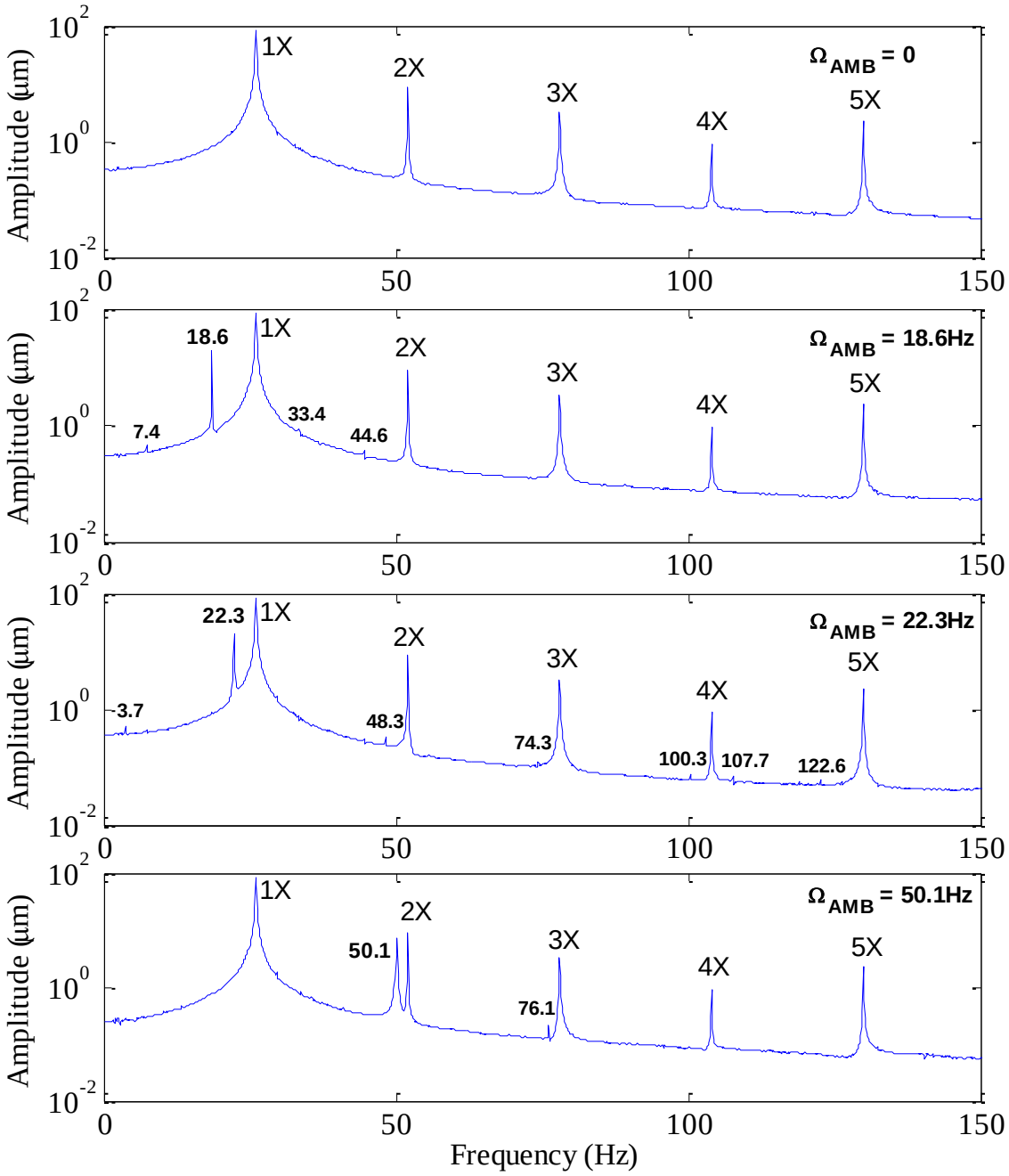

Figure 4.26 Experimental frequency responses of the 25% cracked rotor (rotor spin speed ω = 26 Hz and excitation force of 5 N with various frequencies, response measured at the bearing midspan)

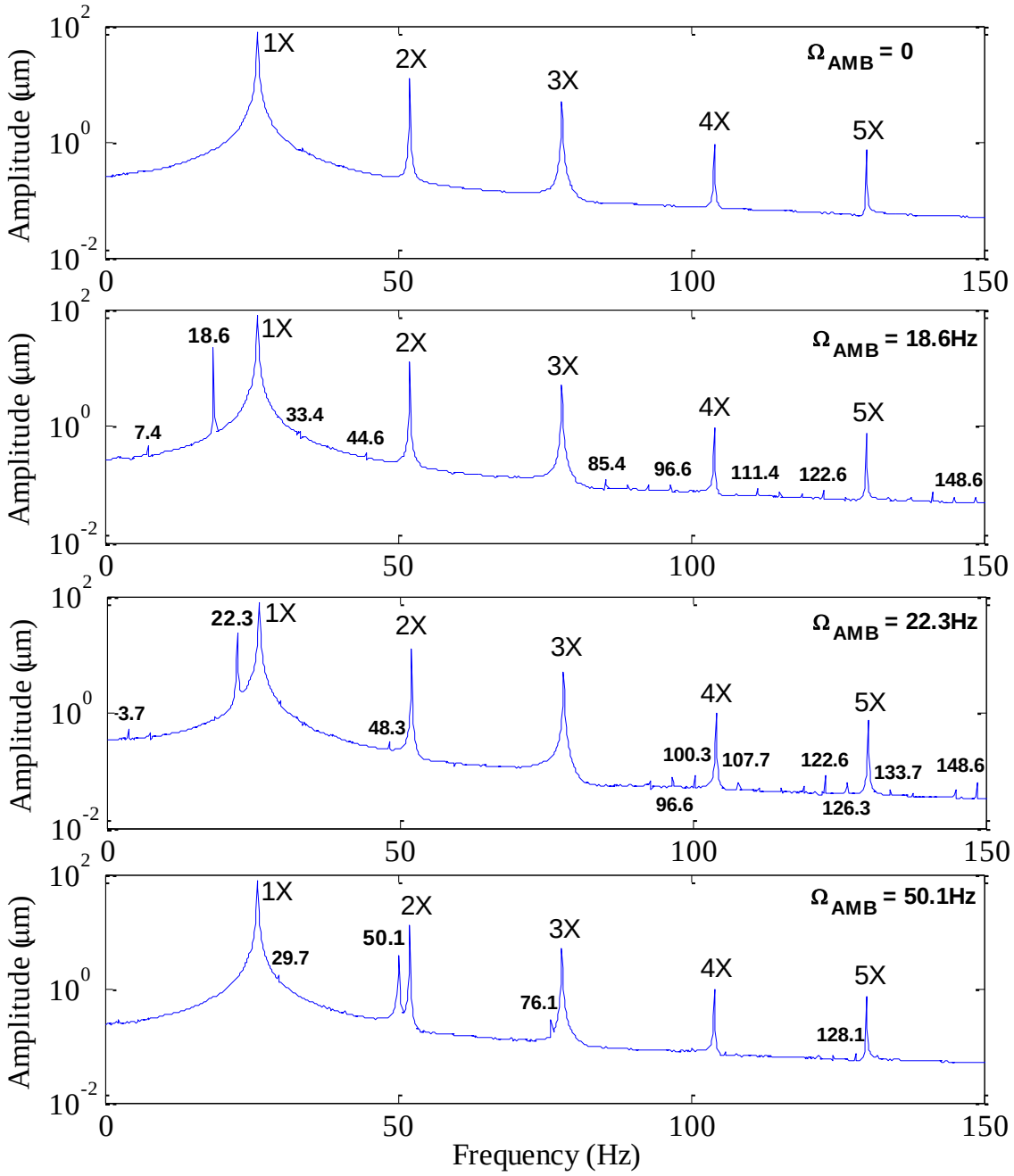

Figure 4.27 Experimental frequency responses of the 25% cracked rotor (rotor spin speed ω = 26 Hz and excitation force of 5 N with various frequencies, response measured next to the non-drive end bearing)

4.4.3 40% Cracked Shaft

The third set of experimental trials is presented for the system operating with the 40% cracked shaft. Figure 4.28 represents the case of the 40% cracked rotor without and with an external excitation force injection with the response measured at the bearing midspan. The first plot in Figure 4.28 shows the frequency response of the spinning rotor without an external excitation force. As in the case with the healthy rotor without an external excitation force, the frequency response of the 40% cracked rotor also consists of the rotor spin frequency of 26 Hz and its multiples of 2X, 3X, 4X, 5X. The only difference between frequency responses of the healthy and 40% cracked rotors for the case without external AMB excitation is a small increase in the amplitudes of the response peaks. The increase in the response amplitudes of the 40% cracked rotor is insignificant and not applicable for crack detection. The other three plots in this figure correspond to the cases with 18.6 Hz, 22.3 Hz and 50.1 Hz frequency injections. Now, in addition to the injection frequency, rotor spin frequency and multiples of the spin frequency, each plot shows a number of unique combinational frequency peaks, emerging due to the presence of the crack. These combinational frequencies provide a unique signature of a crack presence.

Figure 4.29 shows the frequency responses of the 40% cracked rotor without and with an external excitation force injection with responses measured using the sensor positioned next to the non-drive end AMB. The frequency responses for this case are similar to the corresponding frequency responses of the 40% cracked rotor measured at the bearing midspan, although there is a difference in quantity of combinational frequency peaks and their amplitudes. This difference between responses measured with the sensor positioned next to the non-drive end AMB and at the bearing midspan can be

explained by the relative location of the signal injection and a displacement sensor. Because of the geometry and operational speed of the experimental rotor, a higher magnitude response to the injection is seen close to the injection, i.e. using the sensor positioned next to the non-drive end AMB, than is seen farther from the injection, i.e. at the bearing midspan.

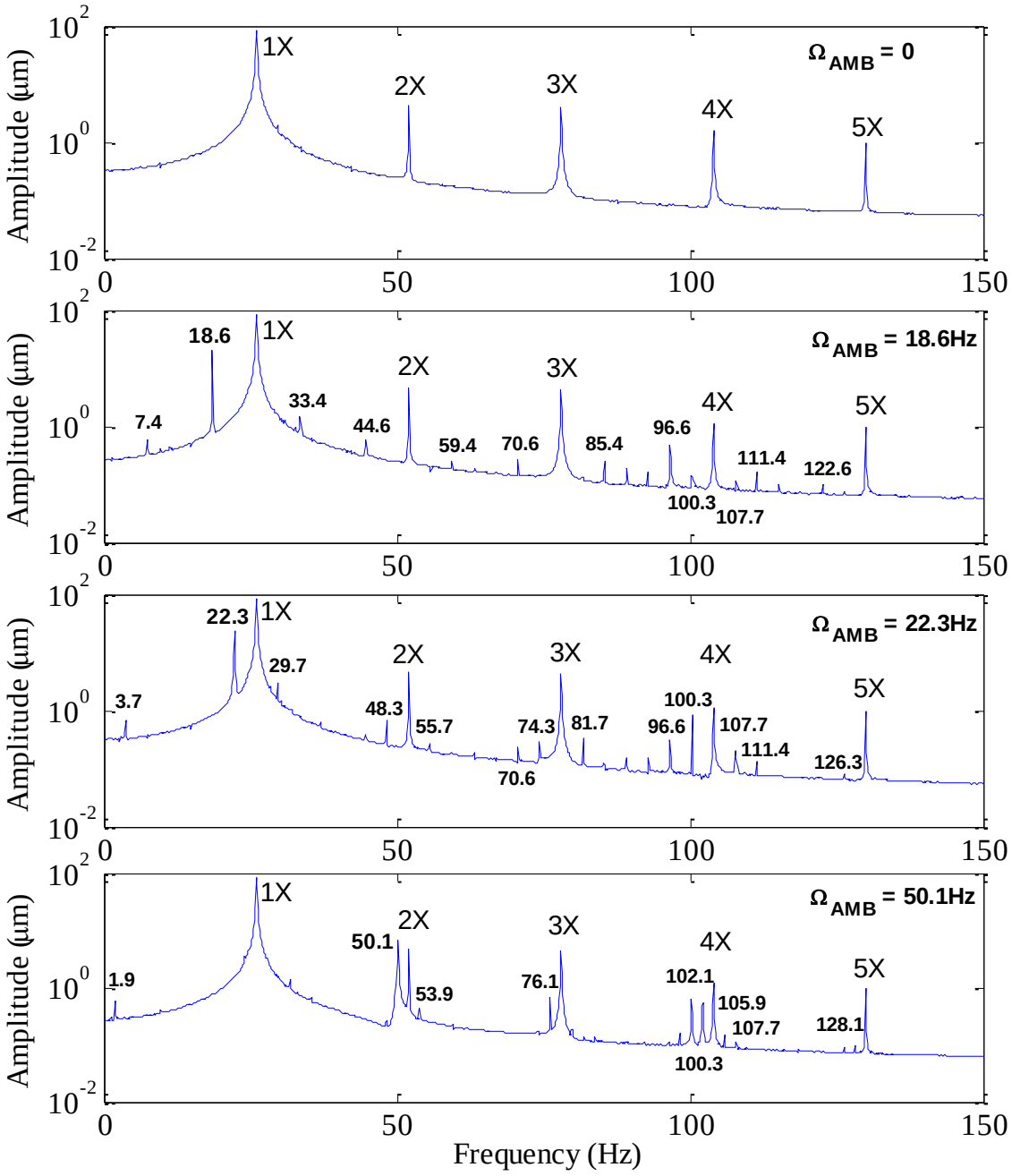

Figure 4.28 Experimental frequency responses of the 40% cracked rotor (rotor spin speed ω = 26 Hz and excitation force of 5 N with various frequencies, response measured at the bearing midspan)

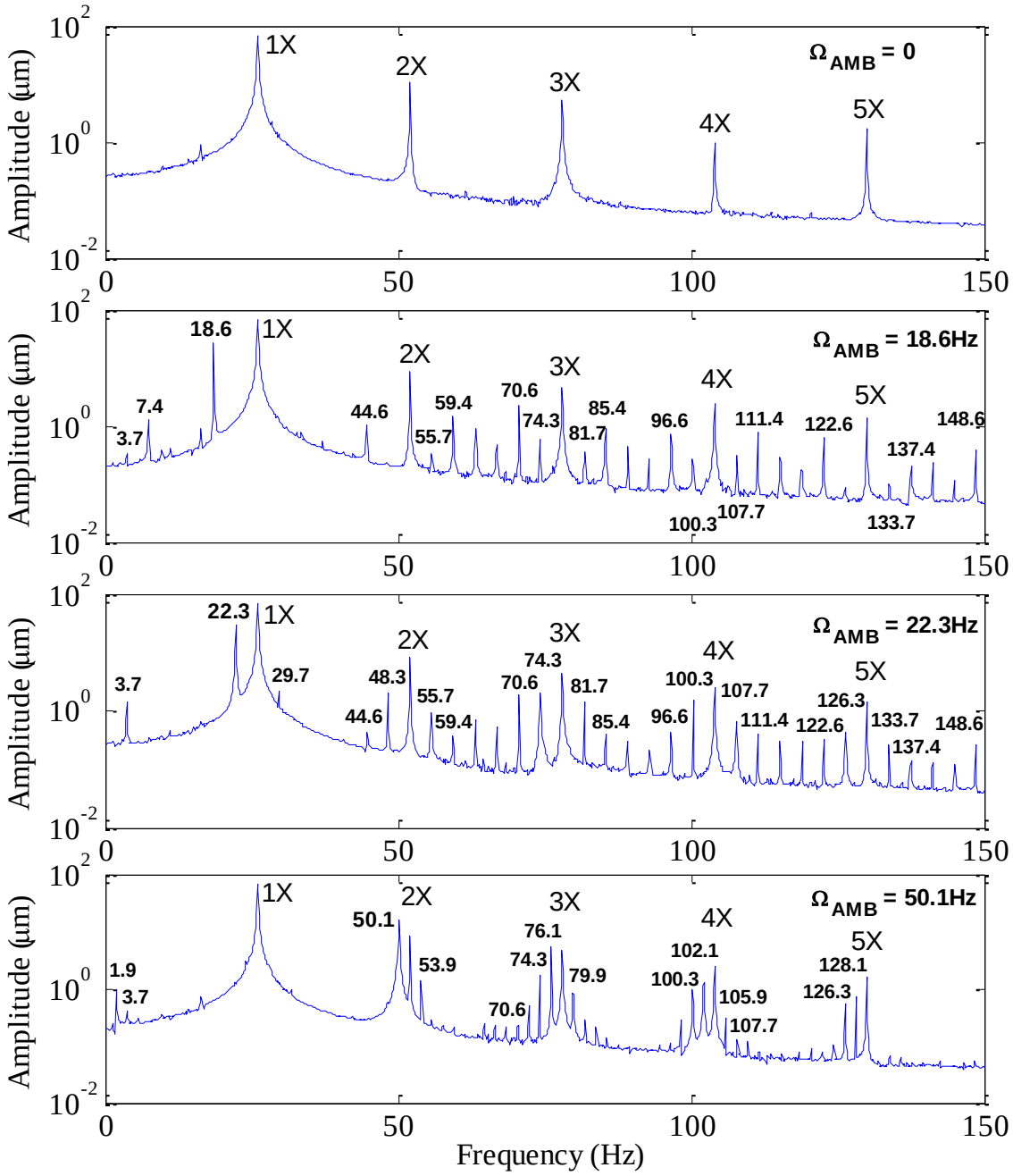

Figure 4.29 Experimental frequency responses of the 40% cracked rotor (rotor spin speed ω = 26 Hz and excitation force of 5 N with various frequencies, response measured next to the non-drive end bearing)

4.4.4 Comparison of Experimental Responses of the Healthy and Cracked Rotors

Figures 4.30 and 4.31 show a comparison of the experimental frequency responses of the healthy and 25% cracked rotors measured using sensors positioned at the bearing midspan and next to the non-drive end AMB respectively. Both figures clearly demonstrate that the frequency responses of the healthy rotor are closely coincide with the corresponding responses of the 25% cracked rotor when the external excitation force is not applied, which makes the detection of a crack not possible. For the cases when the external excitation is applied, each frequency response of the 25% cracked rotor contains a number of unique combinational frequency peaks, which are not present in the response of the healthy counterpart, although their amplitudes are negligible that makes the 25% diameter crack tough to detect.

Figures 4.32 and 4.33 show a comparison of the experimental frequency responses of the healthy and 40% cracked rotors measured using sensors positioned at the bearing midspan and next to the non-drive end AMB respectively. As in the case of comparison of the healthy and 25% cracked rotors, both figures clearly demonstrate that the frequency responses of the healthy rotor are closely coincide with the corresponding responses of the 40% cracked rotor when the external excitation force is not applied. For the cases when the external excitation is applied, each frequency response of the 40% cracked rotor contains a number of unique combinational frequency peaks, which are not present in the response of the healthy counterpart. There is an apparent difference between frequency responses of the healthy and 40% cracked rotors, which provides a clear evidence of a crack presence.

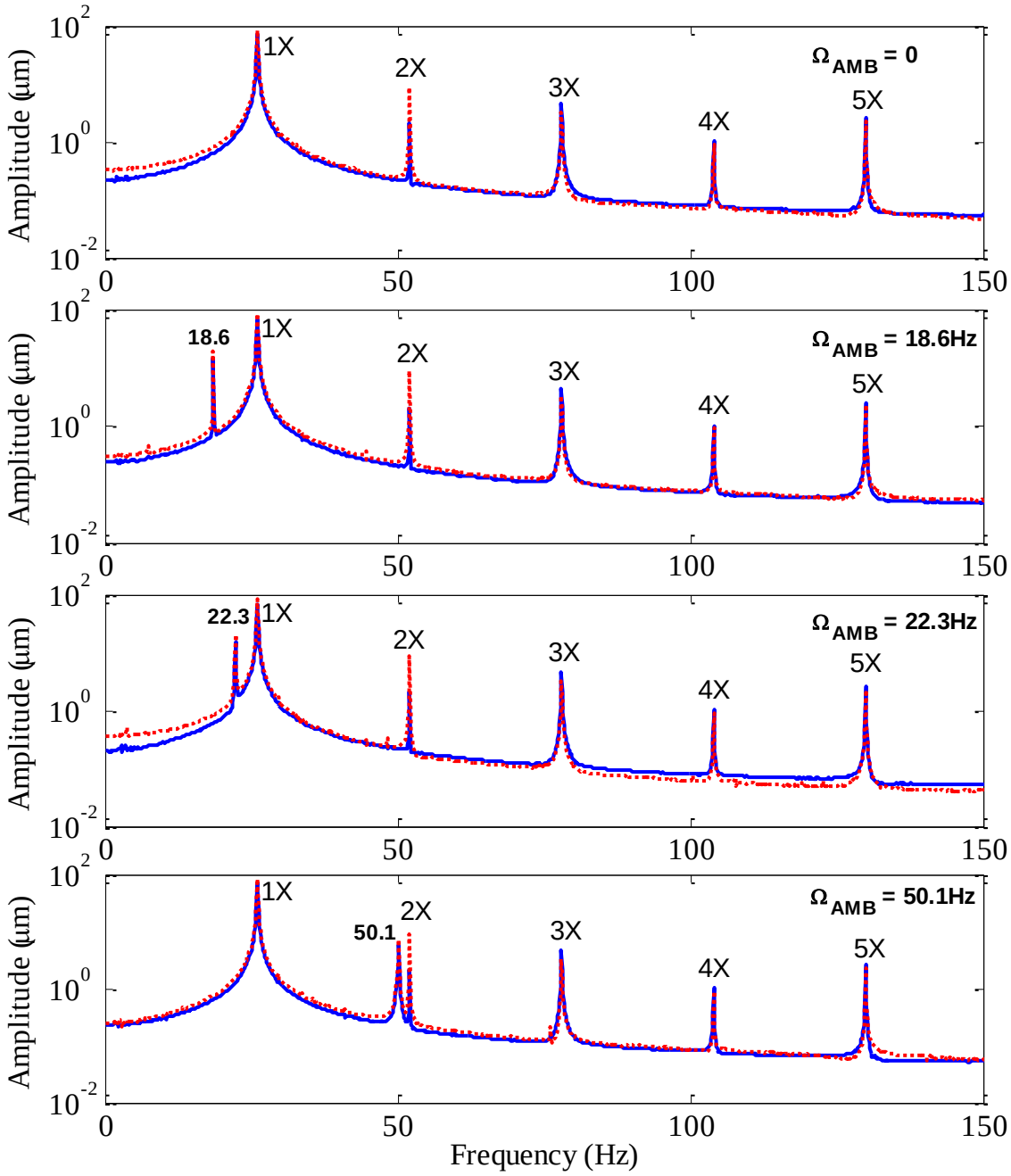

Figure 4.30 Comparison between experimental frequency responses of the healthy (solid line) and 25% cracked (dotted line) rotors (rotor spin speed ω = 26 Hz and excitation force of 5 N with various frequencies, response measured at the bearing midspan)

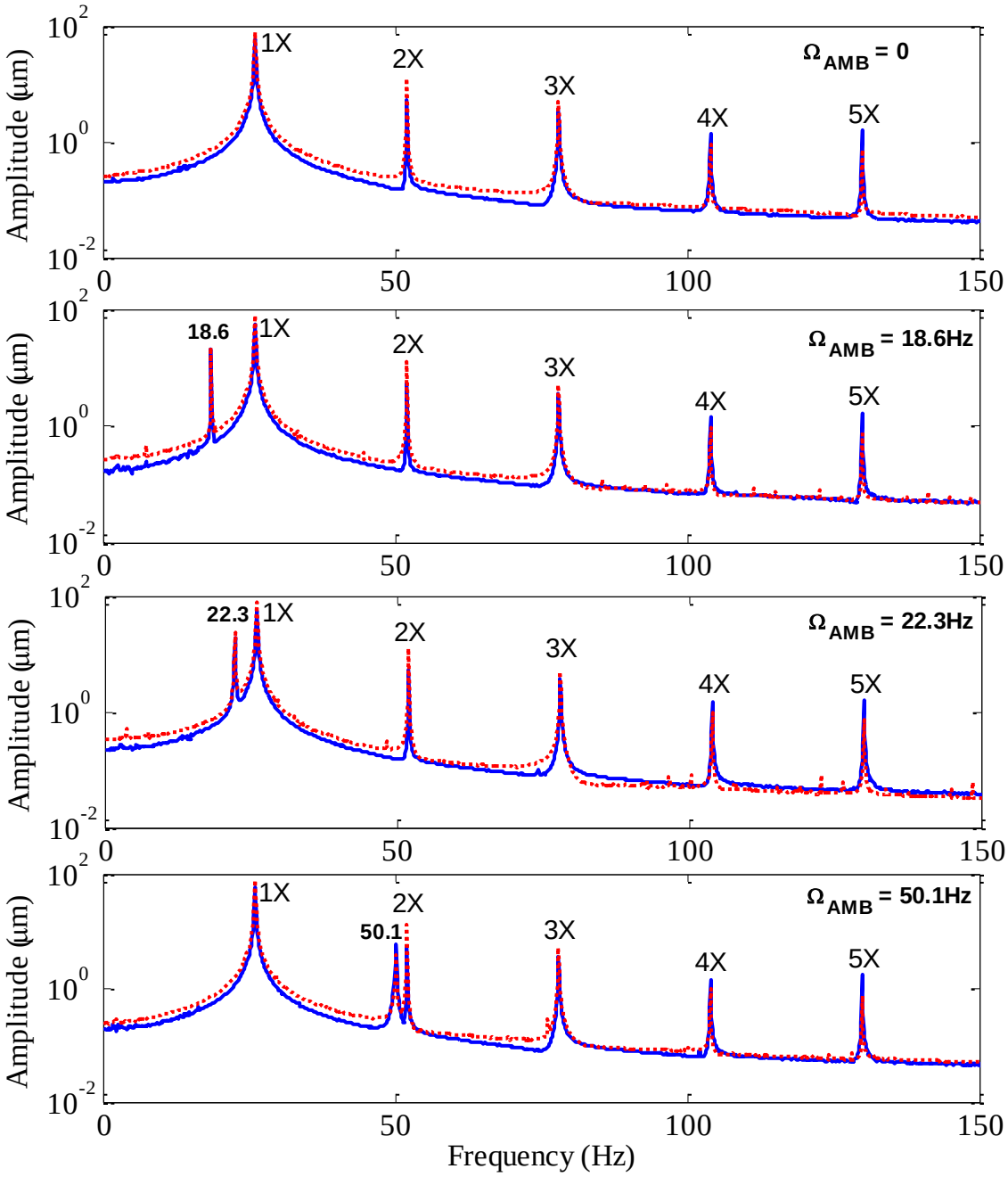

Figure 4.31 Comparison between experimental frequency responses of the healthy (solid line) and 25% cracked (dotted line) rotors (rotor spin speed ω = 26 Hz and excitation force of 5 N with various frequencies, response measured next to the non-drive end bearing)

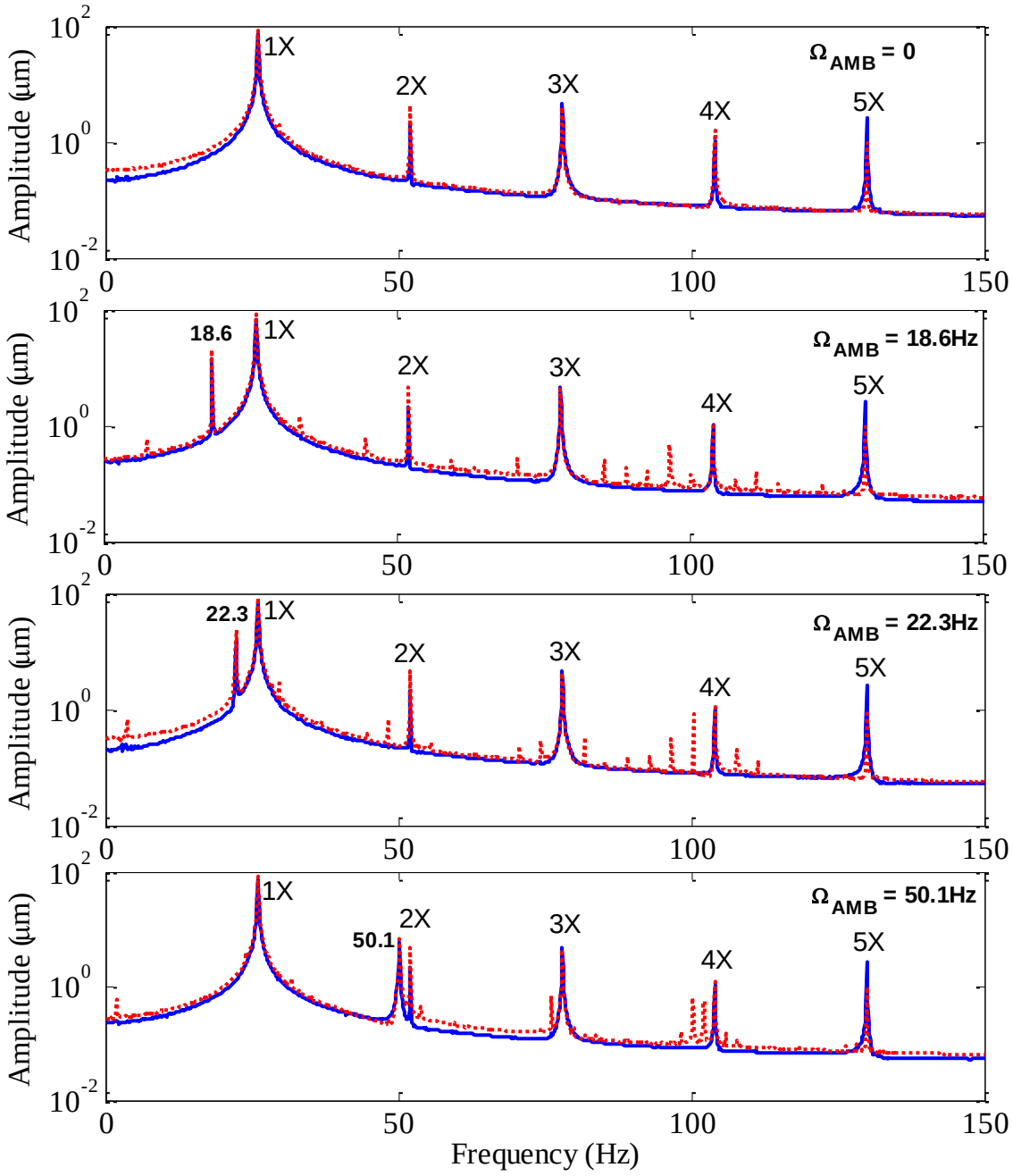

Figure 4.32 Comparison between experimental frequency responses of the healthy (solid line) and 40% cracked (dotted line) rotors (rotor spin speed ω = 26 Hz and excitation force of 5 N with various frequencies, response measured at the bearing midspan)

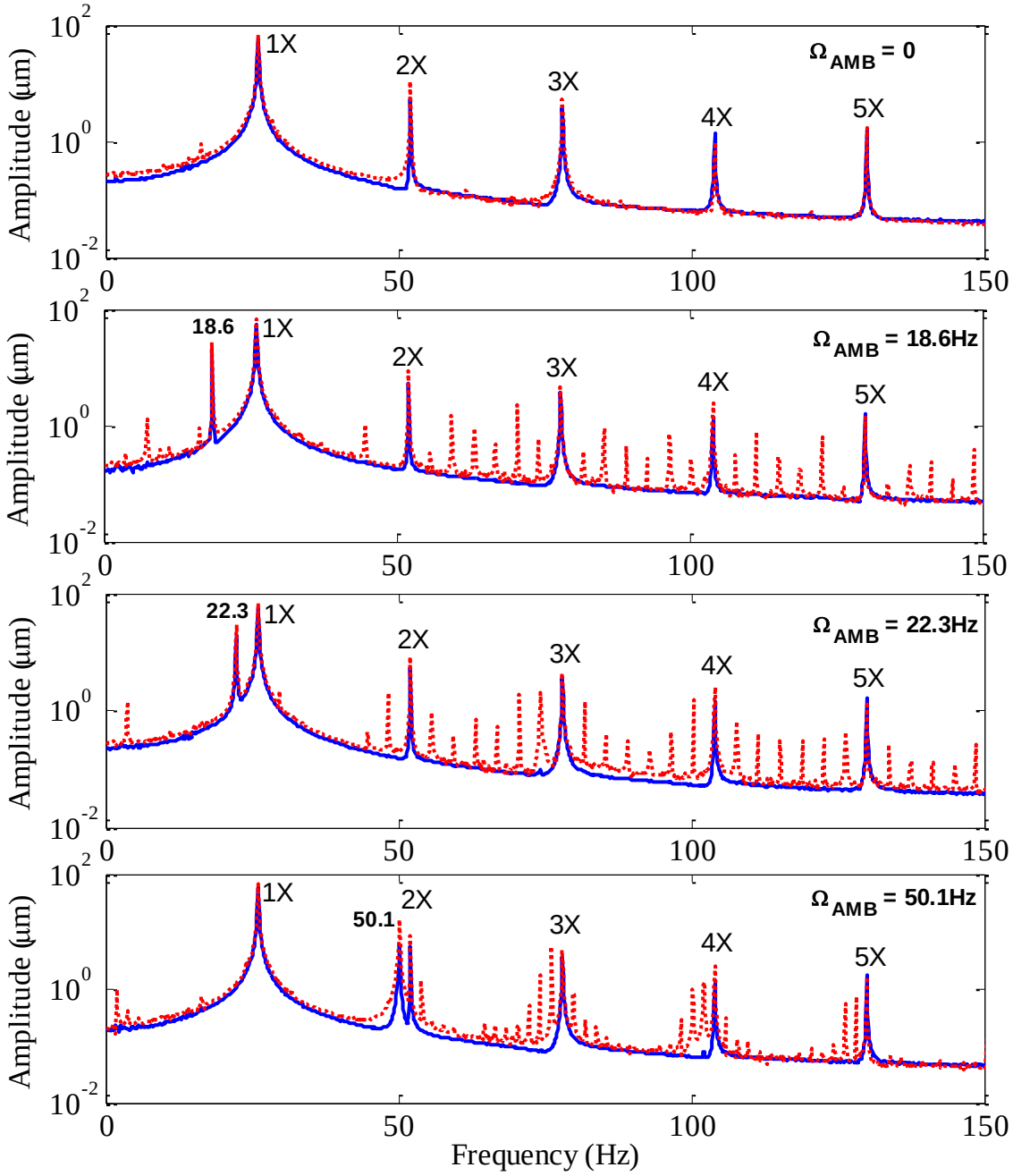

Figure 4.33 Comparison between experimental frequency responses of the healthy (solid line) and 40% cracked (dotted line) rotors (rotor spin speed ω = 26 Hz and excitation force of 5 N with various frequencies, response measured next to the non-drive end bearing)

Figure 4.34 shows the experimental vibration signals of the levitated healthy and 40% cracked rotors running at the speed of 1560 rpm without (a, b) and with (c, d) an external excitation force of 5 N applied at 18.6 Hz at the V-axis of the non-drive end bearing. For all cases, responses were measured with a position sensor located next to the non-drive end AMB and oriented along V-axis. The responses are similar, although there is an increase in the response amplitudes of the 40% cracked rotor. The increase in the response amplitudes, which is about 10-15 μm, may be applicable for crack detection.

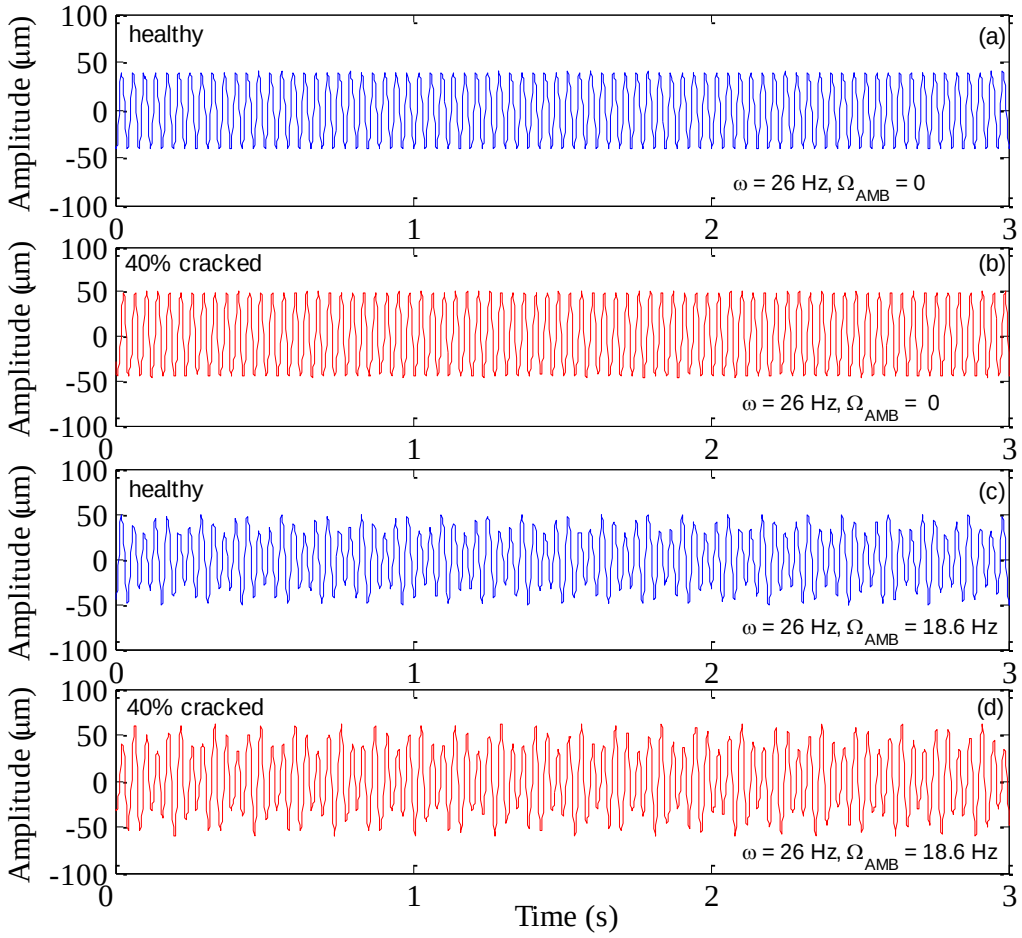

Figure 4.34 Experimental time responses of the healthy and 40% cracked rotors at spin speed ω = 26 Hz: (a, b) without and (c, d) with an additional harmonic force of 5 N at 18.6 Hz applied at the V-axis of the non-drive end bearing

Figure 4.35 shows the experimental vibration signals of the levitated healthy and 40% cracked rotors running at the speed of 1560 rpm with an external excitation force of 5 N applied at 22.3 Hz (a, b) and 50.1 Hz (c, d) at the V-axis of the non-drive end bearing. For all cases, responses were measured with a position sensor located next to the non-drive end AMB and oriented along V-axis. As in the previous cases with no injection and with 18.6 Hz force injection, the vibration responses of the healthy and 40% cracked rotors with 22.3 Hz and 50.1 Hz force injections are similar, although there is an increase in the response amplitudes of the 40% cracked rotor. The increase in the response amplitudes, which is about 15-20 µm, may be applicable for crack detection.

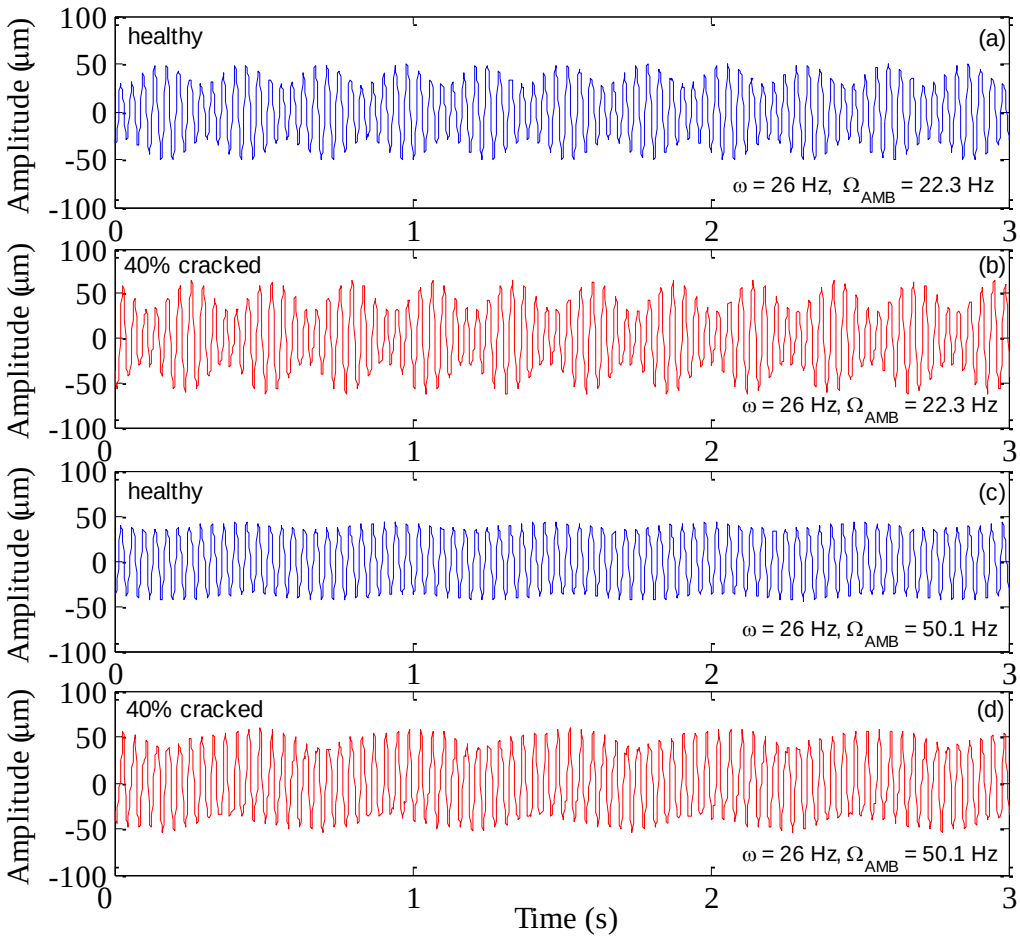

Figure 4.35 Experimental time responses of the healthy and 40% cracked rotors at spin speed ω = 26 Hz: with an additional harmonic force of 5 N applied at 22.3 Hz (a, b) and 50.1 Hz (c, d) at the V-axis of the non-drive end bearing

Figures 4.36 and 4.37 show the frequency responses of the healthy and 40% cracked rotors at the vicinity of combinational frequencies of 70.6 Hz and 111.4 Hz, respectively, for a case without (a) and with (b) external excitation force of 5 N at 18.6 Hz injection frequency. The magnification of the 40% cracked rotor response due to external excitation force is apparent.

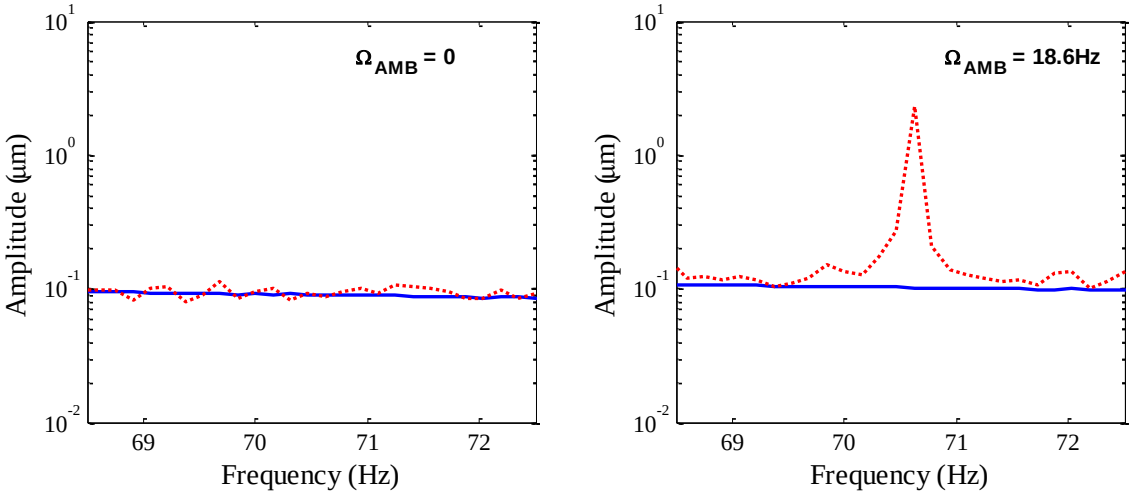

(a) **(b)**

Figure 4.36 Experimental frequency responses of the healthy (solid line) and 40% cracked (dotted line) rotors at spin speed ω = 26 Hz: (a) without and (b) with excitation force of 5 N near the combinational frequency 70.6 Hz

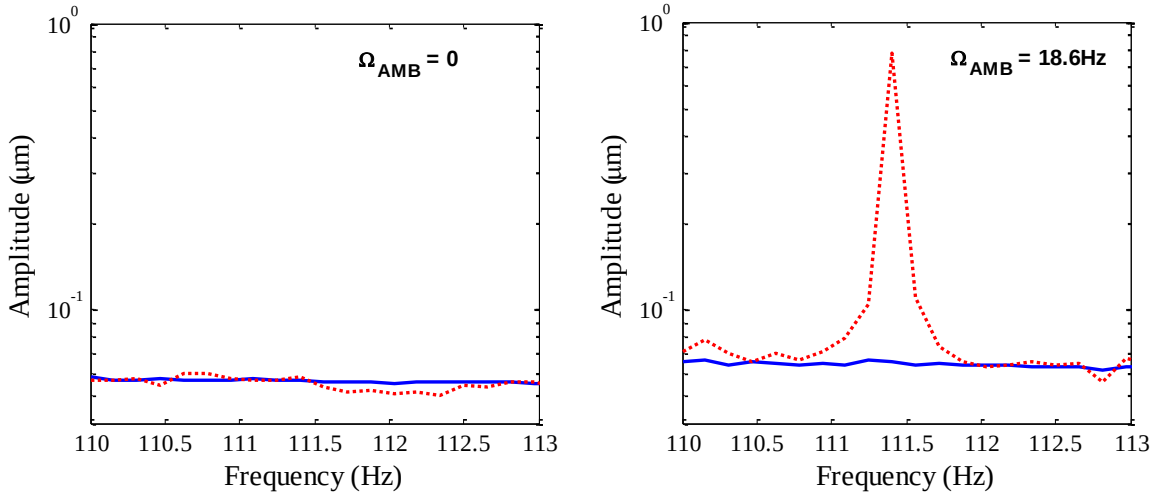

(a) **(b)**

Figure 4.37 Experimental frequency responses of the healthy (solid line) and 40% cracked (dotted line) rotors at spin speed ω = 26 Hz: (a) without and (b) with excitation force of 5 N near the combinational frequency 111.4 Hz

Figure 4.38 shows the experimental frequency responses of the healthy and 40% cracked rotors measured with an accelerometer, installed on top of the non-drive end bearing housing. The response of the healthy rotor consists of the rotor spin frequency of 26 Hz (1X) and its harmonics (2X, 3X, 4X). Also, a few combinational frequency peaks appear at 1.9 Hz, 24.1 Hz and 27.9 Hz, although their amplitudes are negligible. The response of the 40% cracked rotor contains some combinational frequencies as well as the rotor spin frequency and its multiples. Overall, the response amplitude of the 40% cracked rotor is higher than the amplitude of the healthy rotor. The significant differences are visible at the induced combinational frequencies. Although the accelerometer data presented results analogous to the eddy-current probes, the accelerometer was found to be more effective for a system with higher operational speeds.

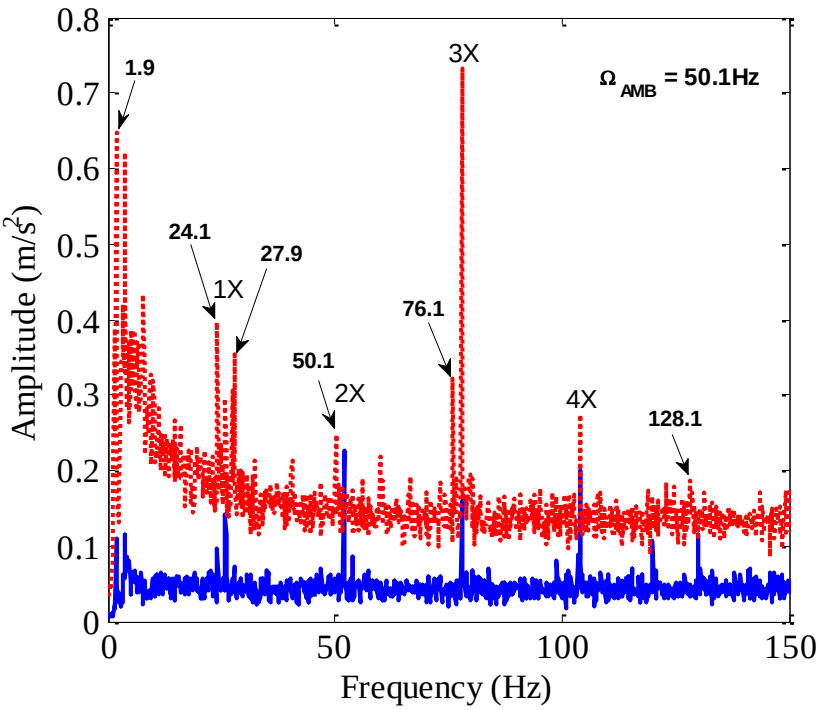

Figure 4.38 Experimental responses of the healthy (solid line) and 40% cracked (dotted line) rotors measured with an accelerometer (rotor spin speed ω = 26 Hz with excitation force of 5 N at 50.1 Hz)

4.4.5 Comparison of Simulated and Experimental Responses

A comparison of the simulated and experimental frequency responses of the healthy, 25% cracked and 40% cracked rotors is shown in Figure 4.39, Figure 4.40 and Figure 4.41 respectively. It should be noted that the results are plotted on a logarithmic scale in order to better visualize the presence and the amplitudes of the frequency peaks which may not be observable on a linear scale. The combinational frequencies that were predicted by the simulation can be seen in the experimental data. The difference in the noise floor between the simulation and experimental data can be attributed to the optimal time step selection in the simulation which is ideal and has no noise or extra frequency inputs. The other factors which occur in a real system in conjunction with the practical time step raise the noise floor. The difference in peak amplitudes can be attributed to the small mistuning of the unbalance, injection magnitude, and stiffness and damping of the system.

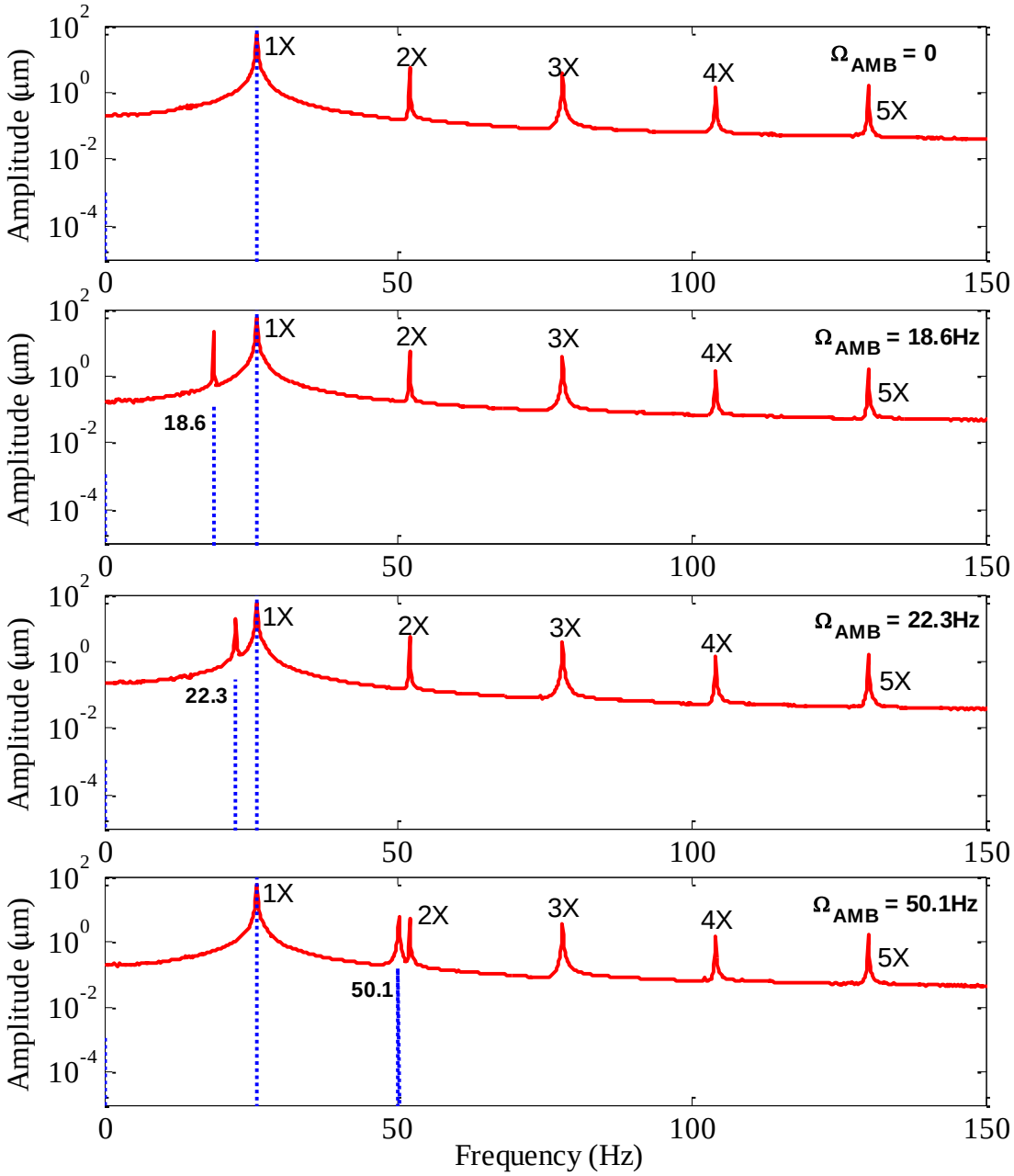

Figure 4.39 Comparison between simulated (dotted line) and experimental (solid line) frequency responses of the healthy rotor (rotor spin speed ω = 26 Hz and excitation force of 5 N with various frequencies, response measured next to the non-drive end bearing)

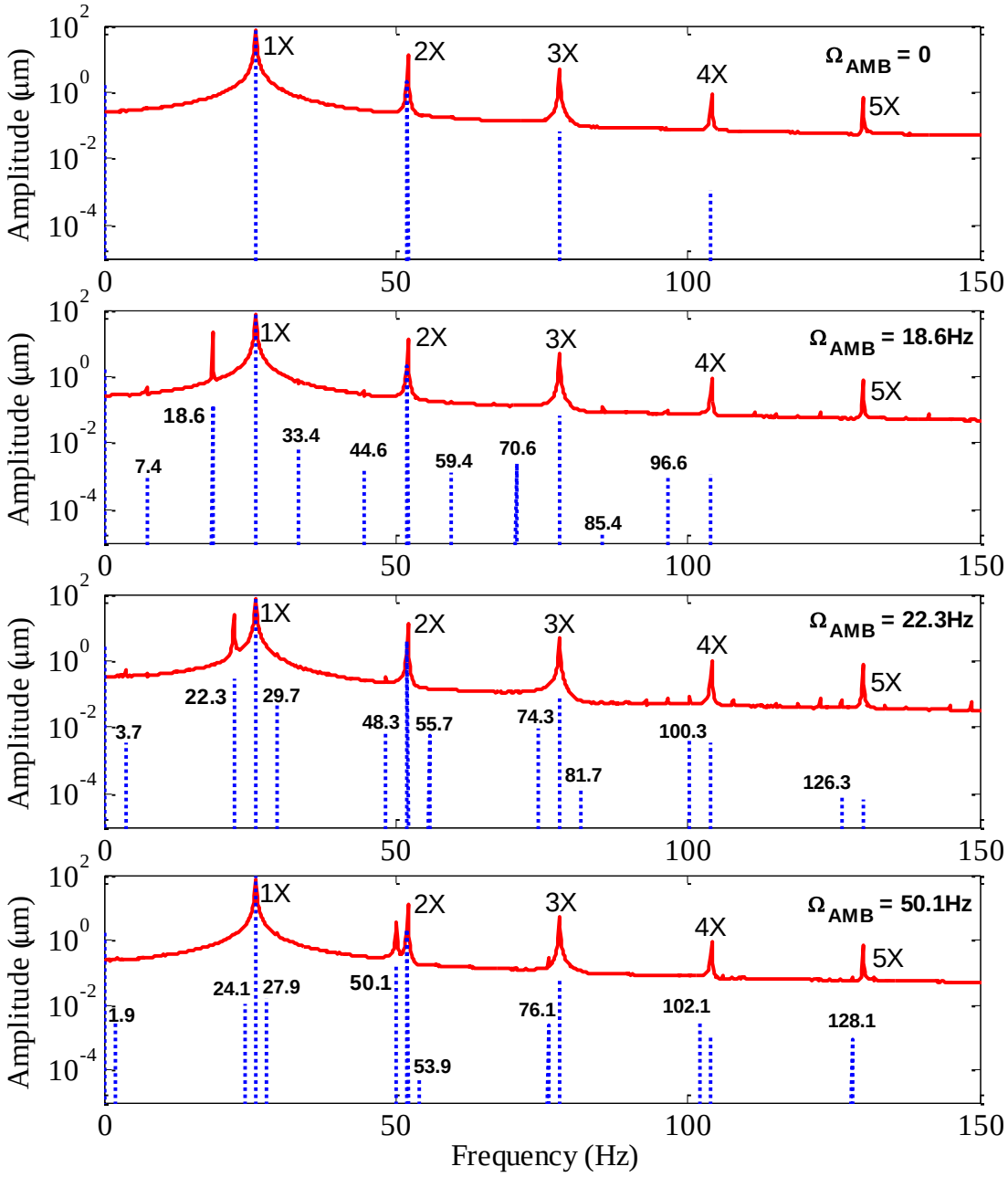

Figure 4.40 Comparison between simulated (dotted line) and experimental (solid line) frequency responses of the 25% cracked rotor (rotor spin speed ω = 26 Hz and excitation force of 5 N with various frequencies, response measured next to the non-drive end bearing)

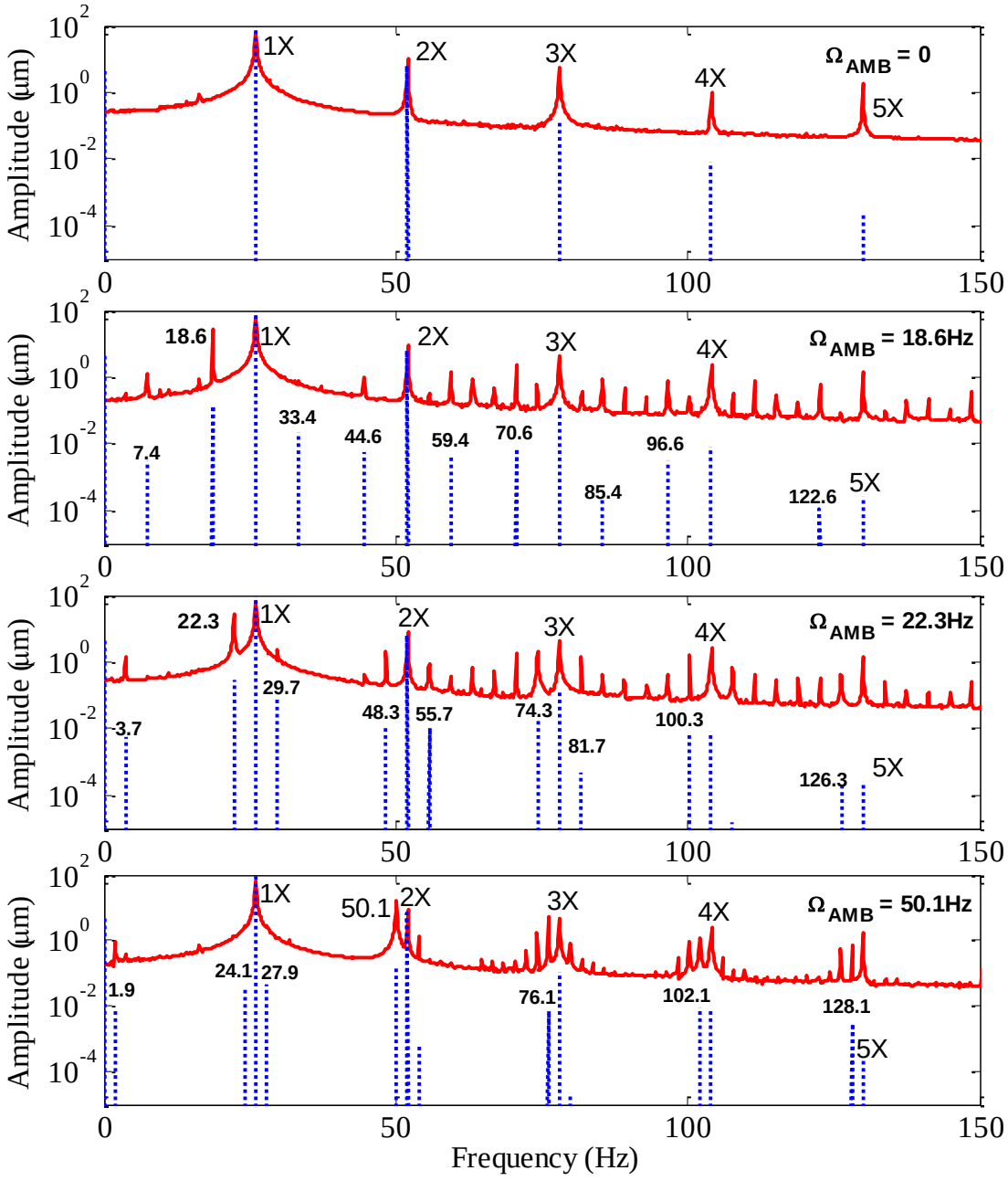

Figure 4.41 Comparison between simulated (dotted line) and experimental (solid line) frequency responses of the 40% cracked rotor (rotor spin speed ω = 26 Hz and excitation force of 5 N with various frequencies, response measured next to the non-drive end bearing)

CHAPTER V

CONCLUSIONS

Detection and monitoring of fatigue cracks in the rotating machinery has been an interesting area of scientific study in the past three decades. Particularly, the dynamic characteristics of cracked shafts and their monitoring have received the most attention in this area of research.

This thesis has investigated an innovative approach to the on-line health monitoring of rotating machinery in the presence of structural damage using active magnetic bearings. In particular, a method for on-line detection of the transverse surface crack in AMB-supported shafts during operation has been explored. In addition to pure levitation, the rotor supporting bearing also served as a force actuator that transformed current signals additionally injected inside the control loop with a specially pre-calculated frequency into the superimposed forces which perturbed the suspended spinning rotor. In order to calculate the external excitation frequencies, the first two natural frequencies of the rotor-

bearing system that correspond to rigid body modes and the third frequency associated with the first bending mode were utilized.

An extensive amount of the experimental data for the healthy, 25% cracked and 40% cracked rotors with different force injections has been collected, analyzed and presented. The obtained results clearly demonstrate that the external excitation force with a specially pre-calculated frequency when applied on the levitated spinning cracked rotor induces combinational frequencies corresponding to the injected AMB frequency, the rotor spin speed and natural frequencies of the system. These combinational frequencies provide a unique signature of the presence of a crack. When the experimental results were compared, it was observed that the amplitudes of the combinational frequencies amplify when the crack depth increases. Moreover, the quantity and the amplitude of the combinational frequency peaks depend on the location of the force injection and position of the displacement sensor.

In addition, the modeling and control of the system with conical active magnetic bearings has been presented in detail. The forces generated by a system of two conical AMBs have been derived and then implemented in MATLAB/Simulink software in order to simulate the behavior of the experimental rotor magnetically supported using two conical AMBs and confirm the stability and robustness of the experimental rotor-bearing system. It has been shown that computer simulations agree well with the experimentally extracted data indicating that the method of modeling a system with conical AMBs, described in this thesis, is accurate to reproduce the experimental behavior of the shaft magnetically levitated using conical AMBs.

The inherent abilities for sensing, information processing and actuation give the magnetic bearing the potential to become a key element in smart machines. The existing AMB and its sensors can be utilized for on-line structural damage detection. This would be the step toward smart rotating machinery where no additional hardware is required for diagnostic purposes. This technology enables rotating machinery to become smart or have self-diagnosing features.

BIBLIOGRAPHY

[Aenis, 2002**]** Aenis, M., Knopf, E., Nordmann, R., "Active Magnetic Bearing for the Identification and Fault Diagnosis in Turbomachinery," *Mechatronics*, Vol. 12, pp. 1011-1021, 2002

[Bash, 2005] Bash, T. J., "Active Magnetic Bearings used as an Actuator for Rotor Health Monitoring in Conjunction with Conventional Support Bearings," Thesis, Virginia Polytechnic Institute and State University, Blacksburg, VA, USA, 2005

[Dimarogonas, 1996] Dimarogonas, A. D., "Vibration of Cracked Structures: A State of the Art Review," *Engineering Fracture Mechanics*, Vol. 55, No. 5, pp. 831-857, 1996

[Fukata, 1992] Fukata, S., Kouya, Y., "Dynamics of Active Magnetic Bearings with Magnet Cores in the Shape of a Cone," *Proceedings of the 3rd International Symposium on Magnetic Bearings*, Alexandria, Virginia, USA, pp. 339-348, 1992

[Gasch, 1976] Gasch, R., "Dynamic Behaviour of a Simple Rotor with a Cross-Sectional Crack," *International Conference on Vibrations in Rotating Machinery*, IMechE, Paper C178/76, pp. 123-128, 1976

[Gasch, 1993] Gasch, R., "A Survey of the Dynamic Behaviour of a Simple Rotating Shaft with a Transverse Crack," *Journal of Sound and Vibration*, Vol. 160(2), pp. 313-332, 1993

[Ishida, 2006] Ishida, Y., Inoue, T., "Detection of a Rotor Crack using a Harmonic Excitation and Nonlinear Vibration Analysis," *Journal of Vibration and Acoustics*, Vol. 128(6), pp. 741-749, 2006

[Jing, 2002] Jing, Y., Peng, G., Lie, Y., "Dynamic Properties Investigation about Conical AMB," *Proceedings of the 8th International Symposium on Magnetic Bearings*, Mito, Japan, pp. 349-353, August 26-28, 2002

[Jun, 1992] Jun, O. S., Eun, H. J., Earmme, Y. Y., Lee, C. -W., "Modeling and Vibration Analysis of a Simple Rotor with a Breathing Crack," *Journal of Sound and Vibration*, Vol. 155(2), pp. 273-290, 1992

[Lee, 2000] Lee, Y. –S., Chung, M. –J., "A Study on Crack Detection using Eigenfrequency Test Data," *Computers and Structures*, Vol. 77, pp. 327-342, 2000

[Mani, 2005] Mani, G., Quinn, D. D., Kasarda, M. E. F., Inman, D. J., and Kirk, R. G., " Health Monitoring of Rotating Machinery Through External Forcing," *Proceedings of ISCORMA-3*, Cleveland, Ohio, USA, 19-23 September 2005

[Mani, 2006] Mani, G., Quinn, D. D., Kasarda, M. E. F., "Active Health Monitoring in a Rotating Cracked Shaft Using Active Magnetic Bearings as Force Actuators," *Journal of Sound and Vibration*, Vol. 294, pp. 454-465, 2006

[Maslen, 2008] Maslen, E. H., "Smart Machine Advances in Rotating Machinery," *9th International Conference on Vibrations in Rotating Machinery*, IMechE, Exeter, UK, September 8-10, 2008

[Mayes, 1976] Mayes, I. W., Davies, W. G. R., "The Vibrational Behaviour of a Rotating Shaft System Containing a Transverse Crack," *International Conference on Vibrations in Rotating Machinery*, IMechE, Paper C168/76, pp. 53-64, 1976

[Mayes, 1980] Mayes, I. W., Davies, W. G. R., "A Method of Calculating the Vibrational Behaviour of a Coupled Rotating Shafts Containing a Transverse Crack," *International Conference on Vibrations in Rotating Machinery*, IMechE, Paper C254/80, pp. 17-27, 1980

[Mohamed, 1992] Mohamed, A. M., Fawzi, P. E., "Conical Magnetic Bearings with Radial and Thrust Control," *IEEE Transactions on Automatic Control*, Vol. 37(12), pp. 1859-1868, December 1992

[Nordmann, 2001] Nordmann, R. et al. "Improved Machinery Performance Using Active Control Technology (IMPACT)," Final Report, BRITE/EURAM Project, April 2001

[Nordmann, 2004] Nordmann, R., Aenis, M., "Fault Diagnosis in a Centrifugal Pump Using Active Magnetic Bearings," *International Journal of Rotating Machinery,* Vol. 10(3), pp. 183-191, 2004

[Papadopoulos, 1987] Papadopoulos, C. A., Dimarogonas, A. D., "Coupled Longitudinal and Bending Vibrations of a Rotating Shaft with an Open Crack," *Journal of Sound and Vibration,* Vol. 117(1), pp. 81-93, 1987

[Quinn, 2005] Quinn, D. D., Mani, G., Kasarda, M. E. F., Bash, T., Inman, D. J., Kirk, R. G., " Damage Detection of a Rotating Cracked Shaft Using an Active Magnetic Bearing as a Force Actuator—Analysis and Experimental Verification," *IEEE/ASME Transactions on Mechatronics,* Vol. 10, No. 6, pp. 640-647, 2005

[Sawicki, 2003] Sawicki, J. T., Bently, D. E., Wu, X., Baaklini, G. Y., Friswell, M. I., "Dynamic Behavior of Cracked Flexible Rotor Subjected to Constant Driving Torque," *Proceedings of the 2nd International Symposium on Stability Control of Rotating Machinery,* Gdansk, Poland, pp. 231-241, 2003

[Sawicki, 2008] Sawicki, J. T., Friswell, M. I., Pesch, A. H., Wroblewski, A. C., "Condition Monitoring of Rotor Using Active Magnetic Actuator," *Proceedings of ASME Turbo Expo 2008: Power for Land, Sea and Air,* Berlin, Germany, June 9-13, 2008

[Sawicki, 2009] Sawicki, J. T., Lekki, J. D., "Smart Rotating Machinery for Structural Health Monitoring," *The 7th International Workshop on Structural Health Monitoring*, Stanford University, Stanford, California, September 9-11, 2009

[Sawicki, 2003] Sawicki, J. T., Wu, X., Baaklini, G. Y., Gyekenyesi, A. L., "Vibration-Based Crack Diagnosis in Rotating Shafts During Acceleration through Resonance," *Proceedings of SPIE 10th Annual International Symposium on Smart Structures and Materials*, San Diego, California, 2003

[Schweitzer, 2005] Schweitzer, G., "Safety and Reliability Aspects for Active Magnetic Bearing Applications – A Survey," *Proc. of the Institution of Mechanical Engineers Part I – Journal of Systems and Control Engineering*, IMechE, Vol. 219(6), pp. 383-392, 2005

[Schweitzer, 1993] Schweitzer, G., Bleuler, H., and Traxler, A., "Active Magnetic Bearings," Verlag der Fachvereine, Zurich, Switzerland, 1993

[Sinou, 2008] Sinou, J. –J., "Detection of Cracks in Rotor Based on the 2x and 3x super-harmonic frequency components and the crack-unbalance interactions," *Communications in Nonlinear Science and Numerical Simulation*, Vol. 13, pp.2024-2040, 2008

[Wauer, 1990] Wauer, J., "On the Dynamics of Cracked Rotors: A Literature Survey," *Applied Mechanics Reviews*, Vol. 43(1), pp. 13-17, 1990

[Wroblewski, 2008] Wroblewski, A. C., "Health Monitoring of Cracked Rotor Systems Using External Excitation Techniques," Thesis, Cleveland State University, Cleveland, Ohio, USA, 2008

[Xiang, 2008] Xiang, J., Zhong, Y., Chen, X., He, Z., "Crack Detection in a Shaft by Combination of Wavelet-Based Elements and Generic Algorithm," *International Journal of Solids and Structures*, Vol. 45, pp. 4782-4795, 2008

[Zhou, 2005] Zhou, T., Sun, Z., Xu, J., Han, W., "Experimental Analysis of Cracked Rotor," *Journal of Dynamic Systems, Measurement, and Control*, Vol. 127(3), pp. 313-320, 2005

[Zhu, 2002] Zhu, C., Robb, D. A., Ewins, D. J., "The Dynamics of a Cracked Rotor with an Active Magnetic Bearing," *Journal of Sound and Vibration*, Vol. 265, pp. 469-487, 2002

APPENDICES

APPENDIX A

Finite Element Model of the Rotor

Table A-I Finite element model of the rotor

Node #	Node Location m	OD Left m	ID Left m	OD Right m	ID Right m	Comments
1	0	0.0159	0	0.0159	0	
2	0.0133	0.0159	0	0.0159	0	
3	0.0266	0.0159	0	0.0159	0	
4	0.0393	0.0159	0	0.0159	0	
5	0.052	0.0159	0	0.0159	0	
6	0.0774	0.0159	0	0.0159	0	
7	0.0868	0.0159	0	0.0159	0	
8	0.102	0.0159	0	0.0159	0	
9	0.1171	0.0159	0	0.0159	0	
10	0.1323	0.0159	0	0.0159	0	
11	0.1475	0.0159	0	0.0159	0	
12	0.1626	0.0159	0	0.0159	0	
13	0.1778	0.0159	0	0.0159	0	
14	0.193	0.0159	0	0.0159	0	
15	0.2081	0.0159	0	0.0159	0	
16	0.2233	0.0159	0	0.0159	0	
17	0.2385	0.0159	0	0.0159	0	
18	0.2536	0.0159	0	0.0159	0	
19	0.2688	0.0159	0	0.0159	0	
20	0.284	0.0159	0	0.0159	0	
21	0.2991	0.0159	0	0.0159	0	
22	0.3143	0.0159	0	0.0159	0	
23	0.3245	0.0159	0	0.0159	0	
24	0.355	0.0159	0	0.0159	0	
25	0.36	0.0159	0	0.0159	0	
26	0.3664	0.0159	0	0.0159	0	
27	0.3867	0.0159	0	0.0159	0	
28	0.3974	0.0159	0	0.0159	0	
29	0.4105	0.0159	0	0.0159	0	
30	0.4236	0.0159	0	0.0159	0	
31	0.4368	0.0159	0	0.0159	0	

32	0.4499	0.0159	0	0.0159	0	
33	0.463	0.0159	0	0.0159	0	
34	0.4762	0.0159	0	0.0159	0	
35	0.4893	0.0159	0	0.0159	0	
36	0.5024	0.0159	0	0.0159	0	
37	0.5156	0.0159	0	0.0159	0	
38	0.5287	0.0159	0	0.0159	0	
39	0.5418	0.0159	0	0.0159	0	
40	0.5512	0.0159	0	0.0159	0	
41	0.5766	0.0159	0	0.0159	0	
42	0.5893	0.0159	0	0.0159	0	
43	0.602	0.0159	0	0.0159	0	
44	0.6118	0.0159	0	0.0159	0	
45	0.6216	0.0159	0	0.0159	0	
46	0.6313	0.0159	0	0.0159	0	
47	0.6411	0.0159	0	0.0159	0	
48	0.6509	0.0159	0	0.0159	0	
49	0.6604	0.0095	0	0.0095	0	
3	0.0266	0.0381	0.0159	0.0429	0.0159	VW24 Conical AMB Rotor
4	0.0393	0.0429	0.0159	0.0476	0.0159	
5	0.052	0.0476	0.0159	0.0476	0.0159	
6	0.0774	0.0476	0.0159	0.0476	0.0159	
23	0.3245	0.127	0.0159	0.127	0.0159	Disk
24	0.355	0.0316	0.0159	0.0316	0.0159	
25	0.36	0.0298	0.0159	0.0298	0.0159	
26	0.3664	0.0348	0.0159	0.0348	0.0159	
39	0.5418	0.0476	0.0159	0.0476	0.0159	VW13 Conical AMB Rotor
40	0.5512	0.0476	0.0159	0.0476	0.0159	
41	0.5766	0.0476	0.0159	0.0429	0.0159	
42	0.5893	0.0429	0.0159	0.0381	0.0159	

APPENDIX B

Test matrix

Table B-I Test matrix

Trial Number	Type of Shaft	AMB Injection Frequency	Injection Type
1	Healthy	0 Hz	none
2	Healthy	18.6 Hz	sine wave
3	Healthy	22.3 Hz	sine wave
4	Healthy	50.1 Hz	sine wave
5	25% EDM Cut	0 Hz	none
6	25% EDM Cut	18.6 Hz	sine wave
7	25% EDM Cut	22.3 Hz	sine wave
8	25% EDM Cut	50.1 Hz	sine wave
9	40% EDM Cut	0 Hz	none
10	40% EDM Cut	18.6 Hz	sine wave
11	40% EDM Cut	22.3 Hz	sine wave
12	40% EDM Cut	50.1 Hz	sine wave

APPENDIX C

Experimental Verification of the Current -Force Relationship

The amplitude of the external harmonic excitation force that was used in the present work was experimentally determined to be 5 N. This was accomplished by applying a force with a known amplitude to the levitated non-rotating rotor on the V-axis and measuring the corresponding current in the magnetic actuator. Figure C-1 shows the configuration of the experiment for verification of the current-force relationship.

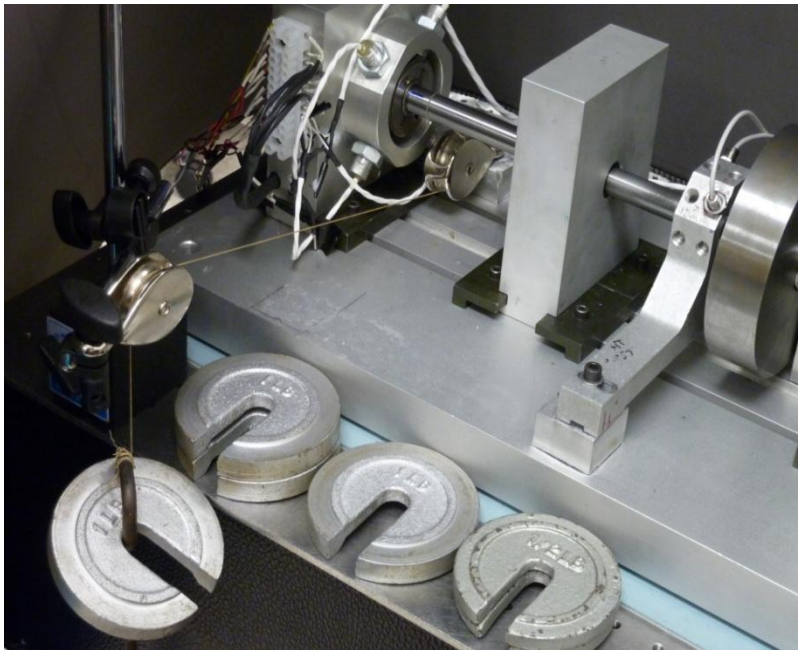

Figure C-1 Configuration of the current-force relationship experiment

Particularly, the experiment was accomplished in the following way. First, the current in the magnetic actuator was measured while the levitated rotor was at rest. Next, the levitated rotor was loaded incrementally with weights and corresponding currents in the

actuator were measured. The experimental data is shown in Table C-I. Finally, the current-force relationship was plotted. Figure C-2 show the plot of the current-force relationship.

Table C-I The experimental data

Force (lbf)	Force (N)	Current (Amp)	Net Current (Amp)
0	0.000	1.84	0
0.68	3.025	1.91	0.07
1.18	5.249	1.97	0.13
1.68	7.473	2.02	0.18
2.18	9.697	2.07	0.23
2.68	11.921	2.12	0.28
3.18	14.145	2.17	0.33
3.68	16.369	2.23	0.39
4.18	18.594	2.27	0.43
4.68	20.818	2.33	0.49
5.18	23.042	2.39	0.55
5.68	25.266	2.43	0.59

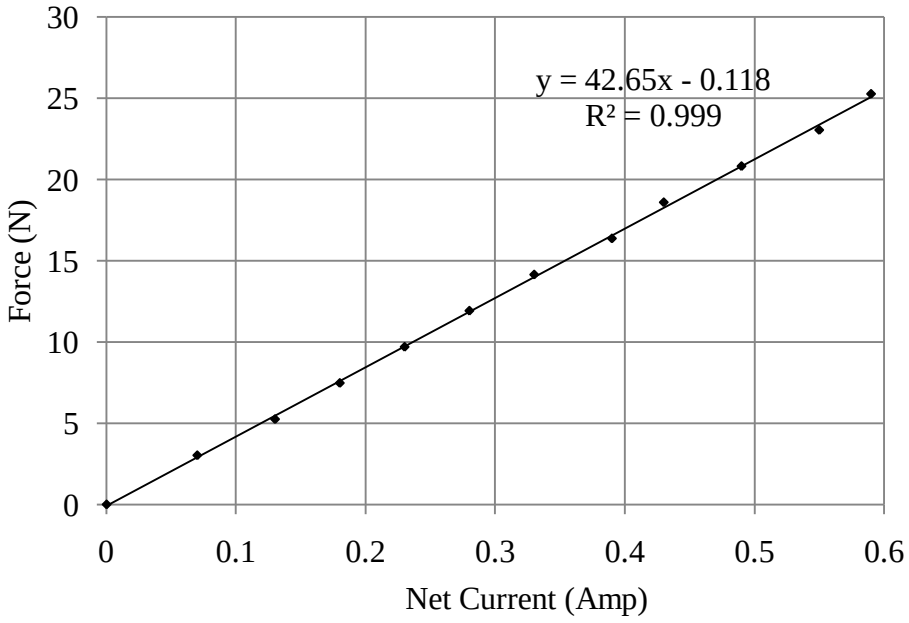

Figure C-2 Current-force relationship

APPENDIX D

Determination of Stiffness and Damping Coefficients of the AMB

In order to have a suitable model of a cracked rotor supported using AMBs, the effective stiffness and damping coefficient of AMB have to be determined. Consider a well-known second order mass-spring-damper system shown on Figure D-1.

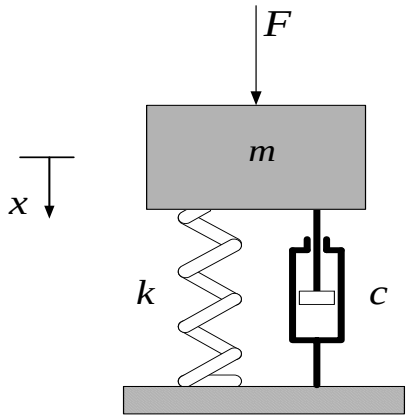

Figure D-1 Mass-spring-damper system

The equation of motion for this system is:

$$m\ddot{x} + c\dot{x} + kx = F \tag{D.1}$$

Taking the Laplace transform of this equation results in:

$$\frac{X(s)}{F(s)} = \frac{1}{ms^2 + cs + k} \tag{D.2}$$

In order to translate equation (D.2) from Laplace domain to frequency domain, set $s = j\omega$ and substitute it into equation (D.2) to yield:

$$\frac{X(j\omega)}{F(j\omega)} = \frac{1}{(k - m\omega^2) + cj\omega} \tag{D.3}$$

Next, consider a typical one degree of freedom magnetic bearing system that consists of two opposing electromagnets and its schematic is shown in Figure D-2.

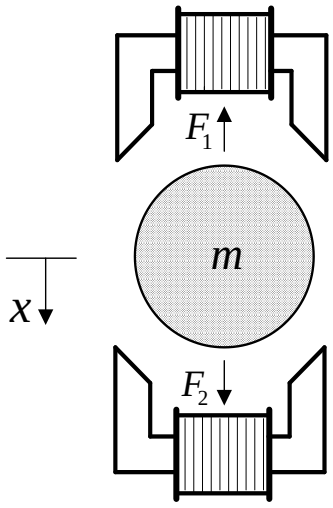

Figure D-2 Schematic diagram of a single degree of freedom AMB

Using Newton's second law, equation of motion for a given system can be written as follows:

$$m\ddot{x} = F_1 - F_2 + F_d \tag{D.4}$$

where m is the mass of the suspended rotor, F_1 and F_2 are the forces generated by electromagnets, and F_d is a disturbance force acting on a rotor. According to the theory of electromagnetic suspension, the magnetic force applied to a rotor by one pair of electromagnets using AMBs can be expressed as [Schweitzer, 1993]:

$$F_{AMB} = F_1 - F_2 = \frac{1}{4}\mu_o A_a N^2 C\left[\frac{\left(I_b + I_c\right)^2}{\left(s_o - x\right)^2} - \frac{\left(I_b - I_c\right)^2}{\left(s_o + x\right)^2}\right] \tag{D.5}$$

where: μ_o - magnetic field constant, A_a - cross-section area of the air gap, N - number of turn per coil, C - geometric factor, I_b - bias current, I_c - control current, s_o - nominal air gap, x - displacement of the rotor.

The above equation can be linearized about operating point using Taylor series expansion as [Schweitzer, 1993]:

$$F_{AMB} = \mu_o A_a N^2 C \frac{I_b}{s_o^2} i_x + \mu_o A_a N^2 C \frac{I_b^2}{s_o^3} x = k_i i_x + k_{xf} x \tag{D.6}$$

where k_i is a force-current factor and k_{xf} is a force-displacement factor. Substituting equation (D.6) into equation (D.4) results in the following:

$$m\ddot{x} = k_i i_x + k_{xf} x + F_d \tag{D.7}$$

Based on the control theory, block diagram of the closed loop control of the rotor system with AMB's in Laplace domain can be expressed as follows:

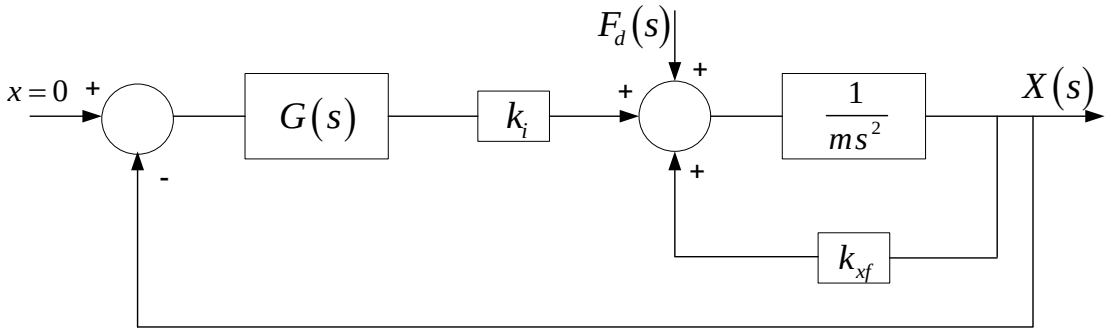

Figure D-3 Block diagram of the closed loop control of the AMB system

In Figure D-3, $G(s)$ is the controller transfer function which consists of PID controller, low pass filter and two notch filters. Using block diagram reduction method, which is based on the elimination of feedback loops, the block diagram shown in Figure D-3 transformed into a simpler form. Figure D-4 shows the transformation procedure.

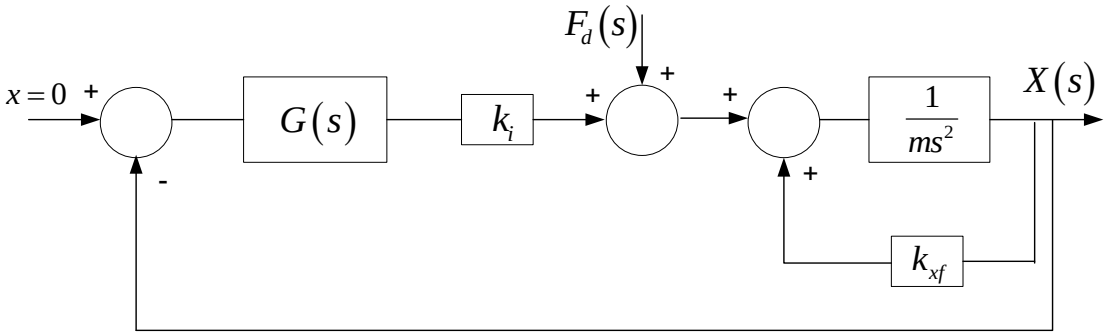

(a)

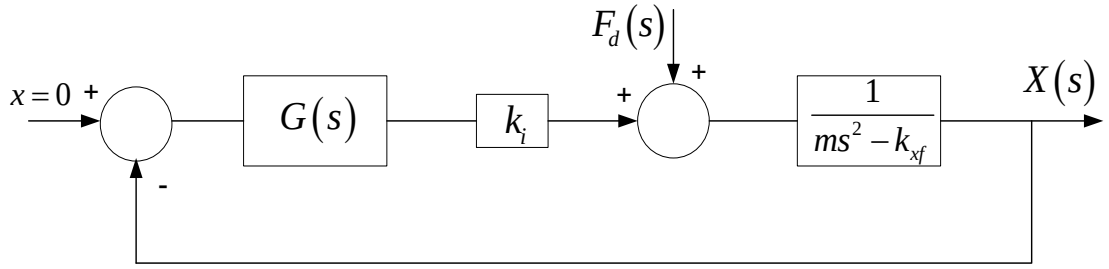

(b)

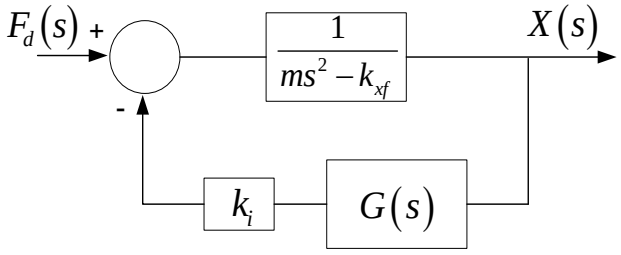

(c)

Figure D-4 Block diagram reduction procedure

From Figure D-4(c), the total transfer function of the system which is a ratio of the output signal *X(s)* (position of the rotor) to the input signal $F_d(s)$ (the disturbance force) can be written as follows:

$$\frac{X(s)}{F_d(s)} = \frac{1}{ms^2 - k_{xf} + k_i G(s)} \tag{D.8}$$

In order to translate equation (D.8) from Laplace domain to frequency domain, set $s = j\omega$ and substitute it into equation (D.8) to yield:

$$\frac{X(j\omega)}{F_d(j\omega)} = \frac{1}{-m\omega^2 - k_{xf} + k_i G(j\omega)} \tag{D.9}$$

where $j = \sqrt{-1}$ is an imaginary number. Since $G(j\omega)$ is a complex number which has a real and imaginary part, equation (D.9) can be rewritten in the following way:

$$\frac{X(j\omega)}{F_d(j\omega)} = \frac{1}{\left(-m\omega^2 - k_{xf} + k_i \operatorname{Re}\left[G(j\omega)\right]\right) + k_i \operatorname{Im}\left[G(j\omega)\right]} \tag{D.10}$$

Comparing equations (D.3) and (D.10), the stiffness and damping coefficients of the AMB system can be expressed as:

$$\begin{cases} k = k_i \operatorname{Re}\left[G(j\omega)\right] - k_{xf} \\ c = \dfrac{k_i \operatorname{Im}\left[G(j\omega)\right]}{\omega} \end{cases} \tag{D.11}$$

The MATLAB software was used to develop a computer code for calculation of the stiffness and damping coefficients of the AMB. The parameters used in the code were previously presented in Chapter IV table 1. Calculated stiffness and damping are shown in Figure D-5 below.

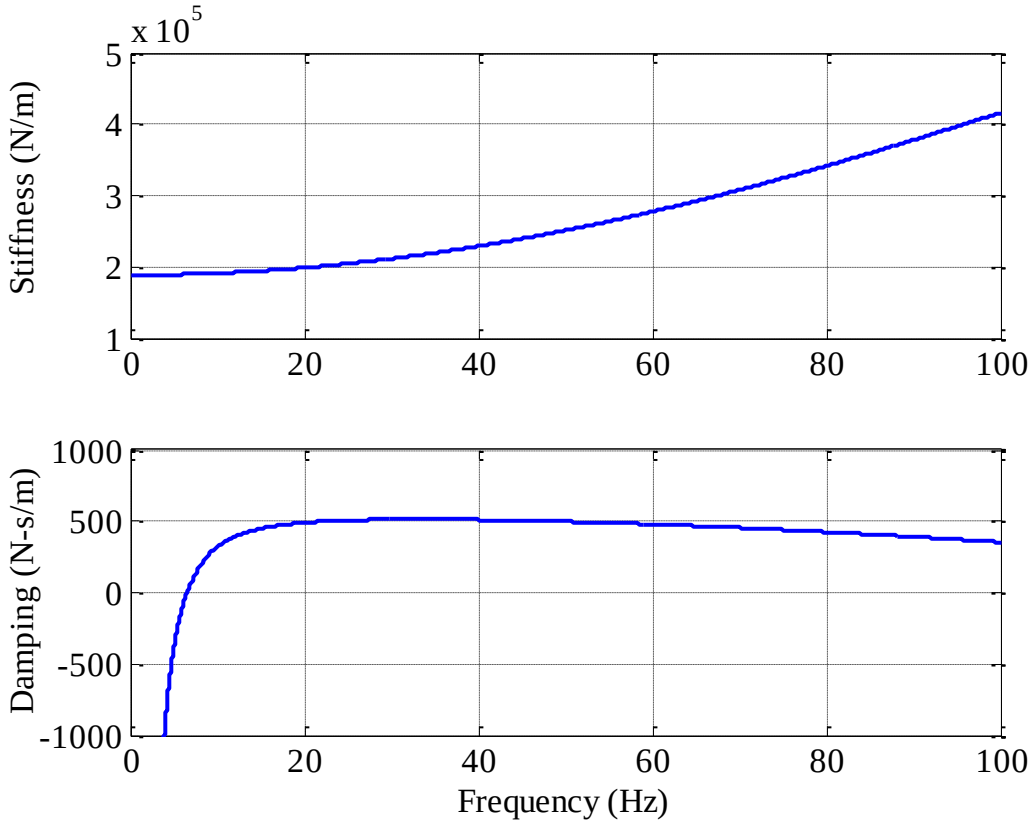

Figure D-5 Calculated stiffness and damping of the AMB

APPENDIX E

Impact Hammer Test

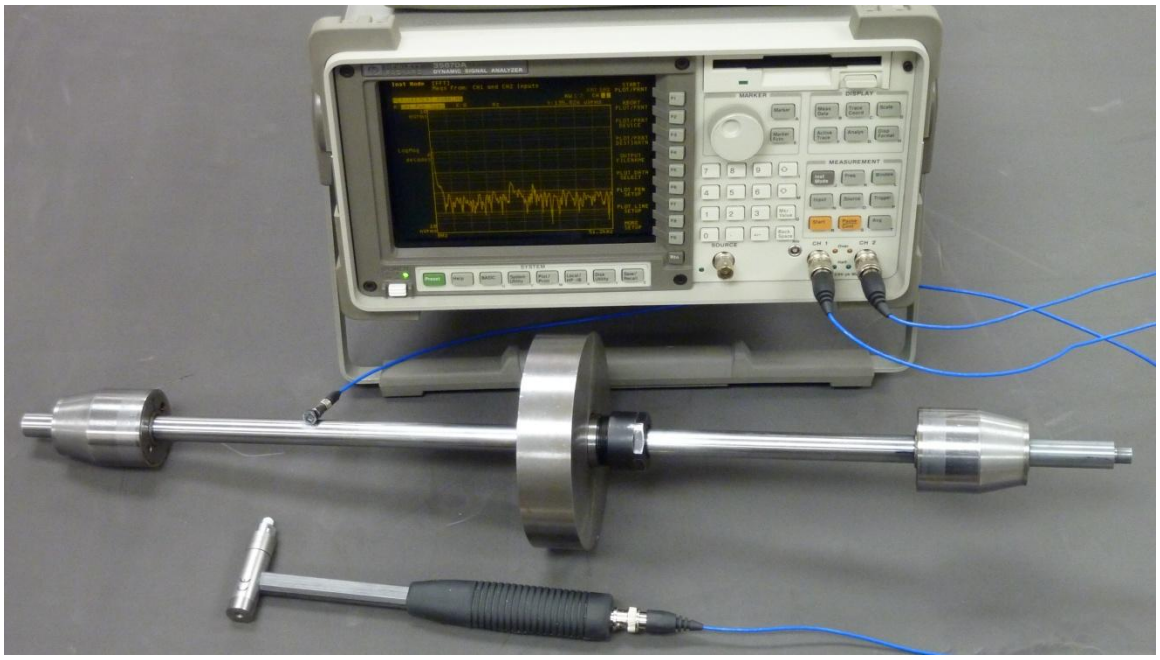

Figure E-1 Assembly of the impact hammer test